RICE UNIVERSITY

Magnetic Modeling of the Solar Corona

by

Anne W. Sandman

A THESIS SUBMITTED IN PARTIAL FULFILLMENT
OF THE REQUIREMENTS FOR THE DEGREE

Doctor of Philosophy

APPROVED, THESIS COMMITTEE:

David Alexander, Chair
Professor of Physics and Astronomy

Thomas W. Hill
Professor of Physics and Astronomy

Michael Gustin
Professor of Professor of Biochemistry
and Cell Biology

Markus J. Aschwanden
Adjunct Professor of Physics and
Astronomy

HOUSTON, TEXAS

DECEMBER 2010

Abstract

Magnetic Modeling of the Solar Corona

by

Anne W. Sandman

The magnetic field is the dominant force in the Sun's outer atmosphere, the corona. It determines the large-scale structure of the corona, governs the small-scale activity that heats the plasma, and powers energetic transient phenomena. The study of the coronal magnetic field is an important component of efforts to understand the corona as a whole, but the high plasma temperature and relative weakness of the field in the corona preclude direct measurement of the field in this region. Theoretical modeling, therefore, provides critical support to our investigation of the coronal magnetic field.

This thesis contains an exploration of magnetic modeling in the context of the physics of the solar atmosphere. Using the novel stereoscopic capability of the *Solar Terrestrial Relations Observatory*, we compare the 3D coronal field structure with various models to study the distribution of the magnetic field and large-scale currents in several active regions. In addition to using existing models, we developed an original modeling approach: using several magnetic dipoles under the solar surface, configured based on comparison with the observed field structure, we overcome certain weaknesses inherent in existing models. The misalignment angles between the vectors of the reconstructed and model fields measure the departure of the model field from the observed field structure, indicating the non-potentiality of the coronal field.

The dipole modeling method achieves a significant reduction in misalignment compared with previously established models, implying a closer agreement between our model field and observed field structures. We use the misalignment measurements to examine the free energy contained in active region magnetic fields and find that following major flares, the field relaxes substantially from a high-shear configuration to a low-shear configuration, indicating a significant loss of free energy in the field. The results in this thesis yield insight into the physics of the solar atmosphere and provide a means to better understand the complex region between the photosphere and corona. Improved understanding of this region will elucidate how the field connects the two regions, and the way in which energy is transported from the convective solar interior into the corona and heliosphere.

Acknowledgements

I would first like to express my thanks to my advisor at Rice University, Dr. David Alexander, and my advisor at Lockheed Martin Solar and Astrophysics Laboratory, Dr. Markus Aschwanden, for their mentorship, patience, and many helpful discussions. To my family and friends, I am also humbly thankful: for a community in which it was not only acceptable, but encouraged for a girl to pursue studies in science; and for the camaraderie of those who unabashedly love learning. Last, but most certainly not least, I would like to express my profound gratitude to my boyfriend for his invaluable and seemingly inexhaustible support and encouragement. It is possible to complete a Ph.D. unaccompanied, but immeasurably less lonely with a partner. Thank you, Steve, for being my keel and my western wind.

This work was supported by the NASA *Solar Terrestrial Relations Observatory* under Naval Research Laboratory contracts N00173-07-1-G021 (Rice University) and N00173-02-C-2035 (Lockheed Martin Solar and Astrophysics Laboratory).

Contents

List of Figures

List of Tables

Chapter 1

Introduction

Magnetic fields can be found throughout astrophysics, and our star is no exception: from deep in its interior to the edges of its extended outer atmosphere, magnetic fields permeate the Sun and the surrounding interplanetary environment. The prevalence of magnetic fields makes them a key component of our understanding of the Sun and its effect on the Earth. Magnetic fields not only influence the structure of the solar atmosphere, but also play a vital role in the dynamic processes that send energetic particles and magnetic fields outward among the planets.

These processes begin, perhaps improbably, far below the Sun's surface. Solar magnetic fields are believed to originate in the tachocline (Spiegel & Zahn, 1992), the interface between the Sun's radiative core and its outer convective layers at a distance of approximately 0.7 solar radii, or 490,000 km, from the solar interior. Whereas the radiative core rotates essentially as a solid body, the convective zone rotates differentially depending on the latitude and distance from the center of the Sun.

The variation in rotation rates throughout most of the convective zone is small, but increases sharply at the interface between the radiative and convective zones (Miesch, 2005). The shearing of the plasma that results at this abrupt boundary drives the solar dynamo, generating the magnetic field. The field is thought to be created in large, concentrated flux tubes that possess increased internal pressure relative to their environment due to their high field strength. This overpressure leads the tubes to rise buoyantly through the convective layer until they reach the surface (see, for example, Fan et al., 2003; Fan, 2004; Miesch, 2005).

At the Sun's visible surface, known as the photosphere, the flux tubes break through and create small regions of strong bipolar magnetic field known as sunspots, which we can observe at optical wavelengths (see Figure 1.1). While the field strength over most of the photosphere is on the order of tens or hundreds of Gauss, the field strength in these concentrated regions can reach up to a few thousand Gauss. The photospheric plasma in these regions is cooler and denser than the surrounding photosphere as a result of the strong field, which is believed to inhibit locally the convective motions that transport energy to the photosphere. Sunspots therefore appears darker compared with the rest of the solar surface, although at temperatures of about 4200 K, they are nevertheless extremely bright in their own right.

Above the photosphere, although the field weakens with increasing radius (under 10 Gauss for heights above 10^5 km), its role in the overall structure and dynamics of the atmosphere grows. The chromosphere, the layer of the atmosphere immediately

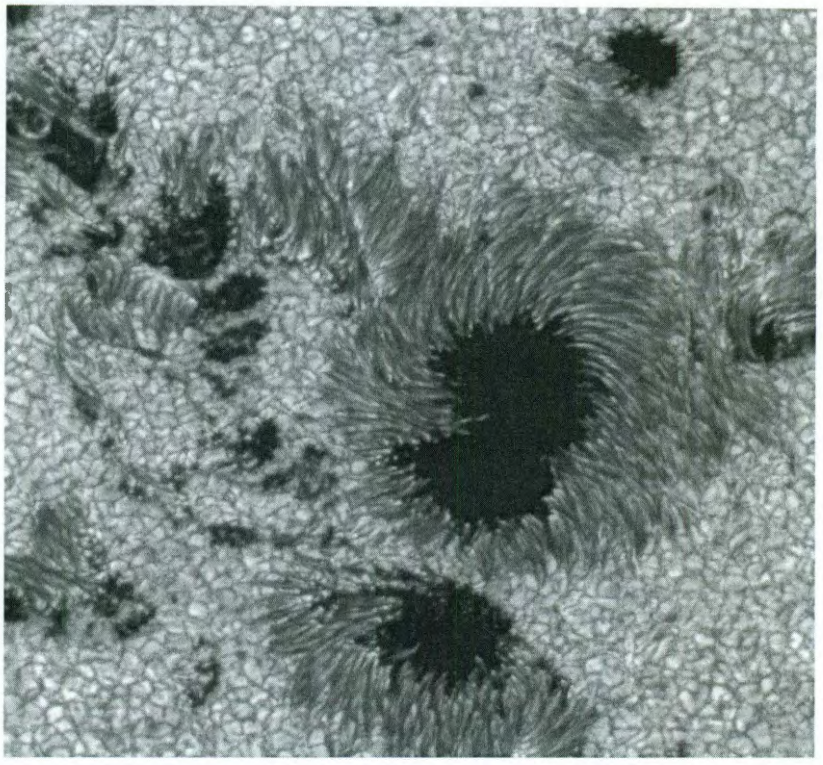

Figure 1.1: A group of sunspots observed by the Swedish Solar Telescope. The granular structures surrounding the sunspots are the result of convective motions that transport energy from the Sun's radiative core to the photosphere. It is believed that this convective activity is suppressed by the strong magnetic field in sunspots, which leads the sunspots to appear darker than their surroundings. (The Royal Swedish Academy of Sciences/The Institute for Solar Physics)

above the photosphere, experiences a dramatic decrease in plasma density: from $\sim 10^{17}$ cm^{-3} in the photosphere to $10^{10} - 10^{11}$ cm^{-3} in the chromosphere (see Table 1.1). In the corona, which comprises the bulk of the atmospheric volume and lies above the chromosphere, the density drops still further, reaching $10^{7} - 10^{9}$ cm^{-3}. Since the corona can be considered as an ideal gas (Aschwanden, 2004), the pressure is directly

proportional to both the density and the temperature. Although the temperature increases substantially in the corona, the drop in density is sufficiently severe that the pressure decreases by several orders of magnitude (Table 1.1).

The significance of this reduction in thermal pressure becomes clear when we consider the plasma beta parameter, which determines the relative influence of the plasma and magnetic field. The plasma beta is defined as the ratio of the thermal pressure to the magnetic pressure:

$$\beta = \frac{p_{thermal}}{p_{magn}} = \frac{16\pi n_e kT}{B^2}, \tag{1.1}$$

where n_e is the electron density of the plasma, T the plasma temperature, and B the magnitude of the magnetic field. In the corona, the plasma beta is small ($\beta < 1$, see Table 1.1) so the magnetic pressure exceeds the thermal pressure, and the magnetic field dominates the plasma. An additional consequence of the relatively strong magnetic field is that diffusion across the field is effectively prohibited, and the plasma is forced to flow parallel to the field.

The magnetic field and the plasma are further bound together by the fact that the corona can be considered a nearly ideal conductor. Because it is a fully ionized plasma at a high temperature and relatively low density, the corona approaches the perfectly conducting limit (see Appendix A). In general, the induction equation, which relates

the magnetic field to the plasma velocity, is written as follows:

$$\frac{\partial \mathbf{B}}{\partial t} = \nabla \times (\mathbf{v} \times \mathbf{B}) - \nabla \times (\eta \nabla \times \mathbf{B}) \tag{1.2}$$

where η is the magnetic diffusivity, which is inversely proportional to the electrical conductivity, σ: $\eta = 1/(\mu\sigma)$. For a highly conductive plasma, we have $\eta \ll 1$, and the induction equation reduces to the following form:

$$\frac{\partial \mathbf{B}}{\partial t} = \nabla \times (\mathbf{v} \times \mathbf{B}) \tag{1.3}$$

A direct consequence of this equation is the *frozen flux theorem*, which describes the relationship between the magnetic field and the plasma in the perfectly conducting limit. For a surface moving with the ambient plasma, the frozen flux theorem defines the conservation of magnetic flux through that plasma. Because of this flux conservation, the field is considered "frozen" to the plasma: changes in the field topology determine the movement of the plasma, or vice versa. (The frozen flux theorem is discussed in more detail in Appendix A.) Thus, in regimes of the solar atmosphere where the plasma beta is small, the plasma is confined to loop-like structures that are assumed to outline the morphology of the field. Conversely, where the plasma beta is greater than unity (e.g. the photosphere or high corona), the field is subject to the forces imparted by the plasma motions.

We can readily observe this dynamic in the solar corona, where high-beta and

Table 1.1. Physical Characteristics of Regimes of the Solar Atmosphere (modified from Aschwanden, 2004).

Parameter	Photosphere	Low Corona	High Corona
Electron density n_e (cm^{-3})	2×10^{17}	1×10^9	1×10^7
Temperature T (K)	5×10^3	$1 - 3 \times 10^6$	1×10^6
Pressure p (dyne cm^{-2})	1.4×10^5	$0.3 - 0.9$	0.02
Magnetic field B (G)	500	10	0.1
Plasma β parameter	14	$\sim 0.1 - 0.2$	7

low-beta regimes exist adjacent to one another. Perhaps most commonly recognized as the ghostly, wispy structures seen in white light images of solar eclipses (broadband observations across optical wavelengths, see Figure 1.2), the corona is the extensive regime of tenuous plasma that begins approximately 2500 km above the solar surface and extends for several solar radii. In the high corona, where the plasma beta is on the order of unity, the plasma dominates the magnetic field. "Open" field lines, which close elsewhere in the heliosphere, are drawn outward by the solar wind until they become effectively radial at large distances. (This property is a fundamental component of the Potential Field Source Surface (PFSS) magnetic field extrapolation method, which is used in my research and discussed in Section 2.2.2.) Other radially stretched structures include streamers, which can reach from close to the solar surface to heights of a few solar radii and are thought to be associated with the current sheets that form at the boundary between regions of oppositely directed magnetic field. We also observe long coronal loops, which trace the large-scale magnetic field and rise to

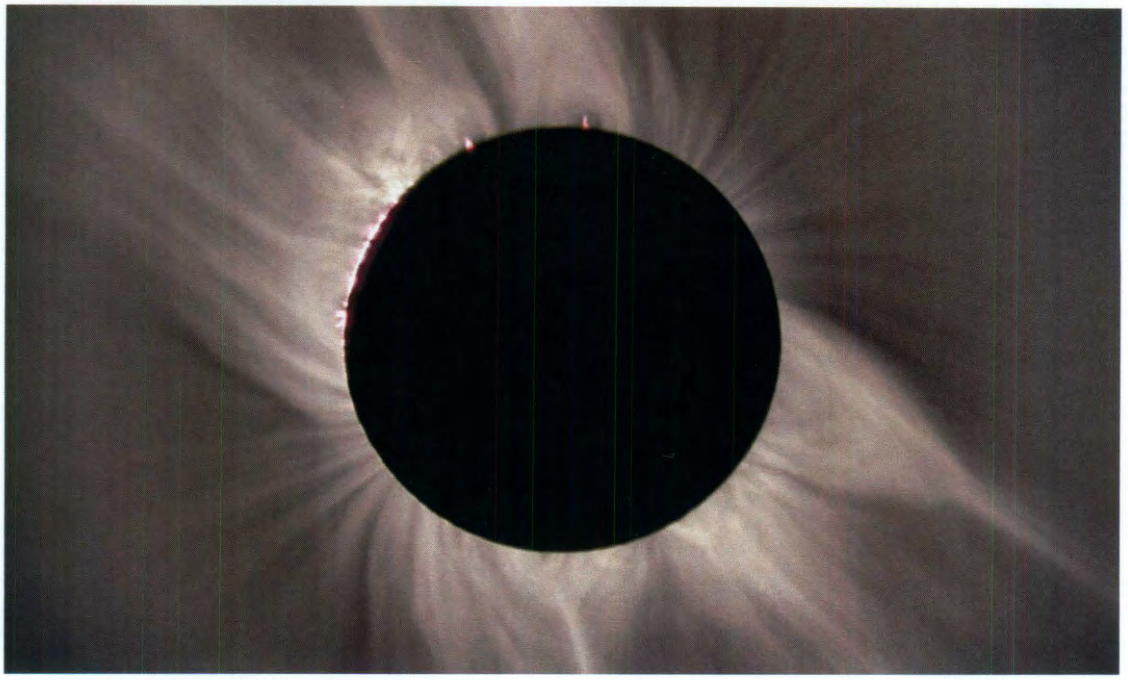

Figure 1.2: Solar eclipse of March 29, 2006, as viewed from Sidi Barany, Egypt. (Jean Mouette, Serge Koutchmy, CNRS)

an altitude of one solar radius before returning to close at the opposite polarity on the solar surface.

Shorter loops, sometimes displaying multipolar field structure with complex loop connectivity among different regions (see Figure 1.3) populate the low corona. These loops extend up to a few tenths of a solar radius above the photosphere, where the plasma beta is small ($\beta < 1$). As in the high corona, the field and plasma are tied to each other. Here, however, rather than the plasma motions stretching out the field as in the high corona, the field in the low corona determines the behavior of the plasma. We observe that the plasma is confined to loop-like structures which are typically assumed to represent the topology of the field.

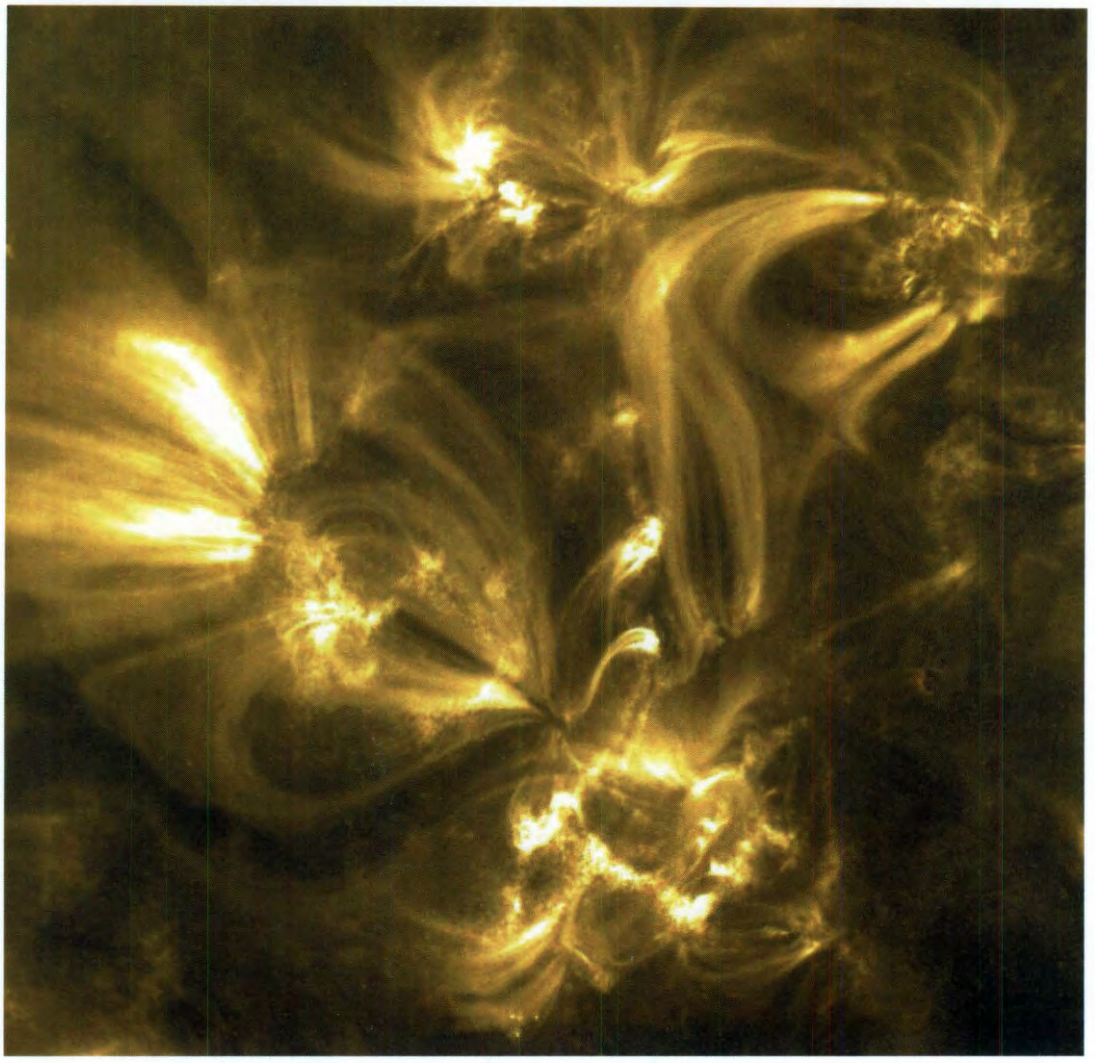

Figure 1.3: Complex coronal loops observed by the *Transition Region and Coronal Explorer* (TRACE) in the 171 Å channel, showing plasma at approximately 1 million Kelvin. (TRACE team)

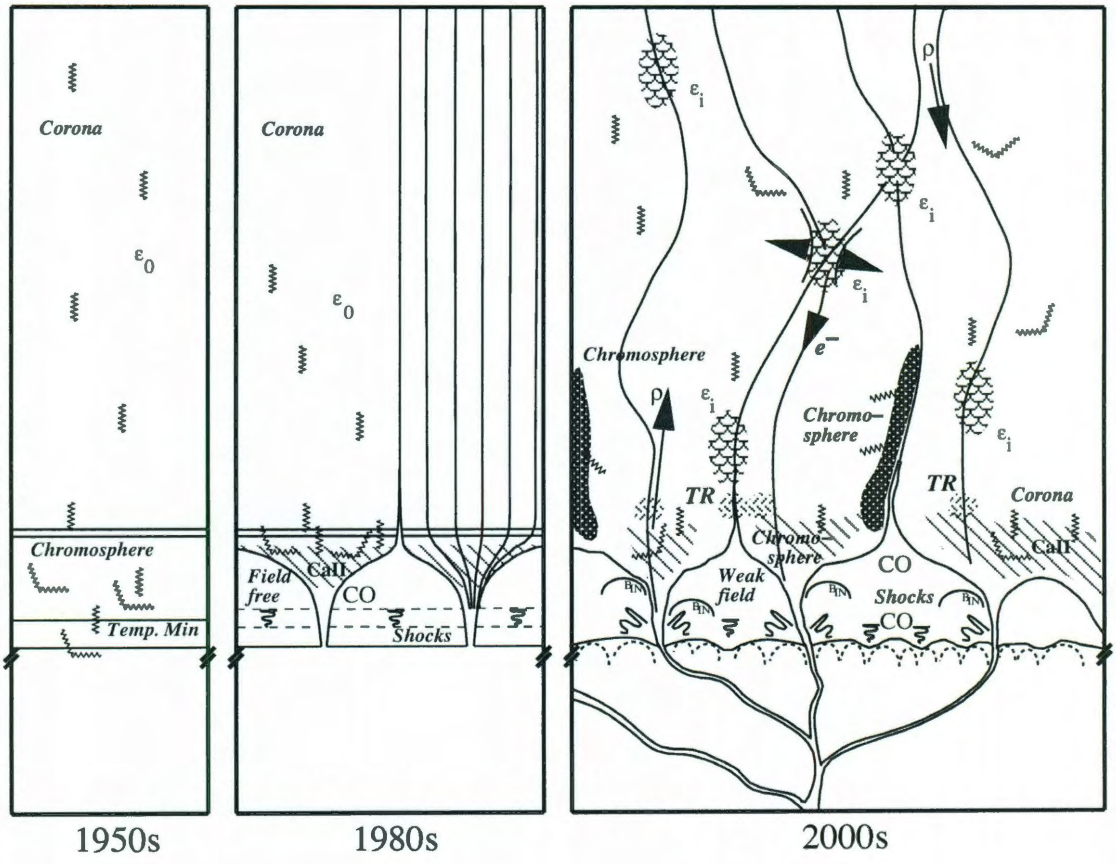

Figure 1.4: Cartoon representation of our conceptions of the solar corona before and during the space age. In the 1950s, prior to space-based observations of the Sun: the solar atmosphere as a series of simple, gravitationally stratified layers. In the 1980s, after early space-based solar observatories: the corona incorporates some magnetic structures such as simple fluxtubes. In the 2000s, a collection of inhomogeneous regions and miniature atmospheres subject to intermittent heating and cooling, plasma flows, magnetic reconnection, and other dynamic processes (Schrijver, 2001).

Because the average temperature of the corona is extraordinarily high, on the order of one million Kelvin or higher, the plasma that fills these loops radiates in the extreme ultraviolet (EUV) and soft X-ray wavelengths ($\lambda < 300$ Å and $\lambda < 60$ Å, respectively). Light at these wavelengths is absorbed by the Earth's atmosphere, so observations in the EUV and X-ray must be taken from space. Thus, for most of the

history of solar observations, our view of the corona has been limited to white light observations of large-scale coronal structure. Such observations were primarily taken during solar eclipses until the invention of the *coronagraph*, in which the bright solar disk is artificially occulted in order to simulate the effect of an eclipse, enabled routine observation of the corona in white light (Lyot, 1932). It was not until the latter half of the 20th century, with the emergence of space-based observatories, that we were able to view the Sun in the EUV and X-ray and appreciate the complex structure of the low corona.

Prior to these advancements, we had only the simplest conception of the corona, as an atmosphere stratified according solely to the effects of gravity (Schrijver, 2001). Following the advent of space telescopes, however, our understanding of the corona has evolved as progressively more detailed observations have revealed the corona's complexity. A brief summary of this evolution is shown in Figure 1.4. Early efforts at space-based coronal observations used rocket-mounted cameras (Baum et al., 1946; Strain, 1947). *Skylab*'s Apollo Telescope Mount (1973-1974) provided images of the diffuse soft X-ray corona (Figure 1.5), EUV and X-ray spectra, and coronagrams that gave indications of the complex loop structure of the low corona, as well as insight into the dynamics of transient phenomena. Skylab also revealed the existence of coronal holes (Vaiana et al., 1976), regions of the atmosphere that are cooler and more rarified than the surrounding corona and therefore appear darker at EUV and X-ray wavelengths. Coronal holes typically contain the open magnetic field that can

be seen in white light observations of the large-scale corona, and can be a major source of recurring geomagnetic storms, connecting with the Earth every solar rotation.

The *Yohkoh* mission, active from 1991 to 2001, yielded further improvements in our ability to observe the X-ray corona and the configuration of the low coronal magnetic field. In particular, Yohkoh provided a more detailed view of the dynamic nature of transient phenomena and the magnetic field's role in this activity (Fletcher et al., 2001; Sterling & Moore, 2004). The launch of the *Transition Region and Coronal Explorer* (TRACE, 1998 - 2010), however, took coronal observations to an entirely new level. With its unprecedented 1 arcsec (1″) spatial resolution (0.5″ pixels) and temporal cadence as low as 1 second (Handy et al., 1999), TRACE sparked a revolution in our understanding of coronal physics, revealing a new degree of complexity and activity in the magnetic field.

This complexity is reflected in the inhomogeneity of the magnetic field at the solar surface. Although photospheric plasma flows exist in a high-beta regime in which the field dominates the plasma, they can nevertheless influence the structure of the field high above the photosphere because the field is frozen to the plasma (see Appendix A). Indeed, we observe that photospheric motions can drive the motion of sunspots that can, in turn, lead to more energetic coronal activity (see, for example, Fan, 2009; Kazachenko et al., 2009; Yan et al., 2009). These motions, along with the emergence of additional flux from the convection zone below the photosphere, introduce twist or shear into the coronal field, which results in an increase in the amount of free energy

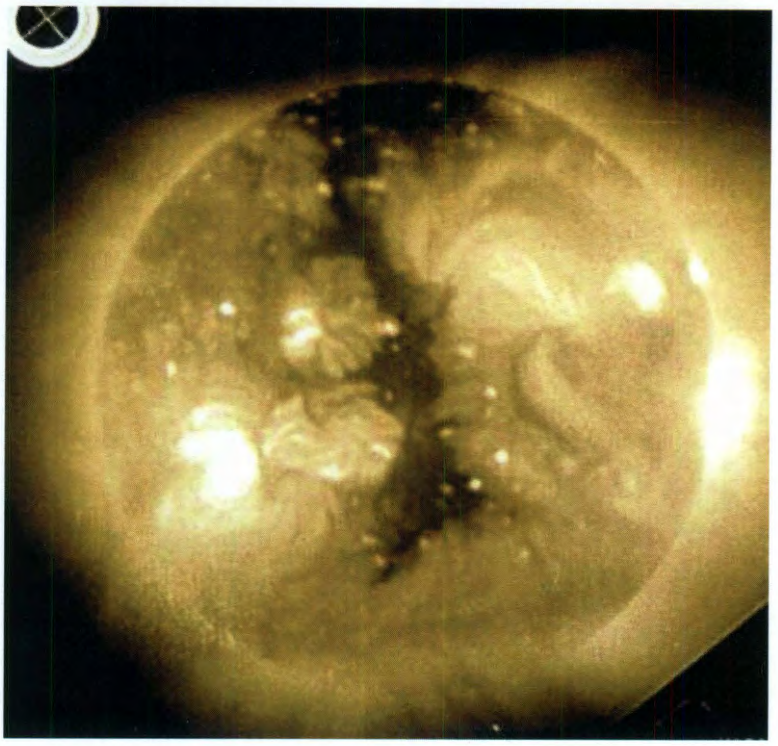

Figure 1.5: The solar corona in soft X-ray, 2-60 Å, as observed by the Skylab Soft X-Ray Telescope (NASA).

available. This free energy takes the form of electrical currents, which must be aligned with the field due to the low-plasma-beta requirement that the plasma flow parallel to the field: the curl of the field is directly proportional to the field itself. Because the plasma cannot readily flow across the field, the increased energy from the twist and shear cannot easily dissipate, and the energy is therefore stored in the field.

The energy does not, however, accumulate indefinitely: given a sufficient degree of stress, the field may experience a loss of equilibrium (Lin et al., 2003). In this case, a portion of the stored energy is released through either magnetic reconnection or flux cancellation, heating the corona and sometimes driving transient phenomena

such as flares and coronal mass ejections (CMEs). Although the exact mechanisms that trigger flares and CMEs are not yet well understood, it is generally accepted that the magnetic field is intimately involved (see, for example, Lin et al., 2010; Mittal & Narain, 2010). The resulting events accelerate particles to relativistic energies and, in the case of CMEs, launch $10^{11} - 10^{13}$ kg of matter into the heliosphere at hundreds of kilometers per second. The energetic particles and magnetic fields contained in these eruptions can interact with planetary magnetospheres, creating "space weather" and potentially impacting radio communications, man-made satellites, and power grids at the Earth's surface (Pulkkinen, 2007). This connection between the Earth's environment and magnetically driven solar activity highlights the importance of understanding magnetic fields in the solar corona.

Unfortunately, our efforts to understand the coronal magnetic field have long been hindered by difficulties in observing the field on large scales. Although we can straightforwardly measure the line-of-sight component of the field at the solar surface, and even make limited measurements of the coronal field (Casini & Judge, 1999; Brosius & White, 2006; Tomczyk et al., 2008), the ability to make reliable and comprehensive observations of the coronal field remains elusive at the present time. These difficulties will be discussed in more detail in Chapter 2.

The inadequacy of coronal field measurement techniques has led solar physicists to supplement observations with analytical and, more recently, numerical models of the field. These models, however, are not without their disadvantages: they are

typically based on observations of the magnetic field at the photosphere, and require *a priori* assumptions about the nature of the field (for example, that it is current- or force-free; see Appendix B). An overview of magnetic field observations and modeling techniques is presented in Chapter 2. We begin with a summary of current magnetic field measurement techniques. We then discuss common magnetic modeling methods and the ramifications of assumptions typically made in the course of modeling coronal magnetic fields.

In the first research chapter, Chapter 3, we create PFSS extrapolations of the magnetic fields of three active regions, areas of the solar atmosphere that exhibit increased magnetic field and field-related activity (such as flares). We then obtain information about the three-dimensional (3D) coronal magnetic field topology through stereoscopic analysis of image pairs from the Extreme Ultraviolet Imager (EUVI) on board the twin *Solar Terrestrial Relations Observatory* (STEREO) spacecraft. Because the plasma beta in this region is generally low (Gary, 2001b), observed coronal loop structures can be treated as a proxy for the real magnetic field. We then use the 3D loop coordinates to evaluate the success of the PFSS extrapolations in reproducing the observed coronal field structure. STEREO observations contain no information regarding the magnetic field strength, so we base this comparison on the misalignment between the observed field structure, represented by the 3D structure of the coronal loops, and the model field structure. The model fields are also subjected to a simple radial stretching technique developed by Gary and Alexander (1999) as a means of

addressing some of the modeling difficulties discussed in Chapter 2.

Building on the results of the PFSS-EUVI study described in Chapter 3, in Chapter 4 we perform a similar analysis of an original magnetic modeling method developed as part of the research leading to this thesis. Our modeling technique uses a system of superimposed dipoles submerged below the solar surface, the parameters of which are optimized based on the misalignment angle criterion discussed in Chapter 3. Because the dipole placement is based solely on the coronal field structure as observed by STEREO/EUVI, the dipole model does not require boundary conditions based on measurements of the magnetic field at the photosphere. While photospheric field measurements are a useful tool for examining aspects of magnetic field models, the use of such boundary conditions has been identified as an outstanding problem in magnetic field extrapolation techniques (De Rosa et al 2009).

In Chapter 5, we use the dipole model as a foundation for estimates of the free energy contained in coronal loop configurations at several times following two major solar flares. Because STEREO images are unavailable for the two events used, we examine the relationship between the 2D misalignment angle, measured in images from TRACE and the *Solar Dynamics Observatory* (SDO), and the full 3D misalignment angle that can be obtained using stereoscopy. We then create dipole models of the two post-flare loop arcades, and use the energy contained in these current-free model fields as a basis for calculations of the free energy in force-free sheared arcade models of the active regions. Finally, in Chapter 6, we discuss the broader implications of

these results and their potential applications in future work.

Chapter 2

Solar Magnetic Fields: Measurements and Models

The darkening of the solar surface in sunspots and the ethereal structure of the solar atmosphere during solar eclipses have been noted by astronomers for millennia. It has been little more than a century, however, since we first began to understand the source of these phenomena: the Sun's magnetic field. George Ellery Hale discovered solar magnetic fields in 1908, when his spectroscopic observations of a sunspot revealed the telltale line splitting associated with the presence of a magnetic field (see Section 2.1.1). Although our instrumentation for measuring solar magnetic fields has become more sophisticated in the century following Hale's landmark observations, the fundamental physics that allows us to measure the fields remains largely the same. In this chapter we will discuss the techniques used to observe solar magnetic fields,

the limitations of those techniques, and the magnetic modeling efforts that we rely on to complement our observations.

2.1 Measuring Solar Magnetic Fields

2.1.1 Observational Techniques

Hale's conclusion regarding the existence of magnetic fields on the solar surface was based on his observation of the Zeeman effect, in which a spectral line is split by a magnetic field into three or more components. Using the splitting of spectral lines sensitive to the Zeeman effect, we can measure the magnetic field strength along the line of sight. Many current efforts to observe solar magnetic fields continue to rely on this phenomenon: the magnetograph at the Mount Wilson Solar Observatory, where Hale made his initial discovery, takes photospheric magnetograms using the Ca II K line at 3933.7 Å, Fe I at 5250.2 Å, Na I D2 at 5890 Å, Na I D1 at 5895.9 Å, and the Ni I line at 6767.8 Å (Babcock, 1953; Howard et al., 1968; Rhodes et al., 1988). The *Solar and Heliospheric Observatory* (SOHO) includes a magnetograph, the Michelson Doppler Imager (MDI), which provides uninterrupted coverage of the line-of-sight photospheric magnetic field using the Ni I line at 6767.8 Å (Scherrer et al., 1995). An example of an MDI magnetogram is shown in Figure 2.1.

These magnetograms provide only one component of the field: the magnitude parallel to the line of sight. To measure the full vector magnetic field, we can invert the

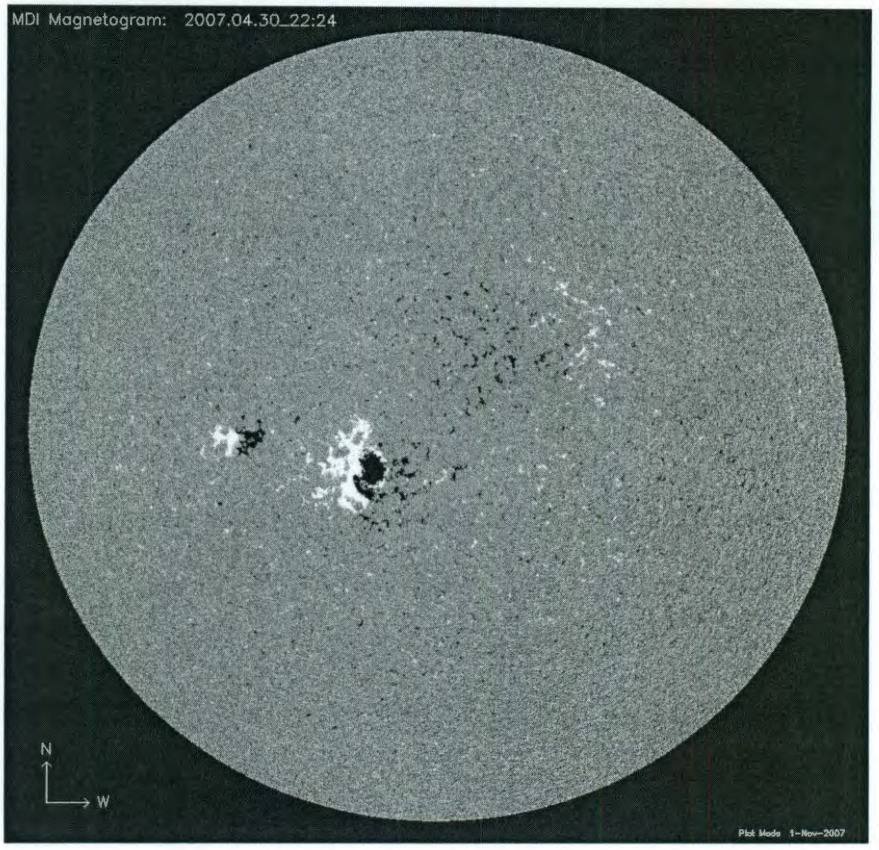

Figure 2.1: A line-of-sight magnetogram taken by SOHO/MDI April 30, 2007. Black represents negative polarity; white represents positive polarity (ESA/NASA).

Stokes profiles of photospheric emission lines that are sensitive to Zeeman splitting (see, for example, Westendorp Plaza et al., 1998; Bellot Rubio et al., 2000). Ground-based vector magnetographs in the United States include the Vector Spectromagnetograph (VSM) at the National Solar Observatory (NSO) and the Imaging Vector Magnetograph (IVM) at Mees Solar Observatory. There are also two space-based vector magnetographs currently in operation. The Solar Optical Telescope (SOT) on board the *Hinode* spacecraft, launched in 2008, was the first space-based solar vector

magnetograph, and provides high-resolution (pixel size 0.08″) vector magnetograms for a 328″ × 164″ field of view (corresponding to 240 × 120 Mm^2) with temporal cadence on the order of tens of seconds (Kosugi et al., 2007). The Helioseismic and Magnetic Imager (HMI) on board the *Solar Dynamics Observatory* (SDO), launched in early 2010, is the first space-based magnetograph to measure the vector magnetic field over the full disk of the Sun. SDO/HMI provides full disk vector magnetograms every 88 seconds at spatial resolution of 1″ per pixel (Kosovichev & HMI Science Team, 2007).

2.1.2 Measuring Coronal Fields: Challenges and Progress

Each of the instruments described in Section 2.1.1 measures the magnetic field at the photosphere, where the field is strong and the emission lines used are at relatively long wavelengths. These conditions, favorable to clear manifestations of the Zeeman effect, make measurement of the photospheric magnetic field a straightforward exercise. In the corona, however, the magnetic field is typically weak, up to a few tens of Gauss, compared with field strengths of hundreds or thousands of Gauss in the photosphere. The spectral lines observed in the corona are typically at shorter wavelengths due to the higher coronal temperatures, and have much broader thermal Doppler widths. The combination of these factors renders the Zeeman splitting of the lines extremely difficult to resolve. As a result, our ability to observe the coronal field using this effect has historically been severely limited.

It is possible, under certain conditions, to measure the coronal field using alternative techniques, but these measurements are typically feasible on only a small scale. The splitting of circular polarization modes of gyroresonance emission (Gary & Hurford, 1994; Brosius & White, 2006; White & Kundu, 1997) and thermal bremsstrahlung (Bogod & Gelfreikh, 1980; Ryabov et al., 1999) can be observed at radio wavelengths, but only for strong fields ($B > 200$ Gauss, typically above sunspots). Other techniques utilize the Hanle effect, which is the rotation of the polarization of light from a source behind the corona. The degree of rotation depends on the strength of the magnetic field through which the light passes, allowing the observer to infer the magnitude of the coronal magnetic field (Bommier & Sahal-Bréchot, 1982; Querfeld & Smartt, 1984; Sahal-Bréchot et al., 1986; Faurobert-Scholl, 1994). The Hanle effect has been successful in providing constraints on the magnetic field in solar prominences (Faurobert-Scholl, 1994; López Ariste et al., 2005; Derouich et al., 2010). Both methods work well for localized measurements, but are impractical for measuring the large-scale coronal field.

The most promising avenues for comprehensive measurements of the coronal magnetic field return to the Zeeman effect, and rely on forbidden emission lines at infrared (IR) wavelengths (Judge, 1998; Casini & Judge, 1999; Judge et al., 2006). Although the Doppler widths of such lines can exceed the Zeeman shifts by as many as 3 orders of magnitude, careful measurement of the wavelength differential and polarization state, performed with high signal-to-noise ratios, can yield data of sufficient quality

to measure the line-of-sight component of the magnetic field (Judge, 1998). The linear polarization of the Fe XIII (10747 Å) and Fe XIV (5303 Å) lines was initially used to establish only the direction of the coronal magnetic field (Mickey, 1973; Querfeld & Smartt, 1984; Arnaud & Newkirk, 1987), and the 10747 Å line was subsequently used to measure the coronal magnetic field strength along a single line of sight (Lin et al., 2000). The Solar Observatory for Limb Active Regions and Coronae (SOLARC) measures the full linear and circularly polarized Stokes intensities at near-IR wavelengths ($1 - 2.5$ μm, Lin et al., 2004), and has succeeded in mapping the coronal magnetic field for a $5' \times 2.5'$ field of view extending from 0.1 to 0.45 solar radii above the limb (edge of the solar disk).

The Coronal Multi-channel Polarimeter (CoMP) provides observations similar to those from SOLARC, but has the advantage of a larger field of view: it provides magnetograms spanning 2.8×2.8 solar radii (or 0.7×0.7 degrees) at spatial resolution of $4.5''$ per pixel (Tomczyk et al., 2008), compared with SOLARC's $5' \times 2.5'$ field of view and spatial resolution of $20''$ per pixel (Lin et al., 2004). Originally demonstrated at Sacramento Peak Observatory in New Mexico, CoMP measures the complete polarization profiles of two coronal Fe XIII lines at 10747 Å and 10798 Å, as well as the chromospheric He I line at 10830 Å (Tomczyk et al., 2008). These measurements provide the magnetic field strength along the line of sight and the field direction in the plane of the sky. CoMP also uses Doppler observations from the line wings to measure the plasma velocity along the line of sight, and calculates the density in the

plane of the sky from the ratio of the two Fe XIII lines (Penn et al., 1994; Tomczyk et al., 2008). The instrument has now been moved to its permanent home at the Mauna Loa Solar Observatory in Hawai'i, and began taking data in July 2010.

Because the spectral lines used by these instruments are only visible off the edge of the solar disk, both SOLARC and CoMP only measure the magnetic field above the limb. In the absence of complementary observations of the photospheric field at the limb, these coronal measurements may be of only limited use in improving our understanding of phenomena such as prominences. Prominences are large quantities of material similar in composition to the chromosphere, suspended in the low corona and observed in emission above the limb. The same feature is also known as a filament when observed in emission on the solar disk. In some cases, filaments have been associated with coronal mass ejections (CMEs, Jing et al., 2004; Li & Luhmann, 2006; Zhou et al., 2006), although CMEs may occur in the absence of filaments, and likewise, filaments may exist without producing a CME.

2.1.3 Supplemental Observations: Coronal Imaging

CoMP has the potential to advance our knowledge of the above-limb coronal magnetic field substantially, but large scale measurements of the coronal field are still in their infancy. Historically, our ability to observe the coronal field has been severely constrained by the limitations of the small-scale field measurement techniques described above. Because of the low plasma beta of the corona, which forces the

plasma to flow along the field and trace out the field's structure (see Chapter 1), we can observe the large-scale structure of the field in EUV and X-ray images; but these observations, too, have their limitations.

The corona is optically thin to EUV and X-ray emission, meaning that the light is minimally scattered or absorbed along the line of sight. Thus, when imaging the corona in the EUV and X-ray, we observe the sum of all emission along the line of sight. Although we can distinguish two-dimensional features in the plane of the image, we can extract no information regarding the third dimension of the structure, and therefore cannot determine the true three-dimensional structure of the field. The *Solar Terrestrial Relations Observatory* (STEREO) addresses this difficulty by observing the Sun from two different vantage points, allowing stereoscopic reconstruction of three-dimensional coronal structures. The STEREO mission is discussed in more detail in Section 3.3.

Observations of the corona are beset by further ambiguity in the temperature of the plasma being observed. While spectroscopy has high energy resolution, it typically has poor spatial and temporal resolution, which frequently renders it inadequate for detailed study of large-scale coronal structures. The imaging instruments on satellites such as SOHO, the *Transition Region and Coronal Explorer* (TRACE), *Hinode*, and the *Solar Dynamics Observatory* (SDO) therefore use direct imaging to examine coronal geometry and dynamics at EUV and X-ray wavelengths.

X-ray imaging uses grazing incidence optics, generally with a large range of ob-

served wavelengths (e.g. 2 - 200 Å for the X-Ray Telescope on board *Hinode*, Kosugi et al., 2007). EUV imaging uses normal incidence optics with multilayer coatings that act as filters in order to restrict the range of wavelengths that pass through the telescope. These coatings permit narrower bandpasses than those involved in X-ray imaging (1.1 - 14 Å for the channels observed by the Atmospheric Imaging Assembly on board SDO, see Soufli et al., 2005). Each bandpass is generally chosen to encompass a particular spectral line emitted by material at a specific temperature. An image captured in that bandpass therefore portrays the line-of-sight summation of all visible plasma at the wavelengths that the filter is designed to observe.

Confusion can arise when the bandpasses, which are broader than the widths of the lines they target, span wavelengths that include additional lines from material at different temperatures. The 195 Å filter used by instruments such as SOHO's Extreme Ultraviolet Imaging Telescope (EIT), TRACE, and the Extreme Ultraviolet Imagers (EUVI) on board the STEREO spacecraft has contributions from two different lines at different temperatures. The primary contribution is from the Fe XII line, associated with material at 1.5 MK; the secondary contribution is from the Fe XXIV line (192 Å), which is associated with material at 20 MK (Delaboudinière et al., 1995; Handy et al., 1999; Phillips et al., 2005; Wülser et al., 2004). The temperature response function of the TRACE 195 Å filter is shown in Figure 2.2. Under most circumstances, this additional contribution does not pose a substantial problem. During solar flares, however, plasma temperatures can easily reach 20 MK. At such

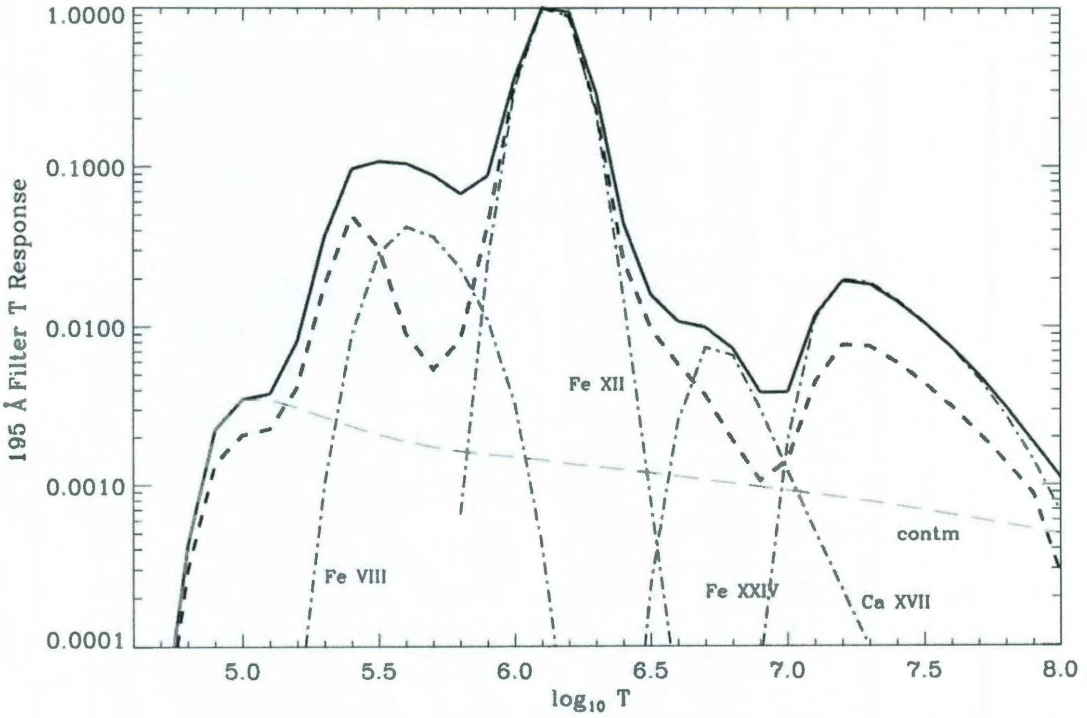

Figure 2.2: Temperature response function and contributions for the TRACE 195 Å filter, calculated by Phillips et al. (2005, solid line) and Handy et al. (1999, thick dashed line). The contributions from different emission lines are shown by dot-dashed lines. The thin dashed line shows continuum emission (modified from Phillips et al., 2005).

times, despite the filter's higher sensitivity to the cooler Fe XII line, emission from the hotter Fe XXIV line can dominate the images in the 195 Å channel.

In addition to the potential ambiguity of observing multiple different temperatures in one wavelength band, the finite width of filter bandpasses also poses the reverse problem: it can be unclear whether a dynamic effect observed in one wavelength is due to variations in the plasma density or fluctuations in temperature. An area of the corona that appears dark in a given wavelength may seem to have very low density compared with neighboring bright plasma, when in fact it contains plasma that is

simply too cool or too hot to emit in the observed wavelength. We can address this problem in part by comparing cotemporal observations in multiple wavelengths[1], but these comparisons cannot fully resolve the confusion.

Furthermore, because we can view the structure of the field only where there is plasma emitting at a wavelength that we observe, we typically cannot infer the field geometry outside of active regions, where the plasma is not sufficiently hot to emit in the EUV or X-ray. As a result, although through EUV and X-ray imaging we can observe locally well defined structures that trace the morphology of the field, imaging shows us only hints of what we require for a complete understanding of the field. The properties of the instruments that we use to view the corona, coupled with the physical characteristics of coronal plasma, limit our observations such that we see the field's structure in only a fraction of the overall corona. Moreover, because the corona is optically thin, the small amounts of structure that we can observe are generally restricted to two dimensions. Thus, it is generally very difficult to extract from individual images either the full three-dimensional structure or the magnitude of the field. We are not so limited, however, when dealing with *pairs* of images taken from different vantage points. This scenario will be discussed further in Chapter 3.

[1]The comparison of cotemporal multithermal observations is one of the objectives of the SDO mission, which is discussed further in Chapter 5.

2.2 Modeling Coronal Magnetic Fields

The challenges associated with coronal imaging, and most measurements of the coronal magnetic field, make these observations an inadequate substitute for conclusive, large-scale measurements of the field itself. Observations of the coronal field are generally supplemented with numerical simulations and analytical models based on certain assumptions about the nature of the field (e.g. that it is force-free; see Appendix B). These efforts allow us to test our theoretical understanding of the field against observationally derived constraints for the models, which can then help validate or refute our theories regarding the field.

The construction of a comprehensive model of the coronal magnetic field is not, however, without complications. Because the plasma temperature and density vary widely from the photosphere through the corona, and because the magnetic field strength decreases with increasing height above the photosphere (Table 1.1), the plasma beta (see Chapter 1) changes dramatically with height. The range of beta for different regimes of the solar atmosphere is shown in Figure 2.3. In the photosphere, we have $\beta > 1$, meaning that the plasma pressure exceeds the magnetic pressure, and the plasma dominates the field. In the chromosphere, the plasma beta experiences a drastic change as the temperature increases and density decreases, until at the base of the corona we have $\beta < 1$.

In the low corona, the low-beta nature of the plasma indicates the importance of the magnetic field, which dominates the plasma and forces it to flow parallel to the

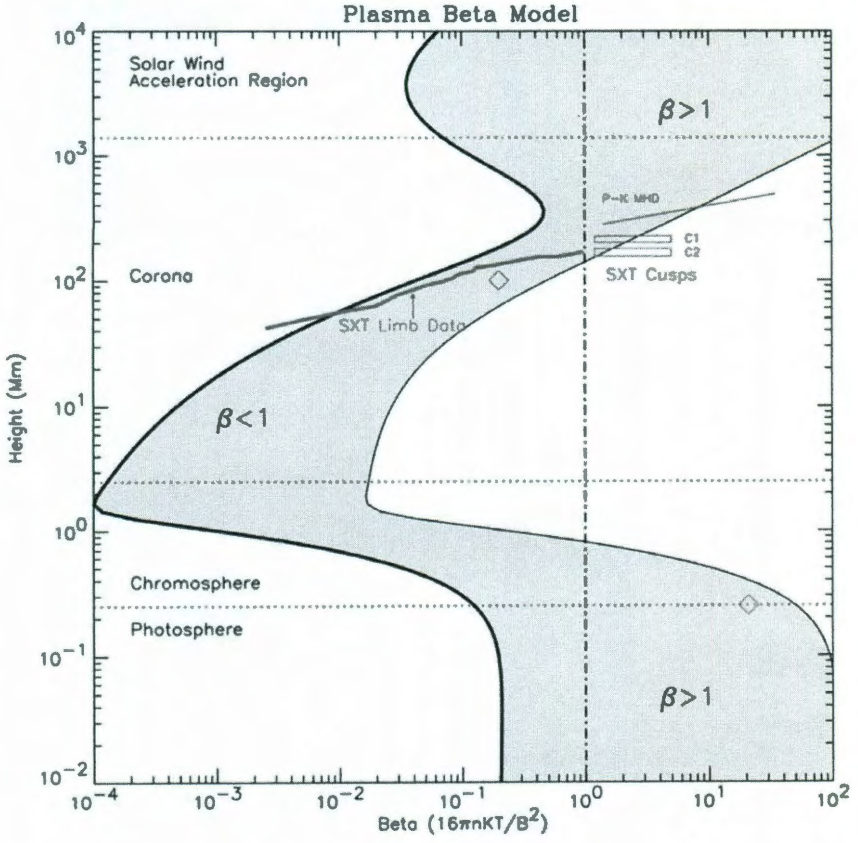

Figure 2.3: Variation of the plasma beta over an active region (Gary, 2001b).

field. High in the corona, the influence of the solar wind drives the increase of the plasma beta until it returns to $\beta \simeq 1$. The variation of the plasma beta by two or three orders of magnitude over the course of the solar atmosphere makes it prohibitively difficult to develop a comprehensive model that deals with all of the different atmospheric regimes. Models that concentrate on the low-beta corona inevitably neglect the physics of the relatively high-beta photosphere and outer corona, and models that assume a high value of beta cannot accurately recreate the field structures that we observe in the EUV and X-ray.

2.2.1 Numerical Simulations

Given its complexity, the most complete approach to modeling the Sun's atmosphere involves a full solution of the magnetohydrodynamic (MHD) equations. MHD simulations of the photosphere and its connection to the corona are an area of very active current research (see, for example, Abbett & Fisher, 2003; Abbett, 2007; Fang et al., 2010). At present, however, the demands of the full extent of the physical processes involved in the dynamic atmosphere exceed our computational abilities.

Certain advances in computational techniques have helped alleviate some of the extraordinary computational burden imposed by MHD simulations of the corona. Adaptive mesh refinement (AMR, see Berger & Oliger, 1984; Berger & Colella, 1989) allows the non-uniform, potentially dynamic discretization of the simulation domain into a variable mesh. The variable size of the individual grid elements allows the simulation to examine certain areas with a high degree of detail, whereas other, less complicated areas may be covered by a coarser grid. This prioritization has proved particularly useful in resolving the small scale heights (100 km) characteristic of regimes such as the photosphere, as well as the narrow extent of the transition region between the chromosphere and corona. AMR improves economy of memory and computational time, facilitating simulations that are locally more detailed but require computational power that is equal to or less than simulations performed with a static grid (Plewa et al., 2005).

Even with this improvement, however, we still cannot adequately resolve the range

of physical processes at work in the Sun's atmosphere. Furthermore, the limited resolution of MHD simulations restricts the degree to which numerical simulations can be compared with observations. While the computing power at modelers' disposal is continually increasing, it cannot yet match the spatial and temporal resolution of solar telescopes. Simulations therefore struggle to incorporate the resolution required for a meaningful comparison between simulation and observation.

2.2.2 Magnetic Field Extrapolations

Although MHD simulations are best suited to capturing the scope of the physics involved from the photosphere through the high corona, the computational burden involved has led solar physicists to develop alternative techniques that simplify the modeling process while preserving some of the physics of MHD simulations. Altschuler & Newkirk (1969) and Schatten et al. (1969) introduced the concept of a *source surface*, a mechanism meant to approximate the effect of the solar wind in the high corona, which has proved reasonably successful in addressing the disparity between the low-beta low corona and the high-beta upper corona.

In the source surface model, an upper boundary condition is imposed at which the magnetic field is required to be radially directed. This boundary condition is typically a spherical shell, referred to as the source surface, positioned at a certain distance (usually 2.5 solar radii, 2.5 $R_{\odot}$) from the center of the Sun. The requirement that the field become radial at this point is meant to simulate the effect that the solar

wind has on the magnetic field lines. At this height in the real corona, the plasma beta returns to approximately unity, with the plasma motions once again dominating the field. The solar wind drags the field lines with it as it flows outward into the heliosphere, until the field lines become effectively radial. Thus, the source surface technique simulates the morphological effects of the solar wind on the magnetic field via an analytical solution, without recourse to MHD simulations.

In general, the field inside the source surface may contain electrical currents. In practice, it is often expedient to choose a potential, or current-free field (see Appendix B). This special case of the more general, current-carrying class of source surface models is referred to as the Potential Field Source Surface (PFSS) model. Figure 2.4 demonstrates the structure of a PFSS field. In this model, the field inside the source surface is potential ($\mathbf{B} = -\nabla\chi$ for $r < R_s$, where R_s is the location of the source surface), and the field at the source surface is purely radial ($B_\theta = B_\phi = 0$ for $r = R_s$).

The PFSS model has enjoyed popularity due to its ease of use and overall effectiveness in modeling the large-scale coronal magnetic field. Nevertheless, the source surface as it is generally adopted has a tendency to oversimplify even the region it was designed to model. Regardless of the activity level of the Sun, the radius at which the field becomes radial in the real solar atmosphere is not constant (Gary, 2001b). As seen in Figure 2.3, the height at which the plasma beta returns to unity varies substantially at any given heliographic location. The assumption of a spherical

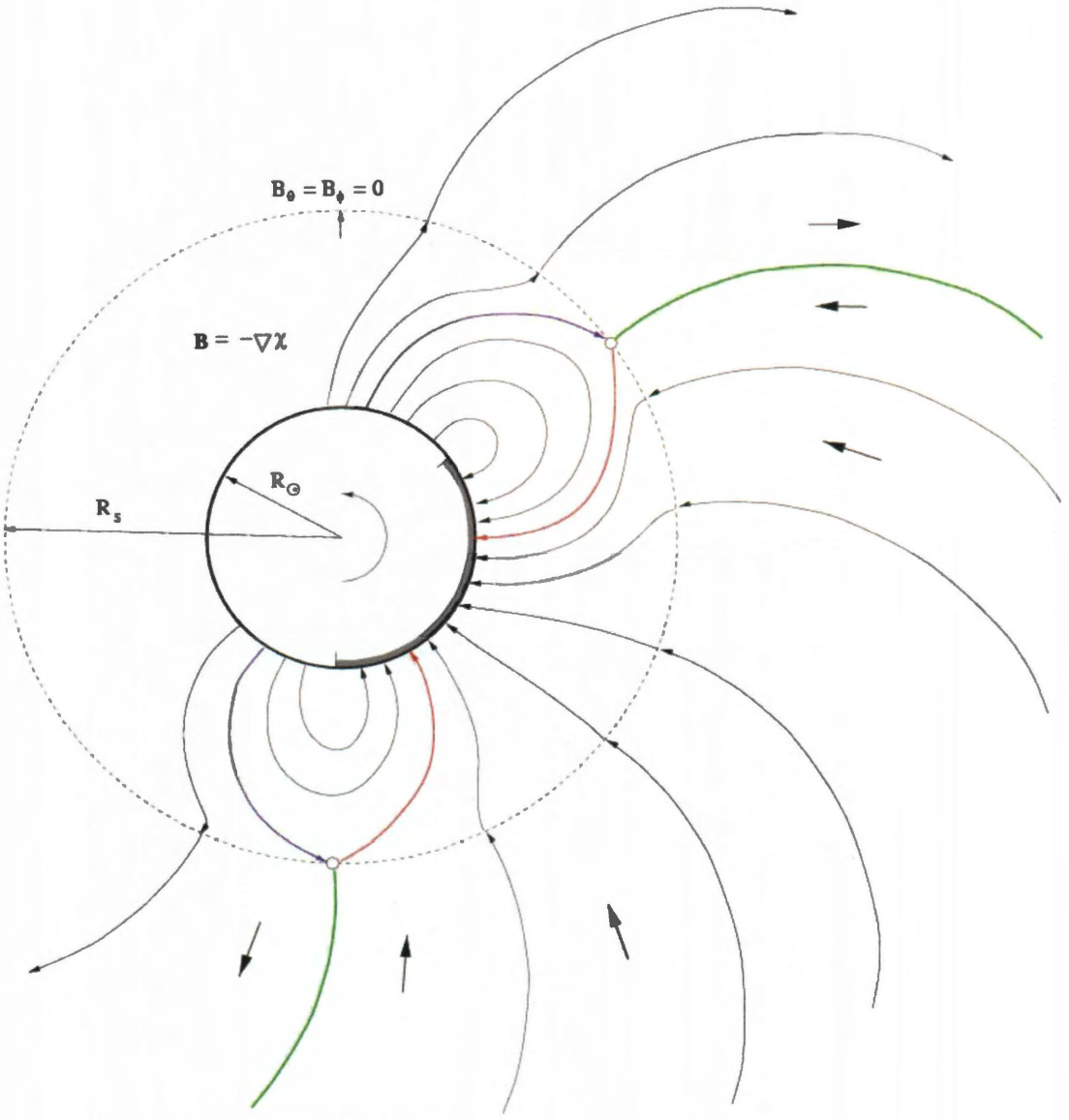

Figure 2.4: Geometrical representation of the Potential Field Source Surface (PFSS) model. Inside the source surface ($r < R_s$), the field is potential; outside the source surface ($r > R_s$), it is permitted to be non-potential. The field is required to be radially directed at the source surface, $r = R_s$ (Longcope, 2005).

source surface therefore underestimates the complexity of the high corona. Furthermore, while the PFSS model is relatively successful at modeling the morphology of the global magnetic field, it has difficulty modeling the low corona. Gary & Alexander (1999) demonstrated that the PFSS model produces inadequate radial stretching of the field at low altitudes. In general, the PFSS model often proves ill suited to reproducing the complicated topology that is characteristic of active region magnetic fields (see Chapters 3-4).

The PFSS model is one example of a *magnetic field extrapolation*, in which the three-dimensional model magnetic field is extrapolated from a set of boundary conditions. These boundary conditions are typically based primarily on magnetic field maps derived from photospheric magnetograms obtained from ground- or space-based observatories. Coupled with certain assumptions describing the field, e.g. $\nabla \times \mathbf{B} = 0$ in the case of a potential (current-free) field, the observational field components form the basis of the full three-dimensional field. The construction of the field can be done with any of a number of extrapolation techniques, such as the popular Green's function or eigenfunction expansion methods (see, for example, Altschuler & Newkirk, 1969; Sakurai, 1982; Seehafer, 1982, and the special volume of *Solar Physics*, Volume 174, No. 1-2, August, 1997).

Other magnetic field extrapolation methods pursue a more general class of magnetic fields: rather than requiring that the field be current-free, they require that the field be *force-free*, i.e. that the Lorentz force is negligible ($\mathbf{F}_L = \mathbf{j} \times \mathbf{B} = 0$). In this

class of fields, electrical currents are permitted, but they must be directed parallel to the magnetic field. In order for this requirement to be met, the current density, $\mathbf{j}$, and therefore the curl of the field, $\nabla \times \mathbf{B}$, must be proportional to the field itself:

$$\mathbf{j} = (\nabla \times \mathbf{B}) = \alpha \mathbf{B} \tag{2.1}$$

where α is a parameter that may be constant or spatially varying (see Appendix B). The most general type of of force-free field is the *non-linear force-free field.* A more restricted class is the *linear force-free field*, and a special case of the force-free field is the *potential*, or current-free field, for which $\alpha = 0$. These distinctions are discussed in greater detail in Appendix B.

Because the corona is generally assumed to carry currents (Schrijver et al., 2005), models that permit the inclusion of currents are thought to be better suited than potential field models to modeling active region magnetic fields. Unlike the source surface model, which has two pre-determined boundary conditions (the photospheric magnetogram at the lower boundary and the source surface at the upper boundary), force-free models are based primarily on the lower, observed, boundary condition. The assumption of force-freeness may not, however, be adequate to describe the corona, particularly outside of active regions (Schrijver et al., 2005). Moreover, choices made regarding boundary conditions for the model domain (e.g. that the field is potential at the side boundaries, as in DeRosa et al., 2009) may impair the models' success in reproducing the true coronal field structure.

The problem of defining suitable boundary conditions is particularly notable because of the virtually universal practice of basing the lower boundary condition on a photospheric magnetogram. We have no reliable observations of the field in either the upper chromosphere, where the environment begins to be force-free (Metcalf et al., 1995), or the lower corona, our region of interest. The only available large-scale measurements of the solar magnetic field are taken at the photosphere, and it is these measurements that, out of necessity, models typically use as the basis for coronal field extrapolations. The use of these photospheric magnetograms for coronal magnetic modeling poses a critical problem: whereas the extrapolated coronal field is assumed to be force-free, the boundary condition used to initialize that extrapolation is based on observations of a region of the Sun that is *non*-force-free (Metcalf et al., 1995). This fundamental inconsistency undermines the effectiveness of the models (DeRosa et al., 2009) and points to a need for new magnetic modeling techniques, an issue addressed in Chapter 4 of this thesis.

Non-linear force-free fields (NLFFFs), for which the parameter α in equation 2.1 varies with position at the solar surface, have long been considered the most appropriate type of field extrapolation for modeling active regions that display complex topology (Démoulin et al., 1997). In NLFFFs, the parameter that relates the current distribution to the magnetic field, α, is permitted to vary spatially (although it must be constant along an individual line of magnetic force; see Appendix B), making NLFFFs more general than linear force-free fields (LFFFs), in which α is constant

everywhere in the model, and potential fields, where α is presumed to be zero everywhere. For complex active regions, NLFFFs are therefore believed to offer the best opportunity to model the true field geometry. It was a great surprise, then, when a study of nine different NLFFF models of an active region failed to produce closer alignment with the observed field structure than did a potential field model of the active region (DeRosa et al., 2009). Among the primary findings of DeRosa et al. was the need to account for the difference between the non-force-free nature of the photospheric boundary condition and the force-free nature of the corona.

Chapter 4 discusses an alternative method of modeling coronal magnetic fields that avoids the difficulties created by the use of photospheric magnetic field data. The submerged dipole method, developed as part of this thesis, does not directly address the interface between the photosphere and the corona. Instead, it models the field in a way that uses only coronal observational constraints, thereby eliminating the lower boundary condition altogether. The magnetic field due to a dipole (or several dipoles, see Section 4.2) is potential, i.e. current-free, and therefore not always applicable to the real corona. However, it succeeds in lowering the misalignment between the observed and model field structures compared with both the NLFFF and PFSS model (the the PFSS results are discussed in Chapter 3). This lower misalignment may put an upper limit on the degree to which the field is non-potential. The spatial distribution of high misalignment between the model and observed field structure may also indicate the regions of the active region where the strongest currents (and

therefore the free energy) lie. This result supports the finding of DeRosa et al. regarding the importance of resolving the conflict between the non-force-free boundary condition and the force-free model, and will be discussed further in Chapter 4.

Chapter 3

Comparison of Coronal Loop Structures with PFSS Models

Detailed knowledge of the magnetic field is crucial to improving our understanding of both the static and dynamic solar corona. However, studies of the coronal magnetic field have long been constrained by the limitations of observations. Photospheric magnetograms are most commonly available, and are widely used as a lower boundary condition for extrapolations of the magnetic field into the corona, but they are not well suited to modeling the coronal magnetic field because the photosphere is not force-free (Metcalf et al., 1995). Thus, force-free extrapolations of the coronal field based on such boundary conditions are not strictly applicable (Régnier et al., 2002).

The chromosphere becomes force-free at a height of approximately 400 km above its lower boundary (Metcalf et al., 1995), and large-scale observations of the chromo-

spheric magnetic field at this altitude could provide suitable boundary conditions for coronal field extrapolations. At present, however, observations of the chromospheric field are somewhat limited. The Vector Spectromagnetograph (VSM) at the Synoptic Optical Long-term Investigations of the Sun (SOLIS) facility takes only line-of-sight measurements of the chromospheric magnetic field (its vector field measurements are limited to the photosphere). The Imaging Vector Magnetograph (IVM) at Mees Solar Observatory can measure the chromospheric vector field, but has a restricted field of view of $4.7' \times 4.7'$ ($\sim 200 \times 200$ Mm, Mickey et al., 1996), and is not run routinely in this mode.

It has recently been shown that the coronal field can be measured using spectropolarimetry and forbidden emission lines (e.g. Liu & Lin, 2008; Tomczyk et al., 2008), or using radio observations (Brosius & White, 2006). Unfortunately, the field of view of these measurements is often too small to observe complete active regions. Thus, at present the best way toward a comprehensive understanding the coronal magnetic field includes joint exploration of magnetogram-based field extrapolations, magnetohydrodynamic (MHD) simulations, and images of coronal loops in the EUV and X-ray. Comparisons of analytical and numerical models with observational data allow us to refine our theoretical understanding of the field and the overall corona.

3.1 Introduction to Modeling Procedure

In general, analytical models of the coronal magnetic field are based on a boundary condition derived from observation, typically a magnetogram giving either the line-of-sight component or both the line-of-sight and transverse components of the photospheric magnetic field. The field is extrapolated from this boundary into the coronal volume, based on certain assumptions about the nature of the field (such as the nature of any currents present). Some examples of these models and their limitations were discussed in Chapter 2. The field structure resulting from these extrapolations can then be compared with observations, usually direct imaging of the corona at EUV or X-ray wavelengths, which demonstrate the morphology of the plasma tracing the coronal field, to determine the best representation of the 3D field distribution.

In this chapter, we examine a magnetic field model in the context of observations of the EUV corona from the *Solar Terrestrial Relations Observatory* (STEREO, see Section 3.3). The model field is given by a Potential Field Source Surface model (PFSS, see Chapter 2 and Section 3.4.3 of this chapter) and is based on observations of the line-of-sight component of the photospheric magnetic field. This model assumes that the field representing the observed active region loops is current-free, with any deviations of the model from the 3D stereoscopic reconstructions representing the degree of non-potentiality of the active regions studied. In addition to the PFSS model, we test a modified model originally introduced by Gary & Alexander (1999),

in which a potential field, consistent with the line-of-sight boundary conditions, is mathematically transformed under certain physical constraints (e.g. $\nabla \cdot \mathbf{B} = 0$) in an attempt to match the observed structure (see Section 3.4.5).

In the approach used here, the initial potential field is a PFSS field constrained by the observed line-of-sight field at the surface and by the adoption of a source surface at the outer boundary (see Chapter 2). This field is then is subjected to a transformation that consists of a simple radial stretching of the field, and is designed to inject currents into the model system while maintaining the divergence-free nature of the field. This construction allows for simple departures from potentiality that can then be tested against observation. PFSS models have previously been used to study the coronal field both in active regions (Schrijver et al., 2005, 2010) and on a global scale (Wang & Sheeley, 2003; Morgan & Habbal, 2010), but the advent of new, stereoscopic observations from the STEREO mission allows us to analyze the PFSS and other magnetic field models in a manner that more accurately determines the success of the models in reproducing the observed field morphology.

With these new observations we can reconstruct the 3D geometry of the real coronal field (see Section 3.4.2), facilitating a direct comparison between the model and observed field structures. In this study, we quantify the discrepancy between the model field structure and the STEREO reconstructed field geometry. This geometry is derived from the reconstruction of curvilinear structures ("loops") from images taken by the Extreme Ultraviolet Imagers (EUVI) on board the two STEREO satel-

lites. This process is summarized in Section 3.4.2 and discussed in further detail in Appendix D. The differences between the model and observed field geometries (described in Section 3.4.4), provide a measure of the degree to which the real coronal field departs from the current-free (potential) nature of the model field.

We apply this analysis to three *active regions*, which are areas of the corona generally associated with the strong magnetic field of sunspots, and where energetic phenomena such as flares occur. The active regions (ARs) in this study are numbered 10953, 10955, and 10956[1]. We analyze sets of EUVI images for each active region: observations beginning at 23:00 UT on 30 April, 20:30 UT on 9 May, and 12:40 UT on 19 May 2007, respectively. The details of the observations are provided in Table 3.2, and the image processing is summarized in Sections 3.4.1 and 3.4.2. The PFSS model and the radial stretching transformation applied to the PFSS field are described in Sections 3.4.3 and 3.4.5, respectively. The results of the comparison between the observed field geometry and the PFSS and stretched PFSS models are given in Section 3.5.

3.2 Quasi-Stereoscopic Techniques

Coronal imaging at EUV wavelengths has previously provided some observational verification for magnetic modeling (Schrijver et al., 2005; Bobra et al., 2008). It can be of only limited use, however, because the telescopes used were at a fixed point in

[1]The active region numbers are given by the NOAA convention for numbering sunspots, and are used throughout this text to refer to individual active regions.

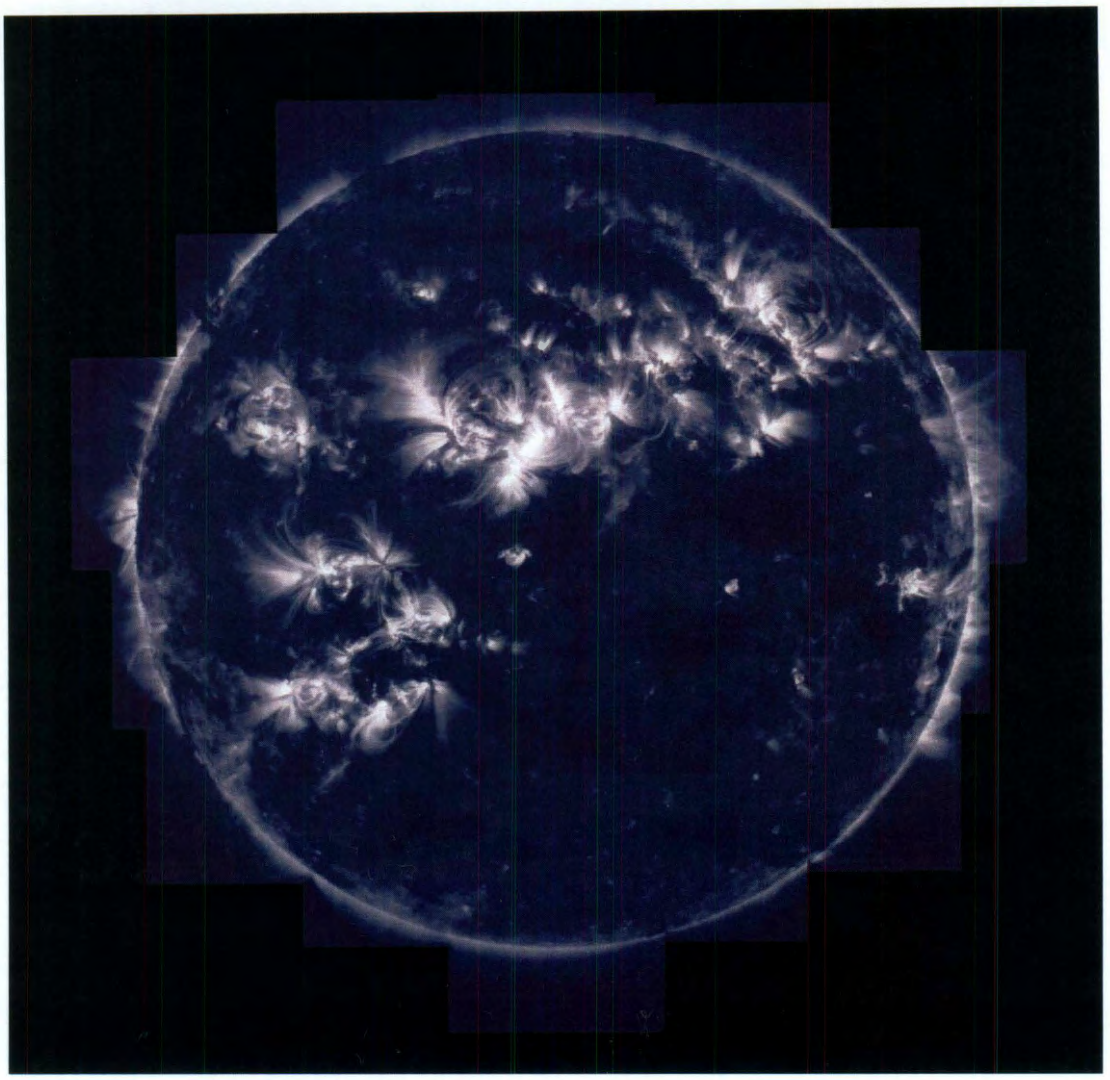

Figure 3.1: A mosaic of multiple TRACE images taken 8 February, 2001 in the 171 Å channel, which is most sensitive to emission from plasma at 1 million Kelvin. Because the TRACE field of view was $8.5' \times 8.5'$ (370 × 370 Mm), multiple TRACE images were combined in order to achieve a full-disk mosaic. (TRACE team.)

space relative to the Sun, so the images are taken from a single vantage point. The corona is optically thin at EUV and X-ray wavelengths, so these images (for example, Figure 3.1) represent a summation of all emitting plasma along the line of sight. As a result, single-viewpoint observations restrict inferences about the magnetic field's configuration to the two-dimensional plane perpendicular to the line of sight. These limitations undermine the extent to which imaging can be used to constrain models of the 3D coronal magnetic field.

There have been some attempts to circumvent the difficulties of single-observer imaging using what are known as *quasi-stereoscopic* techniques. Unlike true stereoscopy, in which simultaneous images from two different points of view are used to achieve the illusion of depth, quasi-stereoscopic methods for coronal study use time-delayed images taken from a single point in space. The *Solar and Heliospheric Observatory* (SOHO), for example, is stationed in a halo orbit about the first Lagrangian point (L1), where the gravitational forces due to the Sun and Earth are balanced (Domingo et al., 1995). The *Transition Region and Coronal Explorer* (TRACE) follows a polar orbit around the Earth (Handy et al., 1999). Both spacecraft move slowly about the Sun, so their movement relative to the Sun is extremely slow compared with the timescales on which the corona changes, and true stereoscopy cannot be performed with observations from either satellite.

Quasi-stereoscopic methods therefore rely on the fact that the Sun rotates, which provides for different views of coronal structures at different times. The Sun has

an average rotation period of $\sim$ 28 days, yielding a daily change in aspect angle of $\sim 13^{\circ}$ as viewed from Earth. Using the parallax created by the varying perspective, it is possible to perform stereoscopic triangulation of an observed feature, thereby obtaining its three-dimensional (3D) structure from sets of two-dimensional (2D) images. This process is discussed in Section 3.4.2, and in further detail in Appendix D.

Solar rotation stereoscopy has been undertaken primarily for large-scale features such as streamers (Koutchmy & Molodenskii, 1992) and long loops connecting different active regions (Berton & Sakurai, 1985). The technique is limited, however, by the requirement that the observed structures be static over the course of the observations. This is generally not a good assumption for a dynamic environment such as the corona, and in particular for active region coronal loops, which are observed to cool with a timescale on the order of hours (Winebarger et al., 2003).

An alternative technique was developed by Aschwanden et al. (1999) in order to account for the dynamic nature of the observed loops. The *dynamic stereoscopy* method allows for the heating and cooling of the plasma in coronal loops, but still requires that the magnetic topology of the region remain unchanged for the duration of the observing period. Aschwanden et al. assume that loops in close proximity to each other run nearly parallel, so although over the course of the observations a given loop may have cooled and become invisible at the observed wavelength, an adjacent loop may be considered to have geometry similar to that of the first loop. Thus, although

individual loops may experience heating and cooling on timescales shorter than the observing period, Aschwanden et al. find that it is possible to perform solar rotation stereoscopy, provided that the overall field topology remains constant. However, although the timescales for changes in the field structure are generally longer than those for the heating and cooling of loops (Aschwanden et al., 1999), the assumption of constant field topology is in general not applicable to active region loops. True stereoscopy requires the use of simultaneous or nearly simultaneous images in order to ensure the identification of identical structures from both perspectives.

3.3 The STEREO Mission

The launch of the *Solar Terrestrial Relations Observatory* (STEREO) (Howard et al., 2008) in 2006 ushered in a new era of coronal observations. With its twin spacecraft, STEREO provides simultaneous images of the Sun from two different vantage points, allowing us to extract 3D information from dual 2D data sets. The two spacecraft, STEREO-A (Ahead) and STEREO-B (Behind), travel in elliptical orbits ahead of and behind Earth, respectively. Their position relative to Earth changes continuously, as their separation angle increases by 45° per year (Howard et al., 2008). Because stereoscopic reconstruction is most accurately performed at spacecraft separation angles of $\theta \lesssim 30°$ (Aschwanden et al., 2008d), the optimum period for stereoscopy was during the first year of the mission.

STEREO's Extreme Ultraviolet Imager (EUVI, Wülser et al., 2004), part of the

Table 3.1. EUV wavelengths and corresponding emission lines observed by the Extreme Ultraviolet Imager (EUVI) on board the STEREO spacecraft.

Wavelength	Emission Line(s)	Temperature of Emitting Plasma
171 Å	Fe IX/X	1.0×10^6 K
195 Å	Fe XII	1.5×10^6 K
284 Å	Fe XV	2.0×10^6 K
304 Å	He II	8.0×10^4 K

the Sun Earth Connection Coronal and Heliospheric Investigation (SECCHI) imaging suite, observes the corona in four EUV wavelengths: 171 Å, 195 Å, 284 Å, and 304 Å. The emission lines associated with these wavelengths, and the temperatures of the plasma producing those emission lines, are summarized in Table 3.1. Each EUVI image is 2048 × 2048 pixels, spanning the full solar disk for total coverage area of 3.4 × 3.4 solar radii, with a pixel size of 1.59 arcsec (1.59″, or ∼ 1156 km, Wülser et al., 2004). EUVI's point spread function, which describes the detector's response to a point source and determines how well the system can resolve such a source, yields an effective spatial resolution of 2 pixels (Wülser et al., 2004).

3.4 Observations and Analysis

3.4.1 EUVI Observations

The data used in this study are sets of image pairs from the EUVI instruments on the Ahead (A) and Behind (B) STEREO spacecraft (see Table 3.2) in three of

the EUVI wavelengths: 171, 195, and 284 Å. The plasma that emits at 304 Å is too cool to fill the loops that trace the field in the corona, so images from this wavelength are not used. The use of three wavelengths facilitates the identification of more loop structures than can be seen in one wavelength alone. In the 171 Å images, one sees only loops at 1.0×10^6 K; in the 195 Å and 284 Å images one sees loops at 1.5×10^6 K and 2.0×10^6 K, respectively, which may display the field structure in areas of the active regions where there is more heating.

The independent pointing and different orbits of the two STEREO spacecraft lead to differences in the images that must be corrected before the images can be used for stereoscopy. The headers of the image files contain the necessary information for making these corrections, such as the location (in pixel coordinates) of the Sun center in the image and the roll angle of the spacecraft at the the time the image was taken. For a given pair of cotemporal image files to be used for stereoscopy, the images are first co-aligned so that the location of the Sun center is identical in both images. The images must then be scaled so that the width of the solar disk is consistent between the two images. The STEREO-A spacecraft travels ahead of and slightly faster than the Earth, and is therefore slightly closer to the Sun than the Earth. Conversely, the STEREO-B spacecraft is slightly farther away due to its slower orbit. As a result, the apparent angular size of the Sun differs between the two imagers, and it is necessary to correct for this effect to ensure accurate triangulation. Finally, to account for the different roll angles of the spacecraft with respect to the ecliptic plane (the plane

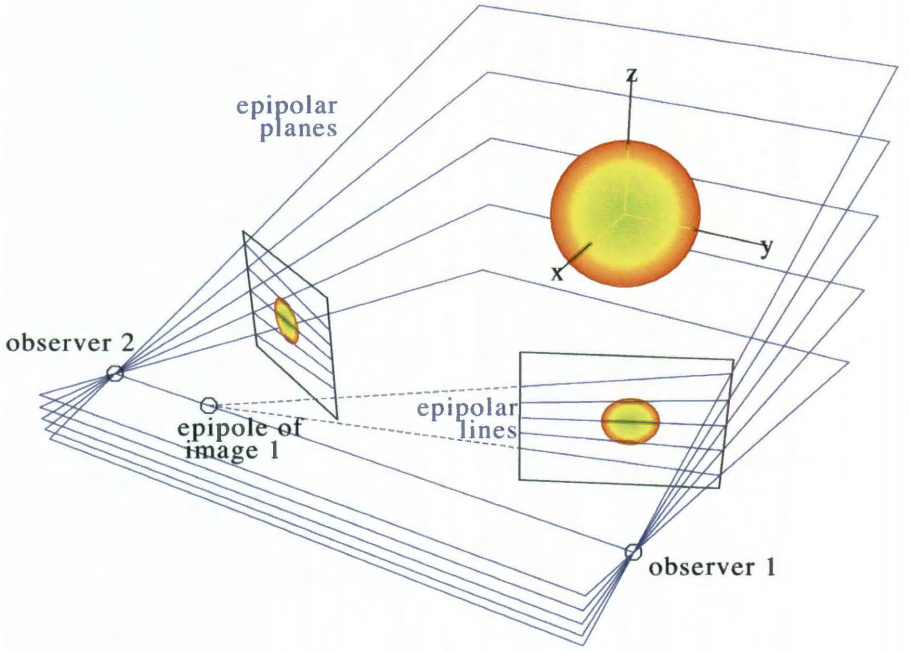

Figure 3.2: Geometry of the epipolar plane. For stereoscopy using STEREO data, observers 1 and 2 are the STEREO-A and STEREO-B spacecraft, respectively (Inhester, 2006).

in which the Earth travels in its orbit around the Sun), the images are rotated so that the solar equator lies parallel to the epipolar plane, which is chosen here as the plane defined by the positions of the Sun center and the two STEREO spacecraft (see Figure 3.2 and Inhester, 2006).

For each active region, an observing period of 20 minutes' duration is chosen, and the images from this period are summed to form an integration over a brief period of time. The summation of images helps to achieve a better signal-to-noise ratio and, because the loop structures are relatively unchanged during this short period,

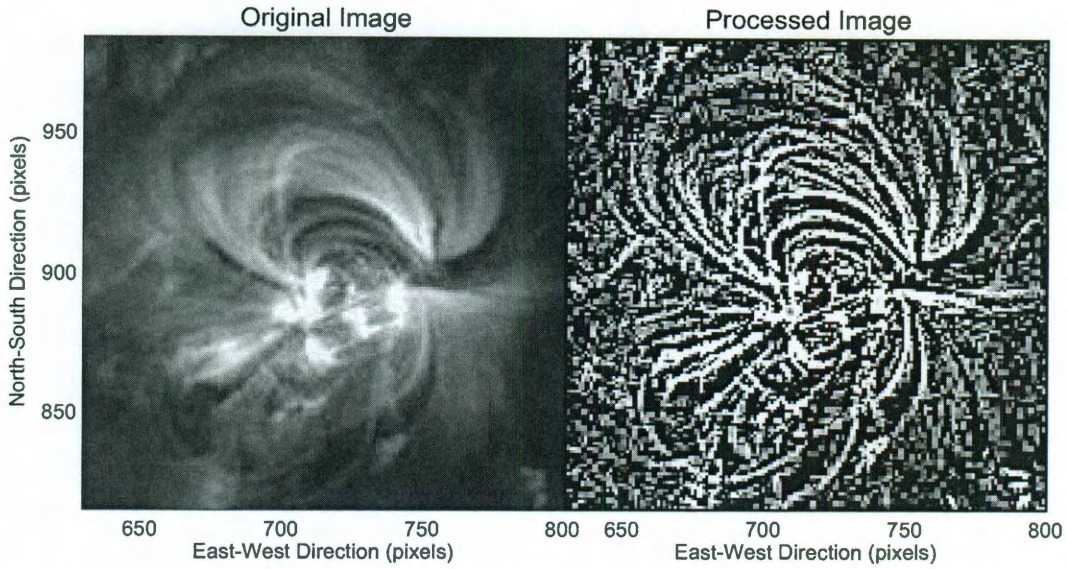

Figure 3.3: EUVI images of AR 10955 in the 171 Å channel. Left: unprocessed image. Right: image after the application of a high-pass filter to enhance feature definition for loop tracing.

does not appreciably degrade the integrity of the image. Images are stacked wherever the cadence is shorter than 20 minutes (ARs 10953 and 10956). EUVI has a typical cadence of 2.5 minutes in the 171 Å channel, yielding eight images in each 20-minute period.

Reliable triangulation of loops depends on the identification of coherent loop structures. It is therefore advantageous to employ image processing techniques that improve the visibility of the curvilinear features traced in the stereoscopy of coronal loops. In this case, a high-pass filter with a variable boxcar smoothing, which subtracts a moving average based on neighborhood pixel values, enhances the feature definition of the images (see Figure 3.3 and Appendix C).

Table 3.2. Observation parameters of STEREO images used for each of the three active regions.

Active Region Number	Observing Times	Spacecraft Separation Angle	Wavelength (Å)	Number of Images	Exposure Time (seconds)	Number of Loops
10953	23:00 – 23:20 UT	6.0°	171	8	2.0	100
			195	2	4.0	50
			284	2	16.0	50
10955	20:30 – 20:50 UT	7.1°	171	1	4.0	30
			195	2	4.0	20
			284	1	16.0	20
10953	12:40 – 13:00 UT	8.6°	171	8	2.0	50
			195	2	4.0	30
			284	2	16.0	20

3.4.2 Stereoscopy

The 3D structure of the loops is extracted from the images by means of stereoscopy tools presented in Aschwanden et al. (2008c). A more detailed description of the triangulation can be found in Appendix D; here the process is summarized only briefly. The loops are identified and traced manually in each image. Although automated loop tracing routines are approaching human effectiveness (Aschwanden, 2010), they generally have difficulty distinguishing real loops from background structures and are often unable to extrapolate small-scale loop elements into long, coherent loop structures (Aschwanden et al., 2008a).

In the manual approach used here, the user traces a given loop first in the Ahead (A) image, then in the Behind (B) image. Each tracing is simply a series of spline points marked manually by clicking a cursor at the appropriate location in the image window (Figure 3.4(a)). Once the A tracing is complete, the user marks the same number of spline points in the epipolar plane (Inhester, 2006) of the B image (Figures 3.4(b) and 3.4(c)). The code then uses the spline points and the spacecraft information to interpolate a curve, and triangulates to find the height above the solar surface of each point along the loop. These steps are repeated until all visible loop structures have been traced, and the loop coordinates are stored in a data file for later use. An example of the traced collection of loops is shown superimposed on the EUVI-A image (Figure 3.5) and the EUVI-B image (Figure 3.6). The 3D active region structure is demonstrated via three views of the traced loops in Figure 3.7.

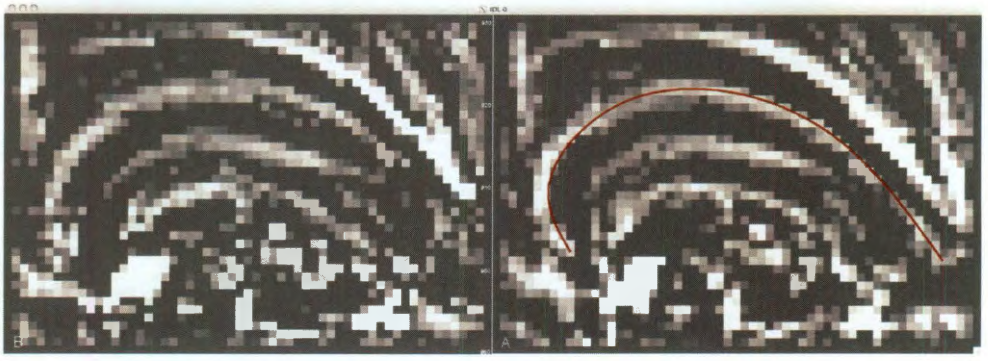

(a) Loop tracing in the EUVI-A image (right). The user clicks on 3-5 points along a loop. The code performs a spline fit to the points, and displays the resulting curve. The B image is shown at left.

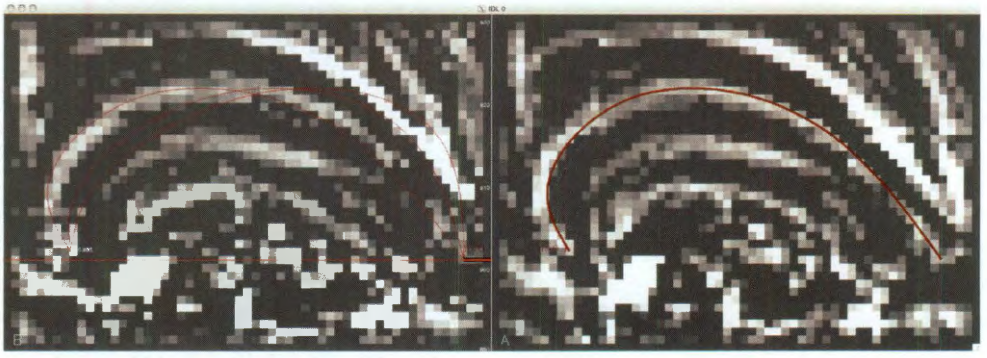

(b) Loop tracing in the EUVI-B image (left). The code plots indicators (thin red lines) of the loop path for different heights. The user must first click on the loop at the initial point (thick red bar). The A image is shown at right, with the curve traced in that image.

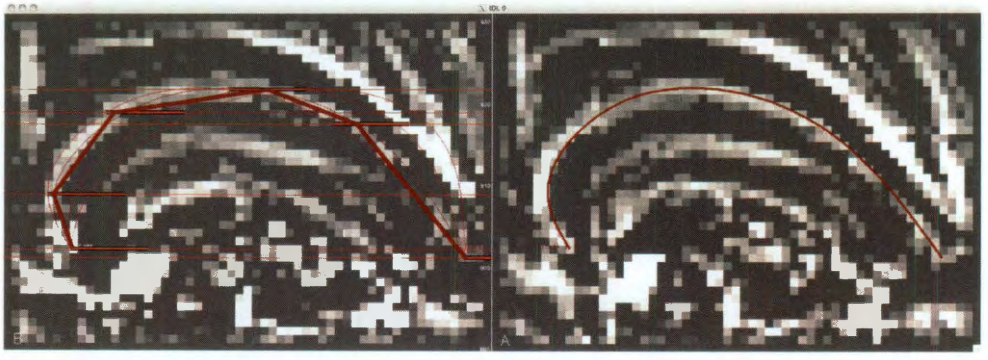

(c) Loop tracing in the EUVI-B image (left), continued. The code provides guides (thick red bars) indicating the range of positions that correspond, at a given point clicked in the A image, to different heights. The user clicks on the points at which the guides intersect the observed loop, and the coordinates are stored. The A image is shown at right.

Figure 3.4: Screenshots of the loop tracing process.

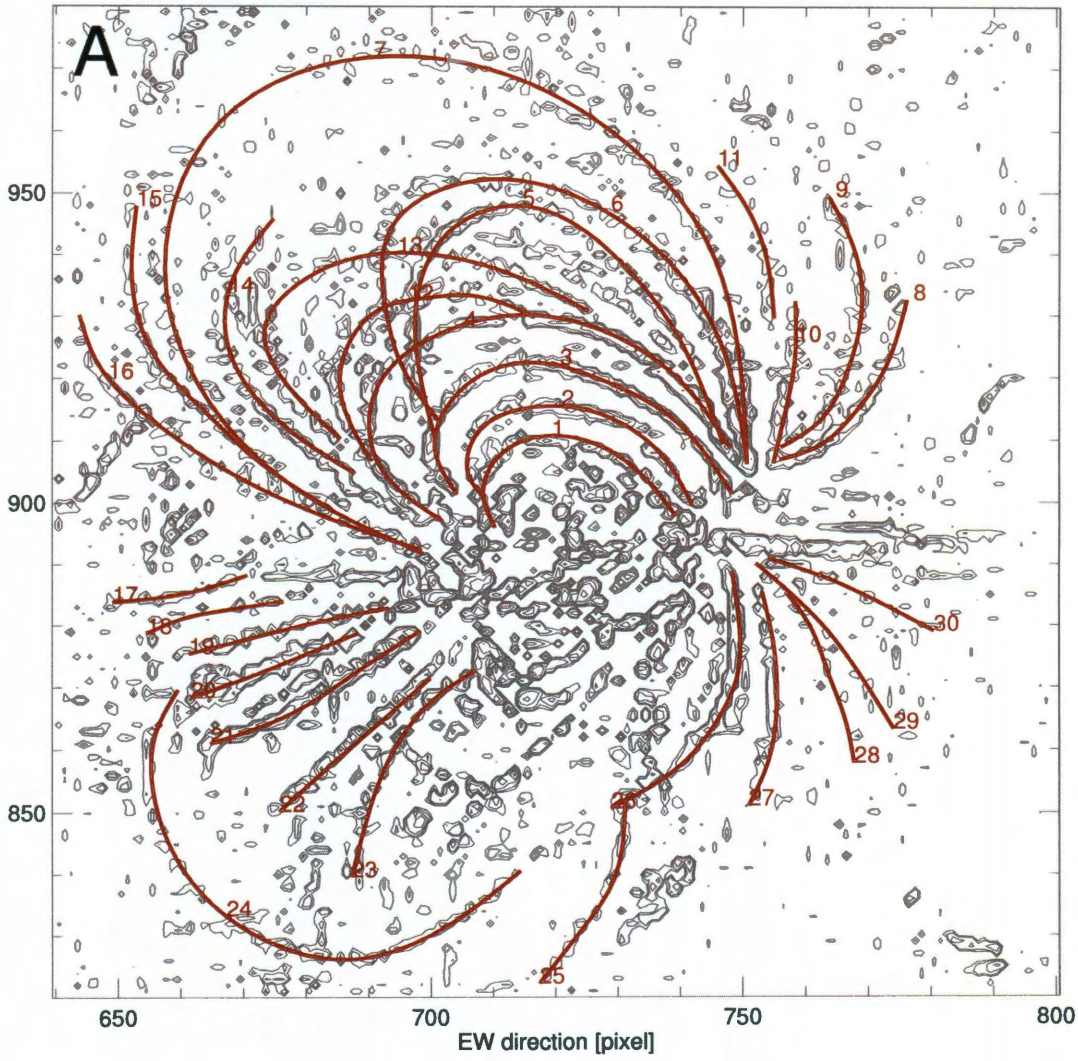

Figure 3.5: Loops traced in the EUVI-A image for AR 10955 (9 May 2007). Background is a logarithmic contour plot of the EUVI-A image, subjected to a high-pass filter as discussed in Appendix C (Aschwanden et al., 2008c).

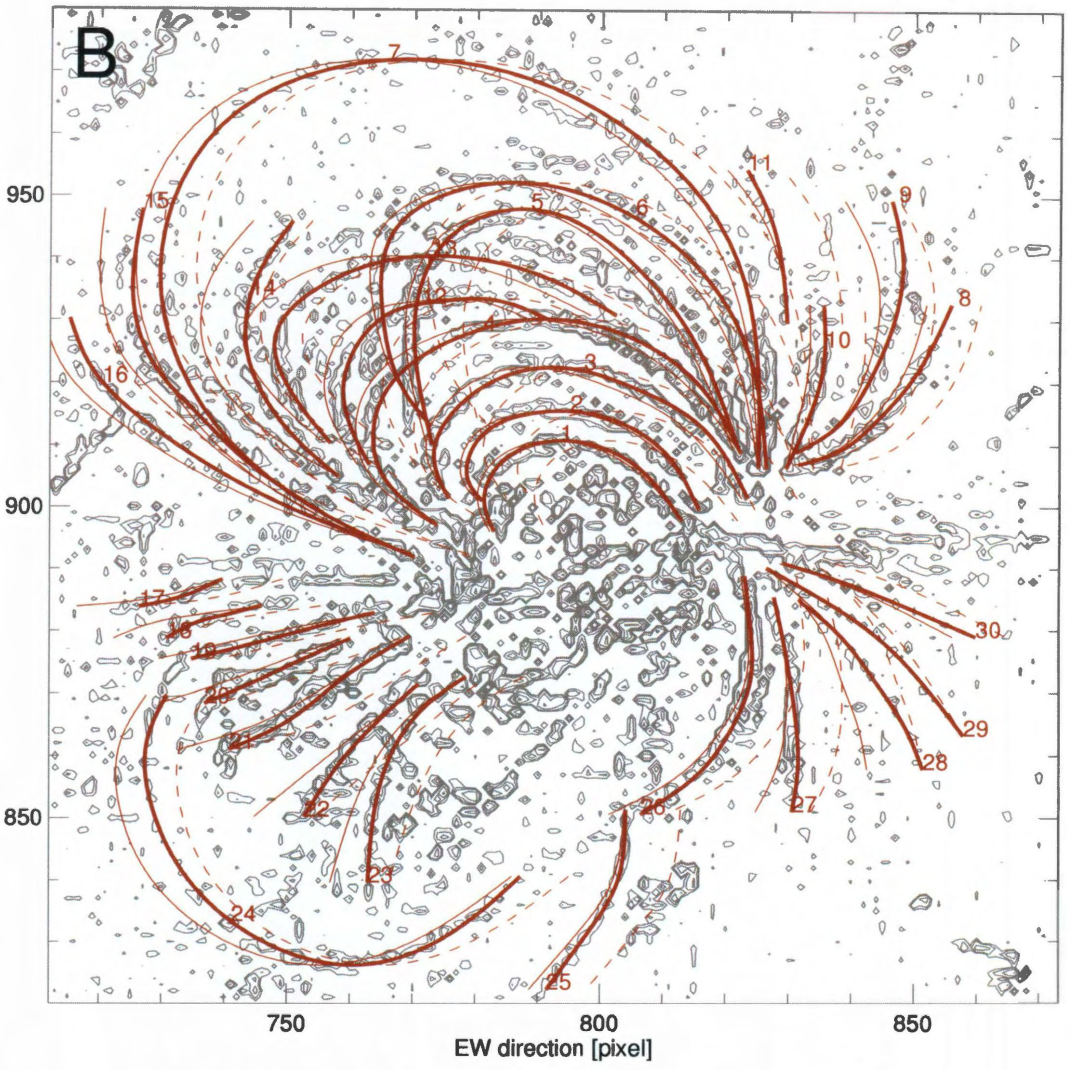

Figure 3.6: Representation is similar to Figure D.4, but for the EUVI-B image. Thick red lines represent the traced loops. Thin solid red lines indicate loop projections, based on curves traced in the A image, calculated for photospheric heights ($h = 0$). Thin dashed red lines indicated loop projections for constant height $h = 0.1R_{\odot}$ (Aschwanden et al., 2008c).

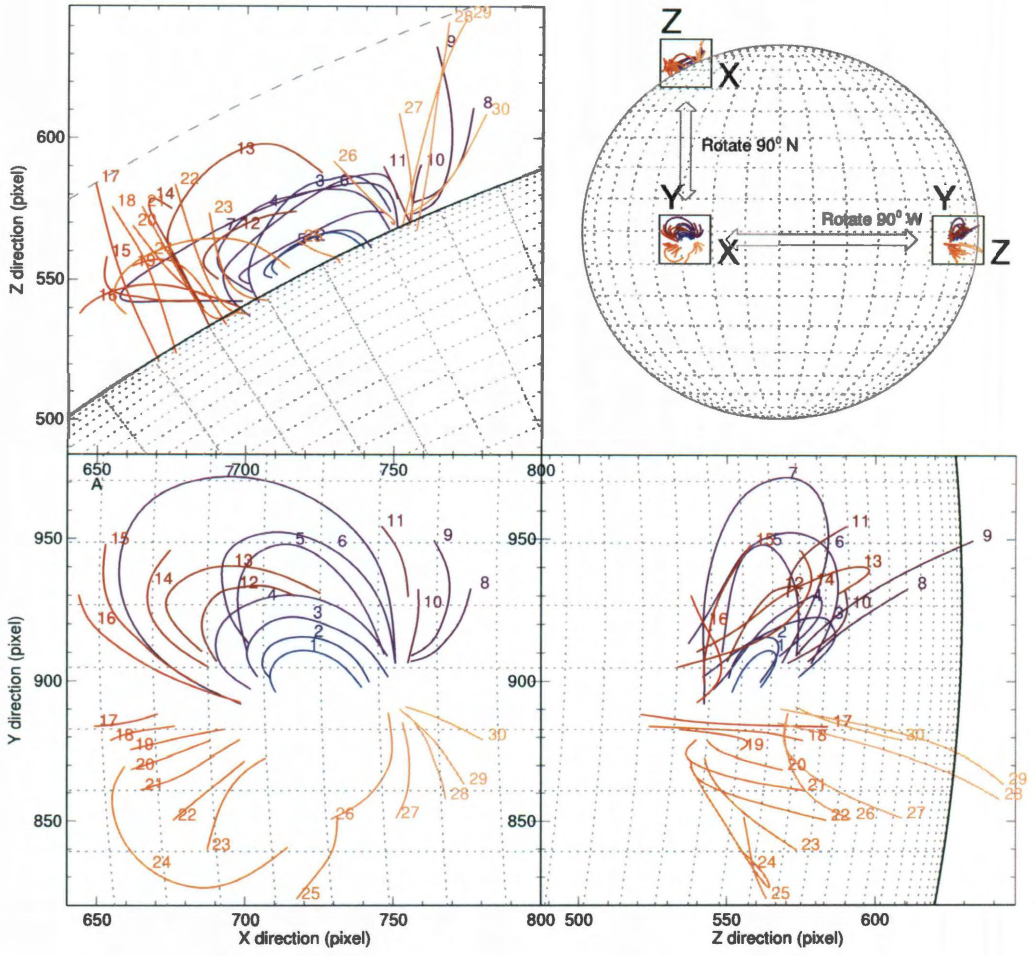

Figure 3.7: Triangulated loops for AR 10955 (9 May 2007) shown from three different perspectives, which are illustrated in the diagram at top right Bottom left: the loops as seen from the EUVI-A spacecraft. Top left: the loops as seen rotated up 90°. Bottom right: the loops as seen rotated 90° to the west (Aschwanden et al., 2008c).

3.4.3 Potential Field Model

With the 3D structure of the EUV loops established from the stereoscopic observations, a model representation of the real magnetic field is calculated for comparison. The potential field model used here is a PFSS model described in Schrijver & De Rosa (2003, and references therein). It imposes a source surface radial constraint at 2.5 $R_{\odot}$ and relies on photospheric magnetograms from the Michelson Doppler Imager (MDI) on SOHO to provide the necessary boundary conditions to compute the 3D field on a regular grid throughout the corona.

For each active region, the vector magnetic field is calculated on a 3D lattice. A regular 1° grid of field line footpoints is defined at the photosphere (points from which lines of force, or field lines, will be traced through the model field), and footpoints are selected in regions where the field strength exceeds 50 gauss. This threshold field strength eliminates weak field from the visualization. The computation of the field lines begins at the footpoints and steps along the lines of force until they return to the solar surface or reach the maximum allowed step count (3000 steps), typically indicating that they have crossed the source surface boundary and are open to the interplanetary medium. These field lines are shown in Figures 3.9 – 3.11. Note that from this point onward, "loop" denotes the *observed* coronal loops traced in EUVI images, and "field line" denotes a line of force traced through the *model* magnetic field.

3.4.4 Comparison of Observed and Model Field Structures

In a system where the plasma beta parameter is small (see Chapter 1), the field inhibits plasma motion across the field, forcing the plasma to flow along the field. Loops observed in the EUV and X-ray in the low corona are therefore believed to trace the structure of the magnetic field. Because the model field structure is known, it is possible to compare the differences in structure between the observed and model fields. The loops therefore provide a means by which one can evaluate the success of the model in representing the real coronal field. The magnetic field vector at a point in space describes the direction of the field at that point, and the coronal loop vectors (vectors that lie tangent to the observed loops) can be considered a dimensionless equivalent of the actual field:

$$\mathbf{b}_{obs}(s) = \frac{\mathbf{B}_{obs}(s)}{|\mathbf{B}_{obs}(s)|} \tag{3.1}$$

where s is the coordinate along a given observed loop. Stepping along each loop, two vectors are identified at every point: the vector tangent to the loop, $\mathbf{B}_{obs}$, and the model magnetic field vector at that particular point, $\mathbf{B}_{PFSS}$. The analog to equation 3.1 for the model field vector is as follows:

$$\mathbf{b}_{PFSS}(\mathbf{r}) = \frac{\mathbf{B}_{PFSS}(\mathbf{r})}{|\mathbf{B}_{PFSS}(\mathbf{r})|} \tag{3.2}$$

The angle between the two vectors, the *misalignment angle* α, provides a measure of the quantitative difference between the observed and theoretical field directions at that point (Figure 3.8). Taking the scalar product of $\mathbf{b}_{obs}$ locally at position $\mathbf{r}$ with the coincident normalized model field vector, $\mathbf{b}_{PFSS}$, it is possible to calculate the angle α between the two vectors:

$$\alpha_i = \cos^{-1}\left(\mathbf{b}_{obs} \cdot \mathbf{b}_{PFSS}\right). \tag{3.3}$$

This *misalignment angle* provides a quantitative measure of the success of the model field in reproducing the structure of the collection of observed loops, i.e. the real field's structure at that point on the loop. When calculated for all points on the loops of an entire active region, the misalignment angle can be used to assess the validity of the model for the active region as a whole: $\alpha = \langle \alpha_i \rangle$ for $i = 1, \ldots, n$, for n the total number of loop points in the active region.

3.4.5 Stretched Magnetic Field Model

The PFSS model described in Section 3.4.3 (see also Section 2.2.2) is one of many examples of the current-free class of magnetic fields known as *potential* fields (see Appendix B). In the real corona, however, the plasma is assumed to carry currents (Schrijver et al., 2005), so it is useful to examine the ability of a *modified* potential field to reproduce the observed field configuration. In general, such a modification is designed to inject electrical currents into the system while preserving the divergence-

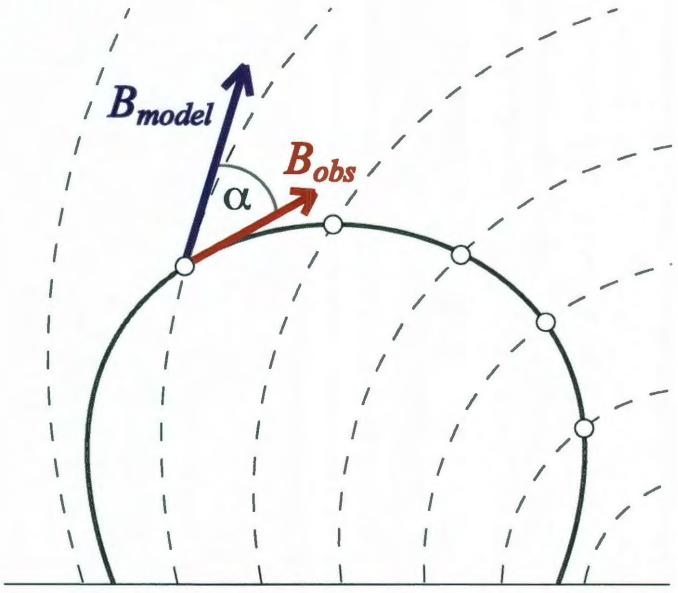

Figure 3.8: Two-dimensional projection of the misalignment angle α between two 3D vectors: The vector $\mathbf{x}_B$ represents the local magnetic field vector and $\mathbf{x}_O$ is the vector tangent to the STEREO loop. The solid line represents an observed STEREO loop; the dashed lines represent the potential field lines. The circle symbols along the observed loop indicate some points at which the field-loop misalignment angle is calculated.

free condition of the field ($\nabla \cdot \mathbf{B} = 0$). The particular transformation used here is a simple radial stretching of the form put forward by Gary & Alexander (1999) to reproduce cusps in active region magnetic fields. The stretching introduces azimuthal currents, rendering the field non-force-free (see Appendix B). The form of the stretching is defined by

$$B'_r = w(r, R_\odot, k) B_r \tag{3.4}$$

$$B'_\theta = v(r, R_\odot, k) B_\theta \tag{3.5}$$

$$B'_\phi = v(r, R_\odot, k) B_\phi \tag{3.6}$$

Here $\mathbf{B} = (B_r, B_\theta, B_\phi)$ is the unstretched (in this case, potential) field, $\mathbf{B}'$ is the transformed field, and the height above the solar surface is given by $h = r - R_\odot$. The functions w and v are defined as follows:

$$w(r, R_\odot, k) = \frac{[h + R_\odot]^2}{[kh + R_\odot]^2} \tag{3.7}$$

$$v(r, R_\odot, k) = \frac{h + R_\odot}{k[kh + R_\odot]} \tag{3.8}$$

where k is an independent variable that determines the degree of stretching induced in the field, with $k = 1$ yielding no stretching. Note that for $h = 0$ (*i.e.* $r = R_\odot$), the function w vanishes, so the radial component of the field is unchanged at the solar surface. This stretching is applied, for varying values of the stretching parameter k, to the potential (model) field of each active region. The resulting fields are no longer potential, but they remain divergence-free. The misalignment angles are then recomputed using the transformed field instead of the original potential field.

3.5 Results

3.5.1 Active Region Misalignment Angles

Figures 3.9 – 3.11 show the potential field lines for each active region (white lines) and the coronal loops that were observed by STEREO/EUVI and traced by hand (red color table). The field lines and observed loops are superimposed on images of the active regions taken by EUVI-A, the EUVI instrument on the STEREO-A spacecraft, at 171 Å. Each loop is drawn in a color that represents the median value of all of the misalignment angles along that loop. A low median misalignment angle along a loop, (*i.e.* better agreement with the potential field) results in a brown to black loop; a brighter yellow to red loop indicates a high misalignment angle and poor agreement with the potential field.

The distribution of these median misalignment angles is shown in Figure 3.12 in the form of a histogram for each active region. A Gaussian curve is fitted to the peak of each histogram, where the peak is defined as follows: the maximum value of the histogram, h_{peak}, occurs at an angle $\alpha = \alpha_{peak}$. The range of $0 < \alpha < 2\alpha_{peak}$ is fitted with a Gaussian. In this way the non-symmetric tails of the distribution are eliminated from the Gaussian fit. The peak has average value $\bar{\alpha}$ and standard deviation σ_α.

The average misalignment angle of each active region provides a measure of the discrepancy between the model field and the observed field configuration. These average angles are noted on each histogram. The variation in angles among the three

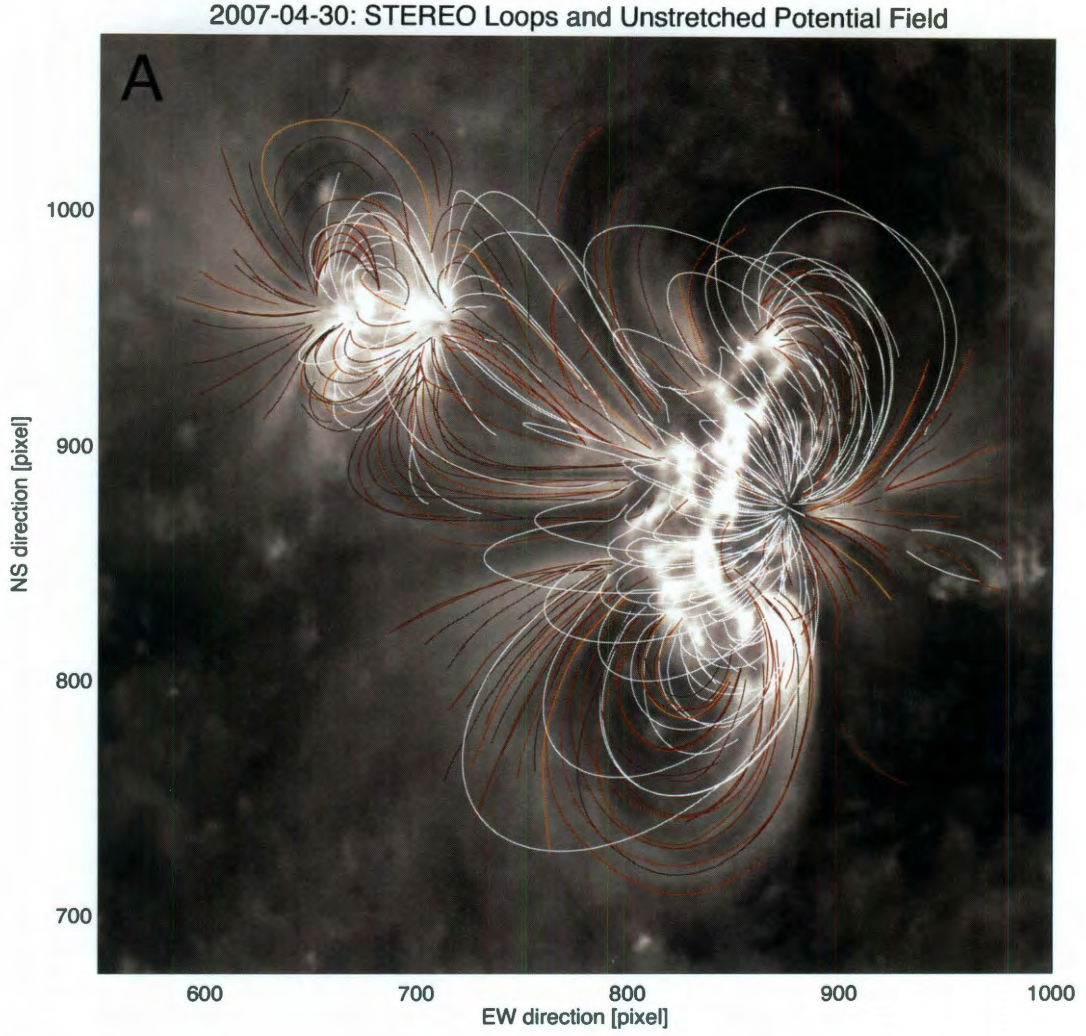

Figure 3.9: Potential field lines (white) and observed EUVI loops (red color table) for AR 10953 (30 April 2007), where the EUVI loop color indicates the median misalignment angle per field line: $\alpha \leq 30°$ (brown), $\alpha \approx 40°$ (red), $\alpha \approx 60°$ (orange), $\alpha \geq 70°$ (yellow). The background image is an EUVI image in 171 Å; lighter areas correspond to brighter regions. Image size is 450×400 pixels, equivalent to 720×640 arcsec or 522×464 Mm. Potential field lines with base magnetic field strength $B_{base} < 50$ G are excluded from this visualization.

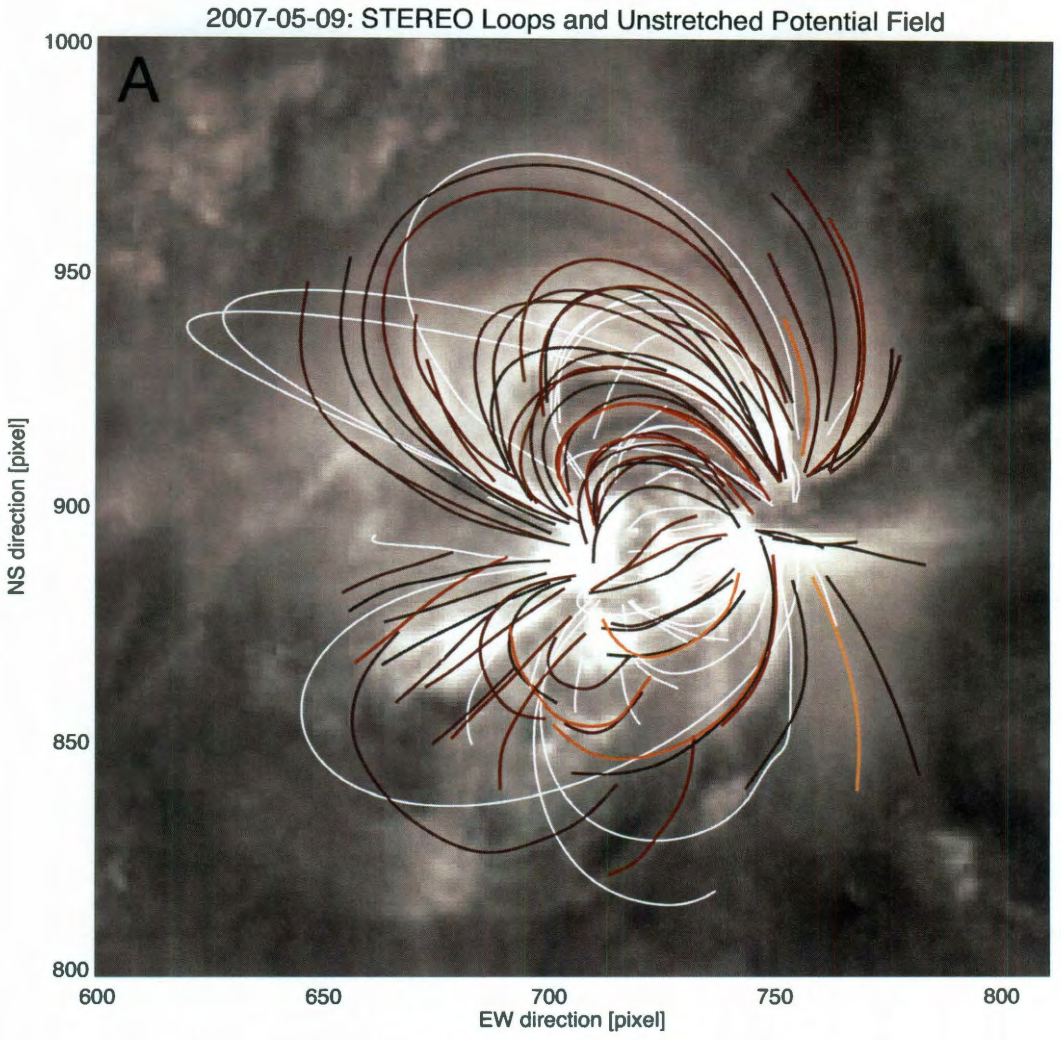

Figure 3.10: Potential field lines (white) and observed EUVI loops (red color table) for AR 10955 (9 May 2007). Image size is 160 × 160 pixels, equivalent to 256 × 256 arcsec or 186 × 186 Mm. Representation similar to Figure 3.9.

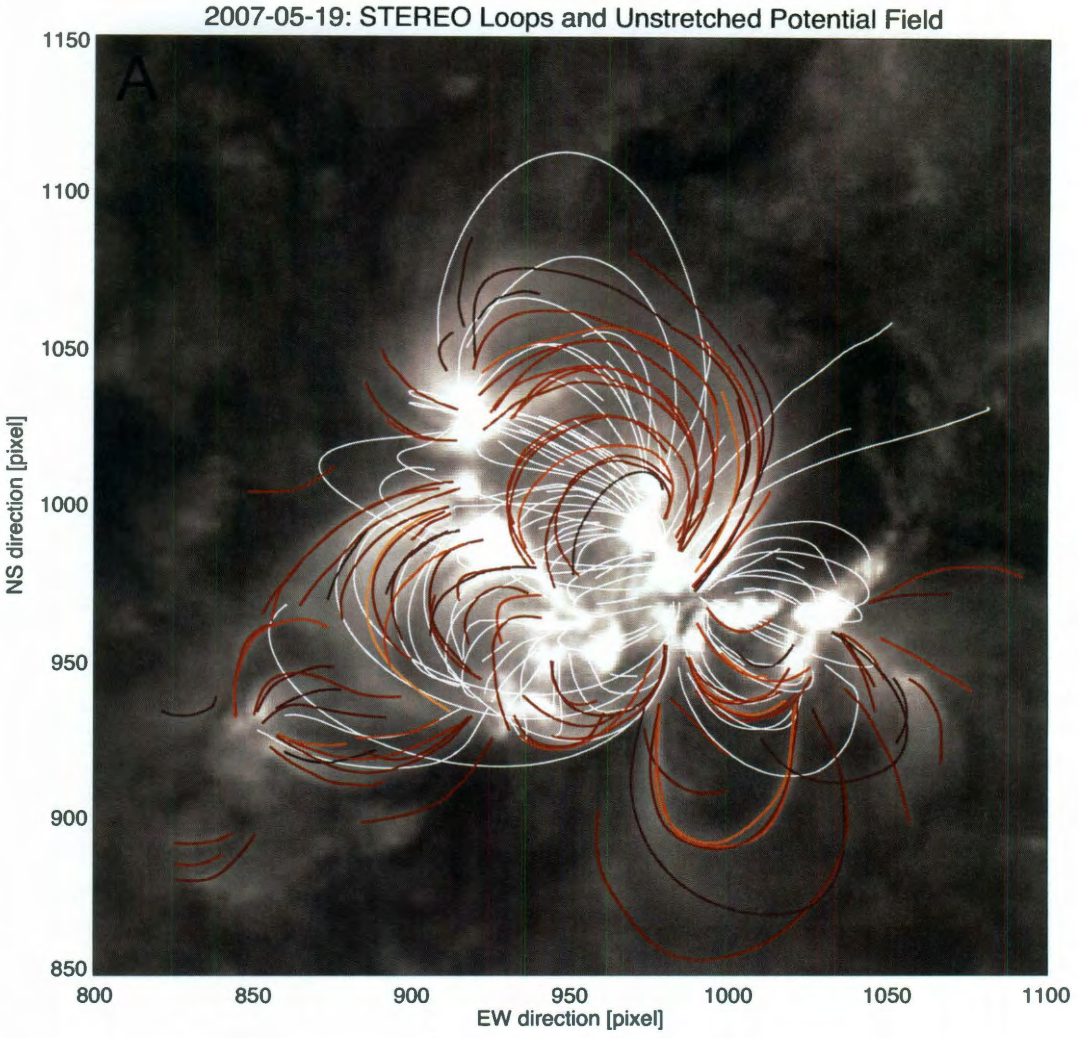

Figure 3.11: Potential field lines (white) and observed EUVI loops (red color table) for AR 10956 (19 May 2007). Image size is 300 × 300 pixels, equivalent to 480 × 480 arcsec or 348 × 348 Mm. Representation similar to Figure 3.9.

active regions indicates that the regions' observed field configurations vary in their proximity to potentiality. With an average misalignment angle of $\bar{\alpha} = 19° \pm 6°$, AR 10955 (9 May 2007) has a field structure that, of the three regions studied, most closely matches the potential field. The active region has a simple dipolar structure, and it is unsurprising that the potential field most closely matches the observed structures in this region.

The field configuration of AR 10953 (30 April) departs further from potentiality with $\bar{\alpha} = 25° \pm 8°$. DeRosa et al. (2009) recently studied AR 10953 using potential and non-linear force-free fields in conjunction with stereoscopically determined 3D loop structures. They tested several non-linear force-free models and, for the model showing optimum agreement with the observed field geometry, found a misalignment angle of 24° for their computational domain, comparable to the 25° misalignment found here. Owing to the small field of view of the *Hinode* observations used to compute their field extrapolations, however, the area of the active region studied by DeRosa et al. is significantly smaller than the area used in this study, which encompasses the entire active region.

AR 10956 (19 May), with $\bar{\alpha} = 36° \pm 13°$, yields the poorest agreement with the potential field. This high average misalignment angle is consistent with its visibly complex multipolar structure. Furthermore, this region produced a minor flare and partial filament eruption that began at 12:50 UT, so the observations used in this study were taken at the time when there was a high degree of stress in the active

region. AR 10953 produced a smaller (GOES B2.6 flare) approximately 8 hours prior to the observations used here, and AR 10955 was quiet during the days prior to and following these observations.

3.5.2 Effect of Radial Stretching

The preceding sections describe the success of the *unmodified* potential field in approximating the observed field configuration. This section examines the effect of the radial stretching (Section 3.4.5) on the fit between the model field and observations. The radial stretching described in Section 3.4.5 (equations 3.4-3.6) is applied to the potential field for each of the three active regions for a range of values of the stretching parameter k, $0.25 < k < 4.0$. A summary of the results of these comparisons with stretched model fields can be found in Table 3.3 for values of $k = 0.5$ and $k = 2.0$.

In cases where the average active region misalignment angle is relatively low, applying a stretching for a large value of k yields a substantially larger discrepancy between the observed loop alignment and the modified model field alignment. For the active region with a high average misalignment angle, however, stretching makes little difference. In general, stretching the potential field prior to calculating the misalignment did not result in significant improvement to the field's agreement with the orientation of the observed loops. This result is not wholly unexpected, as the radial stretching presented here is a simple transformation with minimal spatial dependence. Furthermore, a large radial stretching would imply strong cross-field currents

Table 3.3. Median misalignment angles for different values of the stretching parameter k. Setting $k = 1$ results in no stretching.

Active Region Number	No. of Loops N_{loops}	Stretching Parameter k	Misalignment Angle $\bar{\alpha} \pm \sigma_\alpha$	Base Field Strength $\bar{B} \pm \sigma_B$ (G)
10953	200	0.5	$26.1° \pm 8.6°$	232 ± 316
		1.0	$25.4° \pm 9.0°$	196 ± 235
		2.0	$33.5° \pm 12.7°$	182 ± 217
10955	70	0.5	$19.7° \pm 5.0°$	211 ± 156
		1.0	$19.4° \pm 6.4°$	166 ± 109
		2.0	$26.3° \pm 6.6°$	160 ± 104
10956	100	0.5	$38.8° \pm 14.7°$	196 ± 171
		1.0	$36.4° \pm 13.7°$	158 ± 117
		2.0	$38.3° \pm 13.6°$	150 ± 104

and therefore a large departure from force free conditions, which is not expected for active regions with strong magnetic fields. A more versatile transformation, with increased spatial dependence, could show promise in improving the model field's approximation of the real field's structure.

Progress has been made toward the development of a parameterized technique that can be used to transform model magnetic fields to match the coronal field structure as observed in the EUV and in X-rays (Gary, 2001a, 2003). Relying on the *frozen flux theorem* (see Appendix A), the Parametric Transformation Analysis (PTA) method assumes a field embedded in a medium so that as the medium is deformed, so, too, are the field lines. The resulting field may be non-potential, and even non-force-free in certain regions, a quality that may prove effective in dealing with the transition between the non-force-free photosphere and force-free corona.

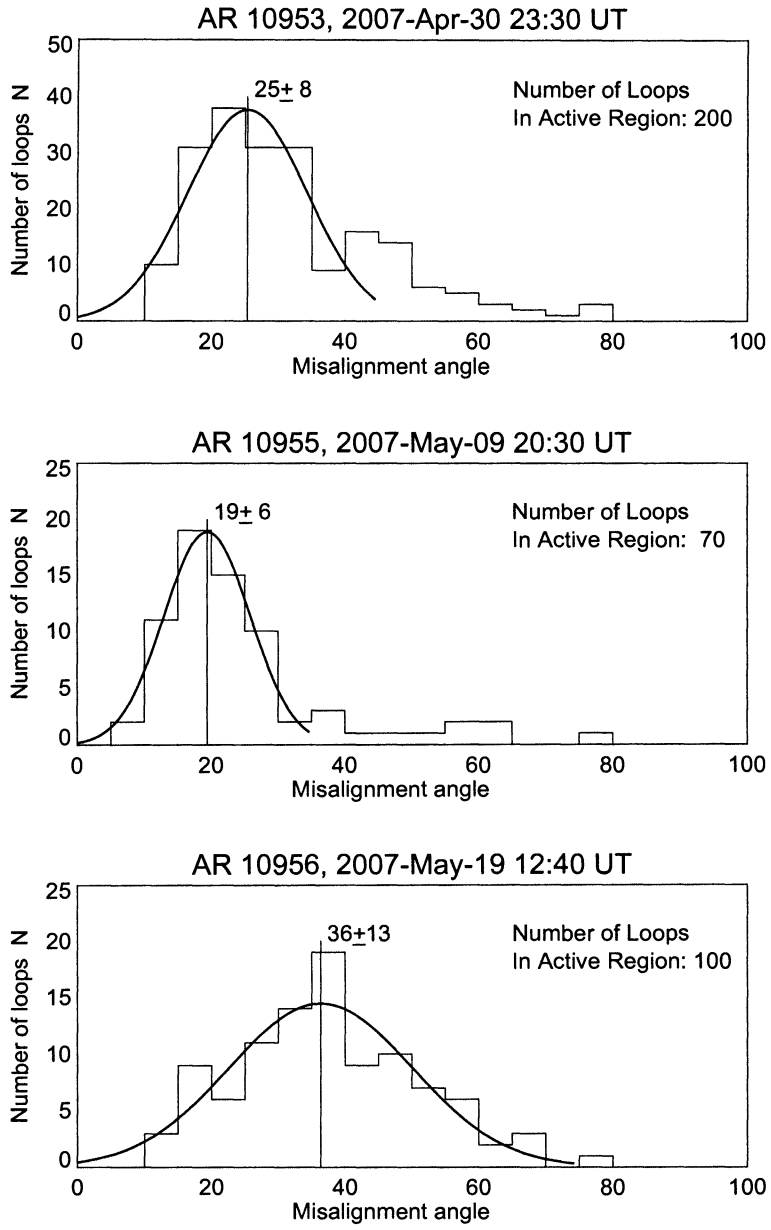

Figure 3.12: Median misalignment angles for the three active regions studied. The x-axis indicates the median loop misalignment angle α; the y-axis indicates the number of loops in the active region that have a given median misalignment angle. A Gaussian curve is fitted to the peak of each distribution, and the average and standard deviation are noted at the peak of each curve. Mavericks with $\alpha > 2\alpha_{max}$ are excluded from the Gaussian fit.

3.6 Summary and Discussion

In this study we have performed a side-by-side analysis of three solar active regions: we have examined the relationship between their magnetic field configurations and potential field extrapolations of those active regions. We used knowledge of the 3D coronal magnetic field structure in these active regions, derived from STEREO/EUVI observations in multiple channels, as observational tests of potential field extrapolations based on line-of-sight photospheric magnetograms from SOHO/MDI. These field extrapolations consisted of unmodified PFSS fields as well as PFSS fields transformed with a radial stretching that was implemented following the form given by Gary & Alexander (1999). In order to test these model fields, we developed routines to compare the 3D structure of the real coronal field as observed by STEREO/EUVI with its model counterpart using the angle between local loop tangent and magnetic field vectors. The overall average misalignment angle for an active region serves as a quantitative measure of how well the model field approximates the true field structure.

The PFSS model is widely used in the study of coronal magnetic fields (see, for example, Schrijver et al., 2005; Wang & Sheeley, 2003; Morgan & Habbal, 2010), and this comparison provides a valuable contribution to our understanding of the viability of the model for simulating active region magnetic fields. This is the first time we have had access to truly stereoscopic observations of the solar corona, and therefore the first time that we have been able to compare any magnetic field model to the true 3D structure of the coronal magnetic field. These data facilitate a more

thorough assessment of the PFSS model's ability to reproduce observed coronal field morphology than was previously possible.

This work also supplies a valuable baseline for other comparisons of the field structure of these active regions and other types of model fields (such as force-free fields). In particular, AR 10956 has been the subject of numerous studies due to its flare and partial filament eruption (Li et al., 2008; Bone et al., 2009; Liewer et al., 2009). Because the Sun was exceptionally inactive during the period when the STEREO satellites were optimally positioned for stereoscopy, AR 10956 is one of the only active regions that STEREO observed exhibiting energetic phenomena, and therefore is likely to continue to be used in future research. The ability to establish the misalignment between a model field and the observed field morphology may prove useful in subsequent study of this active region (see Chapter 4).

Although the model field for each active region displays a substantial misalignment with the observed field morphology, the variation in the median misalignment angles for different active regions yields some insight into the extent to which the real coronal field departs from potentiality (i.e. it provides an indication of the *non-potentiality*). The relative non-potentiality among the different active regions may indicate a relationship between the misalignment angle and the free energy provided by currents in the active region. This possible connection is evident in the heightened misalignment (non-potentiality) of AR 10956, which experienced a flare and partial filament eruption.

In general, the use of EUV observations may impact these findings in the selection for certain types of loops. In some cases, the emission from "moss," low-lying, spongy material that appears bright in EUV wavelengths (Berger et al., 1999; Fletcher & De Pontieu, 1999; Kittinaradorn et al., 2009), can hinder the accurate tracing of loops. The tracing process is also inherently biased toward larger loops, rather than the smaller ones that may lie near a neutral line. It is easier to trace shorter, more central loops in 284 Å images than in 171 Å or 195 Å images, which may imply that some short loops near the neutral line are outside EUVI's temperature range. As a result, the majority of the traceable loops lie outside the core of each active region. Schmieder et al. (1996) and Aulanier et al. (1998) have found that observed loops tend toward potentiality with increasing distance from an active region's neutral line and that loops with the highest degree of shear are found in the active region's core. Thus, because there exists a bias toward large-scale loops, highly sheared short or low-lying loops may be underrepresented. These results may therefore overestimate the degree of potentiality of the active regions.

Such an overestimation could help explain the unexpectedly high misalignments found by DeRosa et al. (2009), who tested several non-linear force-free field (NLFFF) models of AR 10953. DeRosa et al. compared their NLFFFs with the same 3D observed field structure used here, and calculated misalignments equal to or greater than the value found here for AR 10953 ($\alpha = 25°$). NLFFFs have generally been thought to be the most promising avenue for analytical modeling of active region

magnetic fields (Démoulin et al., 1997), so this finding came as a surprise. Further discussion of this result and its relationship with the evaluation of potential field models can be found in DeRosa et al. (2009) and in Chapter 4 of this thesis.

At present it is not possible to determine whether the difference in connectivity between the observed loops and model field lines is due to a particular type of non-potentiality (*e.g.* twist or shear). In each active region, one can observe loops that are perpendicular to the neutral lines, implying a low degree of shear. However, because the loops observable with EUVI may overestimate an active region's potentiality, conclusions about the nature of these active regions' non-potentiality may be premature. Inspection of *Hinode* XRT data show that the hotter, low-lying loops in the core of the active region, which is not well covered by the traced EUVI loops used here, do not exhibit strong shear, either. It is possible that future studies (see Chapter 6) will more adequately address this question.

One potential improvement is the application of a more sophisticated transformation to the model field to introduce a variety of both radial (force-free) and azimuthal currents and a degree of non-potentiality for comparison with observations. The use of a simple radial stretching did not appreciably lower the misalignment between the model field and the observed field configuration, but a different formulation may give improved results. An additional topic of interest would be the application of these field transformations to alternative model fields, such as NLFFFs.

Perhaps the most significant difficulty lies in the discrepancy between the two ob-

servational constraints: magnetograms taken in the non-force-free photosphere and images of the (presumably force-free) active region corona. The use of magnetogram data taken above the chromosphere would be an ideal way to resolve this ambiguity, but such data is unavailable at the present time. In the absence of large-scale observations of the magnetic field in a force-free environment, the misalignment angles calculated here may help guide the creation and refinement of improved modeling techniques. It may be possible, for example, to use knowledge of the coronal field's structure to adjust the photospheric magnetograms such that they more accurately reflect the field at the base of the corona, thereby avoiding the difficulty of the transition region between the photosphere and corona, or even to eschew the lower boundary condition altogether. The latter approach is discussed in more detail in Chapter 4.

Chapter 4

A New Method for Modeling the Coronal Magnetic Field with STEREO and Submerged Dipoles

4.1 Introduction

Our physical understanding of the solar atmosphere depends critically on quantitative modeling of the magnetic field, without which we cannot fully infer the geometry of coronal structure. The corona has been the subject of extensive modeling for decades, but these efforts have been hampered by our limited ability to determine the corona's three-dimensional (3D) structure. Until recently, our observations of the corona have remained strictly two-dimensional. Because the corona is optically

thin, this restriction results in images containing essentially no information regarding the geometry along the line of sight. With the 2006 launch of the *Solar Terrestrial Relations Observatory* (STEREO, Howard et al., 2008), at last we have the ability to observe the Sun in three dimensions (Aschwanden & Wülser, 2010). STEREO's two satellites, carrying identical suites of instruments, observe the Sun from two perspectives.

Armed with more complete observational constraints, some have studied the accuracy of models at reproducing the three-dimensional structure of the coronal magnetic field (see, for example, Feng et al., 2007; Li et al., 2008). In Chapter 3 of this thesis, a study of three active regions modeled with Potential Field Source Surface (PFSS) magnetic fields showed misalignments of approximately $20 - 40°$ between the model and observed field structures. DeRosa et al. (2009) modeled one of the three active regions with several different non-linear force-free field (NLFFF) models, using observations from *Hinode*'s Solar Optical Telescope (SOT) in a restricted field of view. In a very surprising result, they achieved misalignments that were no better than the misalignments for potential models of that region. Both studies demonstrate a need not only for improved models of the coronal magnetic field, but specifically for improved models that account for the sharp transition from the lower boundary condition—typically a magnetic field surface distribution measured in the non-force-free solar photosphere (Metcalf et al., 1995)—to the simulation domain, the force-free corona.

As part of the research leading to this thesis, we have developed a new magnetic

modeling method that sidesteps the problem of the non-force-free lower boundary condition. Using images from STEREO's Extreme Ultraviolet Imagers (EUVI, Wülser et al., 2004) as the primary observational constraints, we model the coronal magnetic field with a series of magnetic dipoles submerged below the solar surface (the photosphere). This method creates a model field without requiring the photospheric or magnetic input that is thought to compromise traditional magnetic modeling methods. With the resulting models, we obtain misalignments between the model and observed field structure that are significantly smaller than those found for PFSS fields and NLFFFs.

Models of the coronal field are typically based first on photospheric magnetic input, and subsequently compared with coronal observations. The method used here proceeds in reverse: the model field is constrained only by the structure of the coronal field as observed by EUVI, and the associated "photospheric" field may vary freely. A comparison between this model photospheric field and observed photospheric fields could shed light on changes that the field experiences between the photosphere and low corona, such as the reorganization of currents from a regime in which they may flow across the field to one in which they may flow only parallel to the field (Metcalf et al., 1995). Although EUVI observations cannot constrain the magnetic field strength in the model field, the model satisfies the physical requirement that the field be divergence-free. It does not, however, consider other physical aspects, e.g. the presence of field-aligned currents that contribute to free energy in the corona.

Despite this caveat, the success of the dipole model in simulating the observed field configuration of the four active regions studied (see results in Section 4.5) renders it a useful tool for studying active region magnetic fields.

This model uses an array of magnetic dipoles positioned below the photosphere to create model fields that are forward-fitted to the three-dimensional coordinates of coronal loops identified in EUVI image pairs. In an environment where the plasma beta is generally small, $\beta < 1$ (Gary, 2001b), the field inhibits plasma motion across the field, forcing EUV-emitting plasma to flow along the field. Thus, since the magnetic field vector at a point in space describes the direction of the field at that point, one can consider the coronal loop vectors (vectors that lie tangent to the observed loops) as a dimensionless equivalent of the actual field. One restriction of EUV observations, however, is that the identifiable loops are typically long loops (up to 345 Mm in length) positioned toward the periphery of the active regions, which may lead them to be more potential than shorter loops near the core of the active regions (Schmieder et al., 1996; Aulanier et al., 1998).

The dipole model yields misalignment angles similar to those found in a study performed by Aschwanden & Sandman (2010), in which systems of unipolar magnetic charges were optimized to fit the observed coronal loops. The unipolar charge method makes use of a photospheric magnetogram to guide the placement of the unipolar charges based on the observed distribution of magnetic flux: magnetic charges are clustered below the simulated solar surface in regions that display higher magnetic

field. This distribution provides an initial guess to an optimization routine that adjusts the positions and relative strengths of the charges based on the 3D field configuration observed by STEREO/EUVI.

The dipole modeling method used here requires no magnetogram input in order to configure the model field, and achieves comparable results using fewer parameters. As in the unipolar charge model, the dipole model explicitly optimizes the model field based on the misalignment angle between observed and model structures. This practice necessarily results from the uniqueness of the STEREO/EUVI data, and the lack of alternative indicators of the field's 3D geometry. Thus, the dipole method constitutes an empirical model rather than an independent test.

Section 4.2 introduces the theoretical magnetic field used, and a method of comparing the model field's morphology with that of the observed loop structures. The data and processing methods used to prepare the stereoscopic constraints for the models are described in detail in the previous chapter in Section 3.4 and Aschwanden & Sandman (2010), and reviewed here in Section 4.3. In Section 4.4 we describe the process of the forward-fitting. we discuss the results of the modeling and possible selection biases in Section 4.5, followed by conclusions in Section 4.6.

4.2 Theory

4.2.1 Dipolar Magnetic Fields

The use of magnetic dipoles facilitates a straightforward modeling of the coronal magnetic field: the magnetic field due to a dipole is defined analytically, and the number of independent parameters required to model even several dipoles does not impose a significant computational burden. Submerged dipoles can also be modeled without recourse to any magnetic input whatsoever. This property eliminates the fundamental conflict that undermines many magnetic models of the corona, in which a non-force-free boundary condition is used and extrapolated to a simulation domain that is presumed to be force-free. Although photospheric magnetograms are valuable observational constraints, the way in which they are currently incorporated into models has been shown to be problematic. Dipole fields, which are potential and therefore automatically divergence- and force-free, provide consistency throughout the domain, though they may not adequately describe the non-force-free photospheric field. This difference may nevertheless lead to insight into the chromospheric field: when the dipole field accurately models the observed coronal field geometry, the difference between the model field and observed field at the photosphere provides a connection among the photospheric, chromospheric, and coronal fields.

Naturally, many active region configurations will not be well described by the field of a single dipole. The divergence- and force-free nature of dipole fields persists when two dipoles fields are combined, so it is possible to construct a model field

using multiple superimposed dipole fields. This arrangement is akin to assuming a distribution of monopoles (see earlier discussion), but is more physical. The linear property of the divergence, $\nabla\cdot(\mathbf{B}_1+\mathbf{B}_2)=\nabla\cdot\mathbf{B}_1+\nabla\cdot\mathbf{B}_2$, permits the combination of several dipoles in arbitrary order without violating the requirement that the resulting field be divergence-free ($\nabla\cdot\mathbf{B}=0$). This model assumes a current loop of infinitesimal size with the far-field approximation of a magnetic dipole (Jackson, 1999, presented in further detail in Appendix E):

$$\mathbf{B}(\mathbf{r})=\frac{\mu_0}{4\pi}\left[\frac{3\mathbf{n}(\mathbf{n}\cdot\mathbf{m})-\mathbf{m}}{|\mathbf{r}-\mathbf{r}_0|^3}\right] \tag{4.1}$$

where $\mathbf{r}=(x,y,z)$ is the position vector at which the field is calculated, and $\mathbf{r}_0$ the position of the dipole, (x_0,y_0,z_0):

$$\mathbf{r}-\mathbf{r}_0=(x-x_0)\,\hat{\mathbf{x}}+(y-y_0)\,\hat{\mathbf{y}}+(z-z0)\,\hat{\mathbf{z}} \tag{4.2}$$

The normal vector between the two points is defined as $\mathbf{n}=(\mathbf{r}-\mathbf{r}_0)/|\mathbf{r}-\mathbf{r}_0|$. The magnetic moment, $\mathbf{m}$, of the current loop (dipole) can be written in components, which are functions of the inclination angle, θ, within the $x-y$ plane, and the azimuth angle ϕ within that plane:

$$m_x = m\cos\theta\cos\phi \tag{4.3}$$

$$m_y = m\cos\theta\sin\phi \tag{4.4}$$

$$m_z = m \sin\theta \tag{4.5}$$

The summation of several individual dipoles yields a more complicated magnetic field:

$$\mathbf{B} = \sum_{i=1}^{n} \mathbf{B}_i(\mathbf{r}_i) = \sum_{i=1}^{n} \frac{\mu_0}{4\pi} \left[\frac{3\hat{\mathbf{r}}_i (\hat{\mathbf{r}}_i \cdot \mathbf{m}_i) - \mathbf{m}_i}{|\mathbf{r}_i|^3} \right] \tag{4.6}$$

where n is the number of dipoles in the system.

4.2.2 Field Misalignment

To evaluate the success of the model field ($\mathbf{B}_{dip}(\mathbf{r})$) in reproducing the structure of the observed field ($\mathbf{B}_{obs}(\mathbf{r})$), a dimensionless equivalent, $\mathbf{b}_{obs}$, may be used as a proxy for the real magnetic field,

$$\mathbf{b}_{obs}(s) = \frac{\mathbf{B}_{obs}(s)}{|\mathbf{B}_{obs}(s)|} \tag{4.7}$$

where s is the coordinate along a given observed loop. The scalar product of $\mathbf{b}_{obs}$ at a given position $\mathbf{r}$ with the coincident dipole field unit vector, $\mathbf{b}_{dip}(\mathbf{r}) = \mathbf{B}_{dip}(\mathbf{r}) / |\mathbf{B}_{dip}(\mathbf{r})|$, gives the angle α between the two vectors:

$$\alpha = \cos^{-1}(\mathbf{b}_{dip} \cdot \mathbf{b}_{obs}) \tag{4.8}$$

This *misalignment angle*, α, serves as a quantitative measure of the goodness-of-fit of the model (dipole) field to the observed loop structure, i.e. to the real field

structure at that point on the loop. The misalignment angle allows an assessment of the forward fitting for the active region as a whole, for all points along all loops in the active region: $\alpha = \langle \alpha_i \rangle$ for $i = 1, \ldots, n$. The number of points per individual loop depends on the overall length of the loop, and ranges from 18 to 137 points per loop (see Table 4.1). When tracing the loops, the user typically selects by hand four or five points that define the overall shape of the loop (see section 4.3.2). The remaining points are interpolated via a spline fit.

It should be noted that α may vary within a range of $0° < \alpha < 90°$. This restriction removes the inherent 180° ambiguity[1] of the magnetic field's direction (α or $180° - \alpha$), which cannot be constrained by STEREO data. The definition of a single value also warrants well behaved convergence in the forward fitting code. In the absence of this simplification, the code would have two ambiguous convergence behaviors in parallel and anti-parallel field directions.

4.3 Observations

4.3.1 Data Set

This study examines four active regions observed by STEREO/EUVI in 2007: active region (AR) 10953 (30 April), AR 10955 (9 May), AR 10956 (19 May), and AR 10978 (11 December), all of which are the subject of previous and ongoing studies.

[1]This ambiguity results from the fact that parallel and antiparallel field directions are observationally indistinguishable from each other, and therefore can be treated as identical.

Table 4.1. Observational data for four active regions observed by STEREO/EUVI.

Active Region	Observation Date	Observation Times (UT)	Spacecraft Separation Angle	Number of Loops	Points per Loop
10953	2007 Apr. 30	23:00-23:20	6.0°	200	18 - 137
10955	2007 May 9	20:30-20:50	7.1°	70	26 - 95
10956	2007 May 19	12:40-13:00	8.6°	100	26 - 112
10978	2007 Dec. 11	16:30-16:50	42.7°	87	26 - 70

A summary of the data sets can be found in Table 4.1. The first three active regions were analyzed in Chapter 3 in the context of PFSS modeling. The first active region, AR 10953, has also been analyzed by DeRosa et al. (2009) using *Hinode* and STEREO data, and with NLFFF models. The second, AR 10955, has been studied extensively by Aschwanden et al. (2008b,c, 2009), examining the active region's 3D structure, temperature and density measurements, and stereoscopic tomographic reconstruction. The third active region, AR 10956, exhibited a flare and a partial filament eruption (Li et al., 2008; Bone et al., 2009; Liewer et al., 2009; Conlon & Gallagher, 2010). Finally, AR 10978 is the subject of ongoing NLFFF modeling efforts (Aad Van Ballegooijen and Alec Engell, private communication, 2010). All four active regions were also modeled in Aschwanden & Sandman (2010).

4.3.2 Stereoscopy

The forward-fitting scheme used here relies on the knowledge of the three-dimensional topology of coronal loops in order to make the best possible assessment of the mag-

netic models. This information is derived from sets of EUVI image pairs in three wavelengths (171 Å, 195 Å, and 284 Å) using a stereoscopic triangulation tool discussed in Aschwanden et al. (2008c), Chapter 3, and Appendix D. To account for the different roll angles of the spacecraft, the images must be co-aligned such that the solar equator is parallel to the epipolar plane, defined by the positions of the two spacecraft and Sun center (Inhester, 2006), for accurate stereoscopic triangulation.

In some cases, low signal-to-noise ratios and the bright EUV emission from low-lying, patchy material known as "moss" (Berger et al., 1999; Fletcher & De Pontieu, 1999; Kittinaradorn et al., 2009) can make it difficult to trace overlying loops accurately. Moss is particularly prevalent in the core of active regions, and interferes with the identification of loops in active region interiors, such as loops in the 284 Å channel and other loops that overlie the center of the active region. While it is not possible to eliminate the moss from the images, the signal-to-noise ratio can be increased by summing images taken over a brief period of time. A summation over a maximum elapsed time of 20 minutes provides improved signal-to-noise without introducing blur due to feature motion or solar rotation. Depending on the instrument cadence in the different wavelengths, 2 - 8 images per wavelength are summed for each active region (see Table 4.1), which facilitates more accurate and more consistent loop tracing. A high-pass filter is also applied to the images in order to improve feature definition (see Appendix C).

After the completion of the image pre-processing, coronal loops are identified by

eye and traced by hand. Automated loop tracing codes are still unable to extract complete loop structures in noisy image areas (Aschwanden et al., 2008a), although automated algorithms are nearing visual perception for high-resolution images ($\lesssim 1''$, Aschwanden, 2010). The loop tracing code outputs a set of Cartesian coordinates describing the collection of loops in a given active region. These coordinates can then be imported into the forward-fitting code for comparison with the model magnetic field. The coordinates are calculated in the STEREO-A reference frame, i.e. with the origin located at the center of the solar disk as seen by the STEREO-A spacecraft.

4.4 Forward Fitting

In this section we summarize the steps taken to fit a system of n dipoles to the three-dimensional field structure represented by observed coronal loops. The observational constraints on the field are simply the three-dimensional coordinates of loops obtained via stereoscopy from EUVI images (Section 4.3.2). We fit the dipoles in a cumulative way, starting with one dipole and incorporating additional dipoles one by one.

For each active region, stereoscopic triangulation provides the coordinates of a set of coronal loops in EUVI images (see Section 4.3.2). Based on these coordinates, we define a three-dimensional domain in the Cartesian coordinate system, whose $x-$ and $y-$boundaries are defined by the range of $x-$ and $y-$coordinates of the observed loops. The $x-y$ plane lies tangent to the solar surface at the center of the

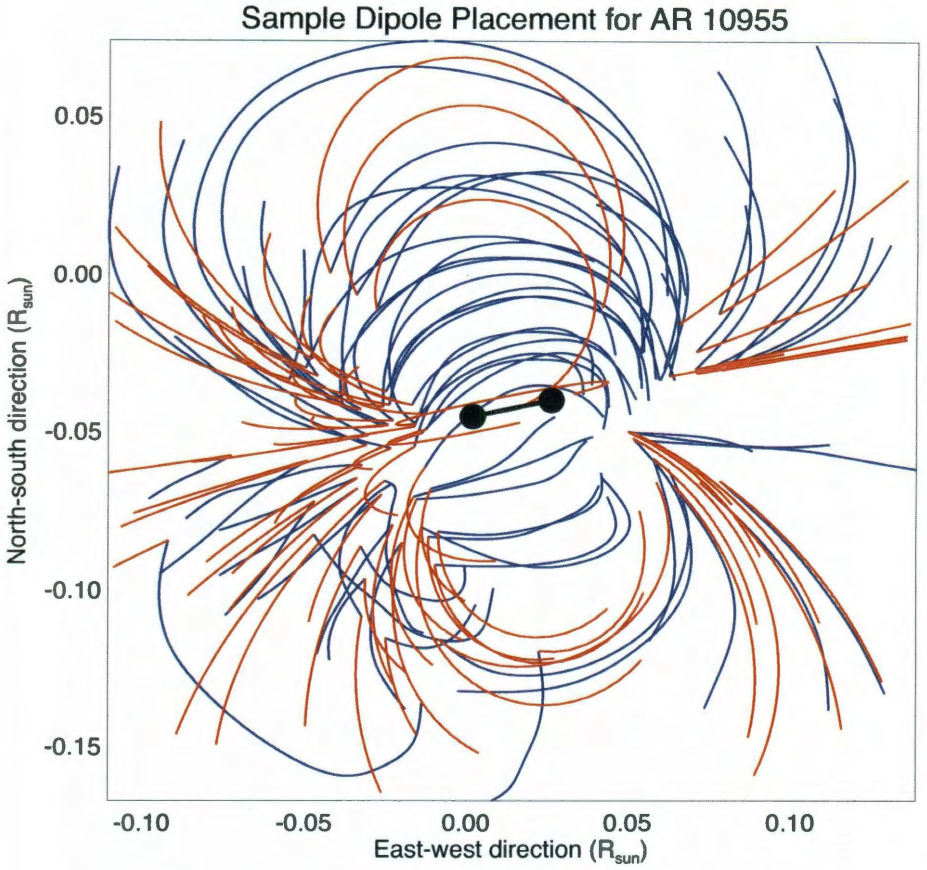

Figure 4.1: EUVI loops (blue) and dipole model field lines (red) for AR 10955 (9 May 2007), using a sample initial dipole placement. The dipole's position and orientation are indicated by the black filled circles.

active region, and the extent of the domain in the $z-$direction is determined by the loops' maximum $z-$coordinate, approximately one density scale height (50-90 Mm, Aschwanden et al., 2000). The rapidly decreasing plasma density and resulting low signal-to-noise ratio above one scale height typically prohibits the identification of distinct linear structures at higher altitudes.

The initial guess for the fitting is formulated manually, based on the overall appearance of the active region and the morphology of the observed loops (see Figure

4.1). The initial guess consists of six parameters that describe a dipole: position in x, y, and z; inclination angle θ about the $y-$axis (parallel to the plane that at the center of the active region is tangent to the solar surface, and oriented in the north-south direction); and azimuth angle ϕ about the $z-$axis (perpendicular to the plane tangent to solar surface). The magnitude of the first dipole is normalized to unity; in the absence of observed magnetic field strengths, this model field is dimensionless. Thus, the first guess has only five coefficients (x, y, z, θ, ϕ); for additional dipoles, which have six coefficients, the magnitude m is normalized with respect to the first dipole, as optimized by the code. This optimization is achieved using the Powell method (Press et al., 1986), which is efficient and stable for first-order optimizations of the type presented here, and generally converges well for appropriate initial guess values. It is not clear if an alternative optimization method would more reliably achieve a global minimum; a study of the effectiveness of different optimization techniques for this problem would be a interesting topic of future work.

After optimizing the first dipole, additional dipoles are iteratively added and optimized, until the median misalignment angle converges to the lowest value that the code can "find." In each iteration of the Powell routine, the code calculates the median overall misalignment angle (Section 4.2.2) between the observed loop vectors and the coincident magnetic field vectors. These field vectors are determined analytically according to equation 4.6, using the set of dipole coefficients for that iteration. The code steps through the parameter space for each of the coefficients until it arrives

Table 4.2. Active region misalignment results for the NLFFF, PFSS, unipolar charge, and dipole models.

Parameters	2007 Apr. 30 23:00 UT	2007 May 9 20:30 UT	2007 May 19 12:40 UT	2007 Dec. 11 16:30 UT
α_{NLFFF}	$24° - 44°$	...	...	...
α_{PFSS}	$25° \pm 8°$	$19° \pm 6°$	$36° \pm 16°$	$32° \pm 10°$
α_{uni}	$14.3° \pm 11.5°$	$13.3° \pm 9.3°$	$20.3° \pm 16.5°$	$15.2° \pm 12.3°$
α_{dip}	$16.3° \pm 14.4°$	$11.1° \pm 6.9°$	$17.8° \pm 11.1°$	$11.2° \pm 11.2°$

at a minimum value for the misalignment angle. The $z-$coordinate of the dipole is restricted to values below the solar surface ($z < 0$). Because the parameter space has as many as $\sim$ 30 free parameters (for 5 dipoles), it is not guaranteed that the optimization algorithm converges to the absolute minimum. We therefore try multiple different initial guesses for each dipole to ensure a global convergence.

4.5 Results

4.5.1 Active Region Misalignments

We fit each active region with magnetic fields consisting of up to 5 dipoles; additional dipoles do not improve the misalignment angle. Based on the optimized dipole configurations for each active region, we find misalignments of $16° \pm 14°$ for AR 10953 (30 April 2007), $11° \pm 7°$ for AR 10955 (9 May 2007), $18° \pm 11°$ for AR 10956 (19 May 2007), and $11° \pm 11°$ for AR 10978 (11 December 2007).

The best-fit results of the dipole fitting are shown in Figures 4.2 - 4.5. The field lines for the dipole model are shown as red lines and the coronal loop structures obtained by stereoscopy from EUVI image pairs are shown as blue lines. Underlying the field lines and loops in each figure is a map of the STEREO-constrained $z-$component of the model magnetic field, $B_{dip,z}$, at the level of the photosphere. For ease of comparison, the field lines and loops have the same initial footpoints (that is, they originate at the same location). In most cases, the model field lines display morphology that is comparable to that of the observed loop structures, although the connectivity of the field lines is typically different from that of the loops. The variation in the connectivity reflects the degree of misalignment for an individual loop: loops that are well represented by the model field will have coincident field lines that diverge only slightly from the path of the loop, whereas loops that are poorly represented will have coincident field lines that travel in a very different direction.

For each active region, we calculate the misalignment angle at all points on the observed loops for which we have coordinate information. These misalignment angles are collected in a histogram for every active region; the four histograms are shown in Figure 4.6. Each histogram is fitted with a Gaussian distribution; the peak of the curve indicates the most frequent misalignment value (i.e. the misalignment angle for which the histogram has its maximum value) and the standard deviation for the active region, $\alpha \pm \sigma$. The most frequent misalignment angles and their standard deviations are listed for each active region in Table 4.2. For comparison, Table 4.2

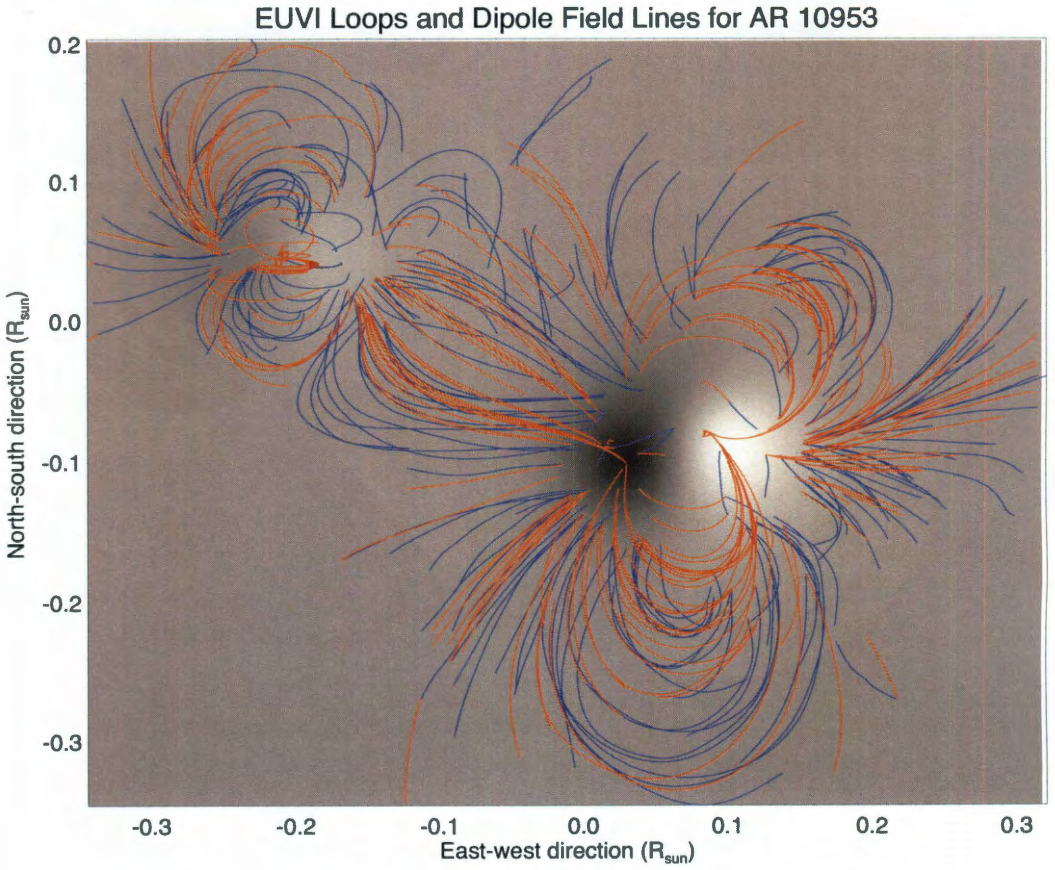

Figure 4.2: EUVI loops (blue) and best-fit dipole model field lines (red) for AR 10953 (30 April 2007). The loops and field lines are plotted over a map of the model magnetic field at the level of the photosphere.

also shows the misalignment angles found for the NLFFF (AR 10953 only, DeRosa et al., 2009), PFSS (see Chapter 3), and unipolar charge methods (Aschwanden & Sandman, 2010). Also shown in Figure 4.6 are plots of the misalignment angle for models using different numbers of dipoles ($1 \leq N_{dip} \leq 5$), demonstrating the gradual reduction in misalignment angle that achieved by using multiple dipoles. Presented for reference is the misalignment angle found for the PFSS model in each case (dashed

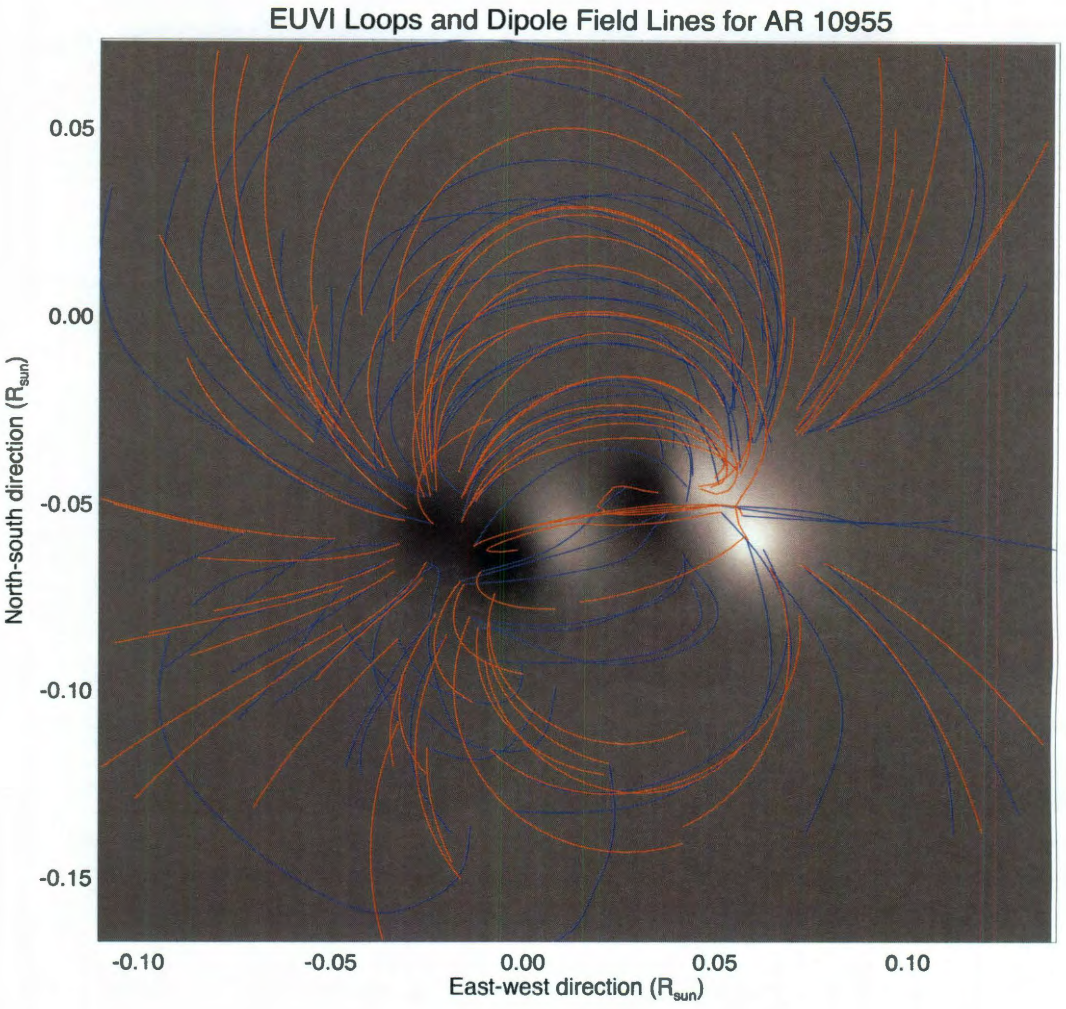

Figure 4.3: EUVI loops (blue) and best-fit dipole model field lines (red) for AR 10955 (9 May 2007). Representation is similar to Figure 4.2.

horizontal line).

The dipole model provides a reduction in misalignment angle of $\Delta\alpha_{NLFFF} = 8°$ over the best NLFFF results for AR 10953. Because the *Hinode*/SOT vector magnetograms used by DeRosa et al. (2009) are limited in their extent (approximately $328'' \times 164''$, Kosugi et al., 2007), they do not encompass the entire active region.

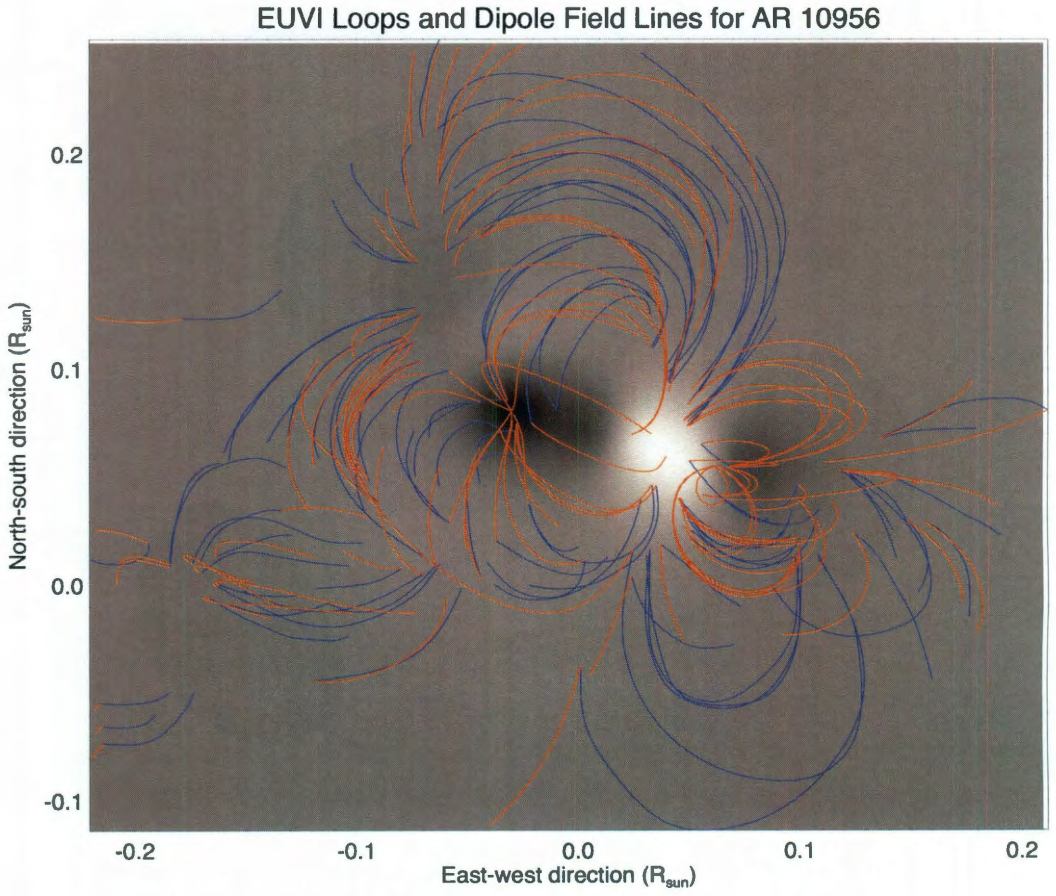

Figure 4.4: EUVI loops (blue) and best-fit dipole model field lines (red) for AR 10956 (19 May 2007). Representation is similar to Figure 4.2.

DeRosa et al. therefore embed the observed vector magnetogram within a line-of-sight magnetogram obtained from the Michelson Doppler Imager (MDI) on the *Solar and Heliospheric Observatory* (SOHO) mission, which provides vertical (or near-vertical) field information but no horizontal field information. Thus, they have the most complete observations for the core of the active region, where one would expect the field to be most non-potential (Schmieder et al., 1996; Aulanier et al., 1998). The bias of

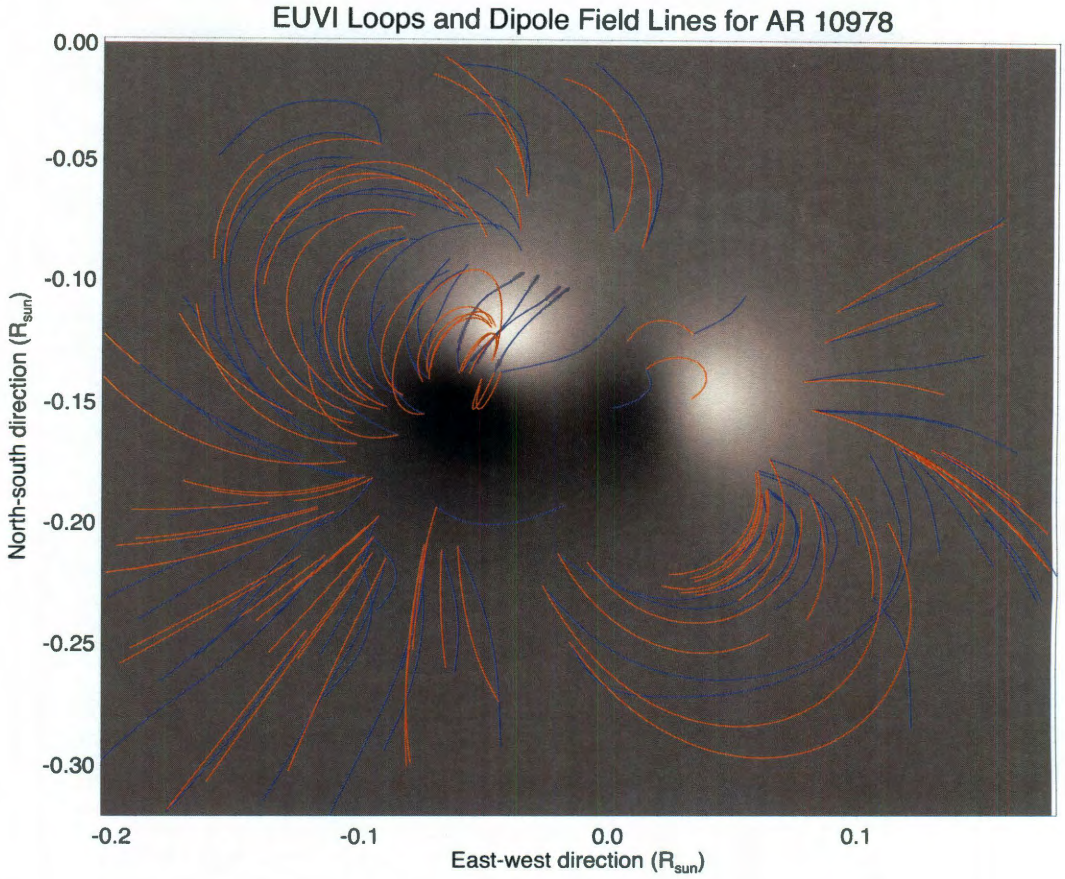

Figure 4.5: EUVI loops (blue) and best-fit dipole model field lines (red) for AR 10978 (11 December 2007). Representation is similar to Figure 4.2.

EUV coronal observations toward loops in the outer areas of the active region, rather than low-lying loops near the neutral line, implies a limited suitability for testing NLFFF modeling methods *per se*, which may explain the overall high misalignments found by DeRosa et al..

The range of dipole model misalignment angles for the four active regions ($\alpha_{dip} \approx 11° - 18°$) shows a substantial decrease in misalignment when compared with PFSS

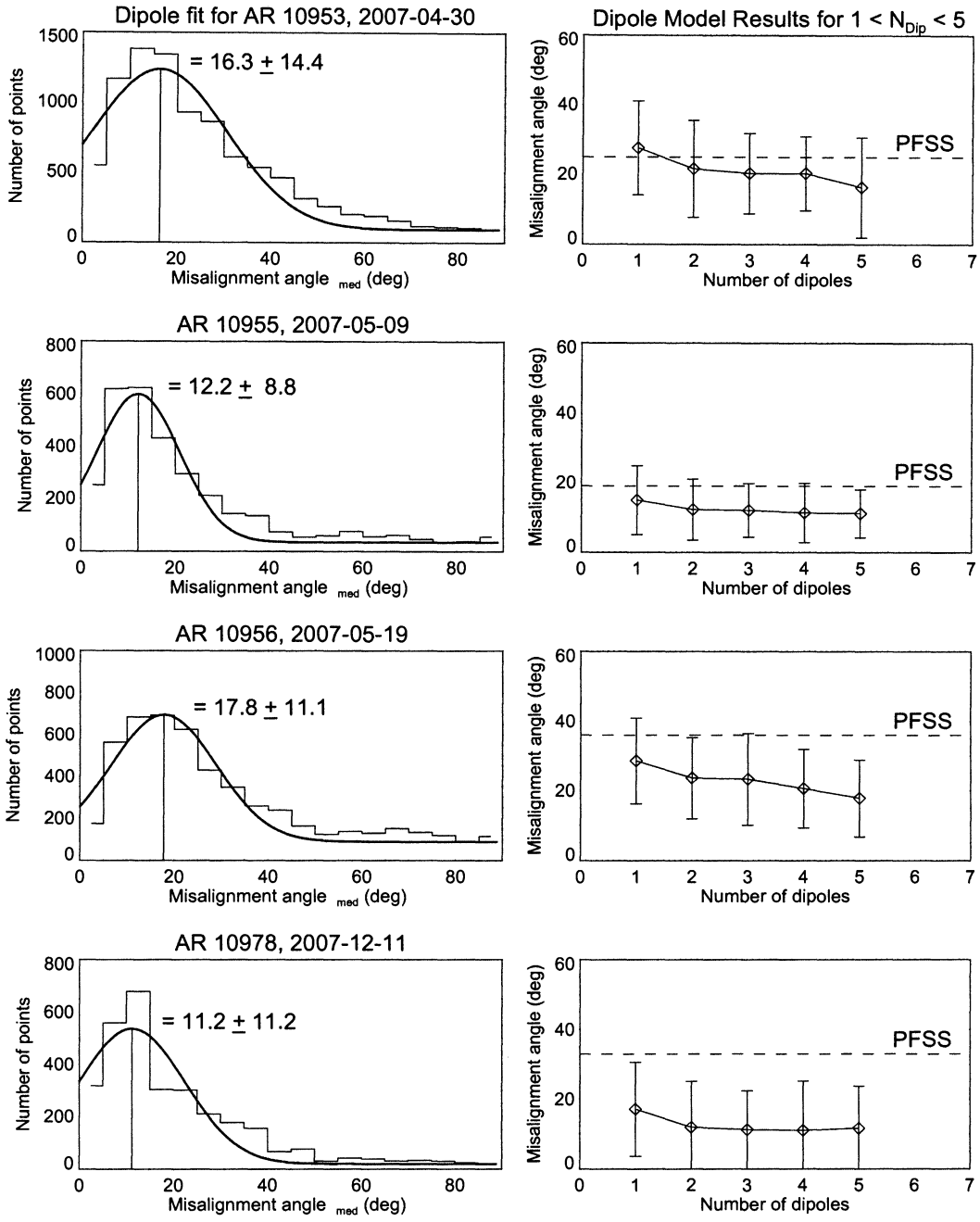

Figure 4.6: Left column: histograms showing the distribution of misalignment angles in each active region studied. The histograms are fitted with a Gaussian distribution, and the peak shows the characteristic misalignment angle for that active region. Right column: active region misalignment angles as a function of the number of dipoles used in the model. For comparison, the dashed horizontal line shows the misalignment value found for the PFSS model.

models of the same regions ($\alpha_{PFSS} \approx 19° - 36°$): $\Delta\alpha_{PFSS} = 8° - 21°$ depending on the active region. A reduction in misalignment implies that the model field more closely resembles the real coronal field. This closer agreement with observations makes the dipole model a useful tool for analyzing the physical properties of active region magnetic fields, as will be demonstrated in Chapter 5.

The dipole model also yields misalignment angles that are comparable to those of the unipolar charge model described by Aschwanden & Sandman (2010). The most frequent misalignment angles are $\langle\alpha_{uni}\rangle \approx 16° \pm 3°$ for the unipolar model and $\langle\alpha_{dip}\rangle \approx 14° \pm 3°$ for the dipole model. This result suggests that the small-scale field does not have a significant impact on the overall loop structure on a scale observable with STEREO/EUVI. The small-scale field and loops with $L \lesssim 10$ Mm can therefore be neglected for the purposes of forward fitting the model parameters to STEREO data. The loops traced in EUVI images have lengths in the range 18 Mm $< L <$ 345 Mm.

4.5.2 Temporal and Spatial Variation in Misalignment

The overall misalignment angle of an active region provides a useful measure of the goodness-of-fit of a given magnetic field model to the observed coronal field's structure in that active region, but it may be that a single value is too simplistic as a descriptor of an entire active region. Particularly in the case of active regions exhibiting a complex field structure, such as AR 10956, there may be areas of the

region that are better or more poorly described by the model field than the active region as a whole. It is therefore worthwhile to examine the active region locally as well as globally.

In each active region, We identify small groups of loops with dipolar configuration and calculate the misalignment angles for each individual group. These collections of misalignment angles provide a better picture of the spatial distribution of the misalignment angles in the active region, and therefore a better idea of how well the model field fits the observed field in different areas of the active region. The segmentation of active regions into individual groups of loops shows, for some regions, a broad distribution of misalignment angles throughout a given active region. The range in median misalignment angles from one area of an active region to another is as small as 7° for AR 10978 and as large as 25° for AR 10956, a difference of up to 75% compared with the median misalignment of the overall active region. For AR 10956, the area with the highest median misalignment angle (region 4 in Figures 4.7 and 4.8) is also the area associated with flaring activity.

This result is not surprising in light of the active region's activity level and complex structure. Indeed, the fact that it experienced a flare and partial filament eruption motivates a study of the active region's misalignment angles as a function not only of space, but also of time. We choose one set of EUVI images before the increase in soft X-ray flux observed by GOES (12:10-12:30 UT, Figure 4.7), and a second set after the soft X-ray curve returns to pre-flare levels (15:40-16:00 UT, Figure 4.8). With

these image sets we trace all identifiable coronal loops (see Section 4.3.2), and thus acquire two sets of 3D loop coordinates describing the coronal field before and after the flare. The representation in both figures is similar to Figures 4.2-4.5: the blue lines show the observed loop structures traced in STEREO/EUVI images, and the red lines show the field lines traced through the model magnetic field. The structures are plotted over a map of the model magnetic field at the level of the photosphere. We divide the active region into four groups of morphologically similar loops, indicated by numbered black boxes. For each group, the distribution of misalignment angles is calculated and fitted with a Gaussian. The misalignment angles for the four loop groups are shown as histograms below the main panels of Figures 4.7 and 4.8 (middle panels), along with the overall distribution of misalignment angles (lowest panel).

After constructing dipole magnetic fields for both the pre-flare and post-flare loops, we find that, surprisingly, the two sets of loops display comparable misalignment angles (histograms at bottom center of Figures 4.7 and 4.8). The dipole models for the pre- and post-flare loops find different optimum dipole configurations, as demonstrated by the different connectivity of the model field lines (red lines) between Figures 4.7 and 4.8, but the lowest misalignment angles achieved by the forward fitting are similar for the two periods of time. Thus, the loops show considerably more variation in misalignment angles within a given active region than they do between the two snapshots in time.

One might expect that the flare and eruption would trigger a release of magnetic

energy and a subsequent relaxation of the field into a more potential state. Based on soft X-ray images from *Yohkoh* before and after a flare of GOES class M4.4, Sakurai et al. (1992) observed the evolution of the field from a sigmoidal configuration (i.e. highly sheared) to a more relaxed configuration. However, we do not observe such an evolution here. The area from which the filament erupted (region 4 in Figures 4.7 and 4.8) experienced only a slight decrease in median misalignment angle over the course of the eruption: from 42° to 36°.

This small change indicates that for a minor flare such as the one observed here (GOES class B9) and an incomplete filament eruption, the decrease in magnetic energy might be adequate to affect only a slight change in a localized region, without a discernible change in the overall active region and with persistent non-potentiality. Alternatively, the dipole model could be equally poor at reproducing both field configurations, so that any relaxation toward a more potential state is undetected by the model's best-fit attempt at reproducing the observed field structure. An additional possibility is that in the case of the post-flare loops, the code simply does not converge to a solution with the lowest possible misalignment. Further studies of other active regions exhibiting flares or eruptions would be helpful in elucidating this result, and in Chapter 5, we examine the evolution of coronal loops following two large flares. However, because the Sun was particularly inactive for the majority of the period when the STEREO spacecraft were favorably positioned for stereoscopy, it has not been possible to perform a stereoscopic analysis of a larger flare.

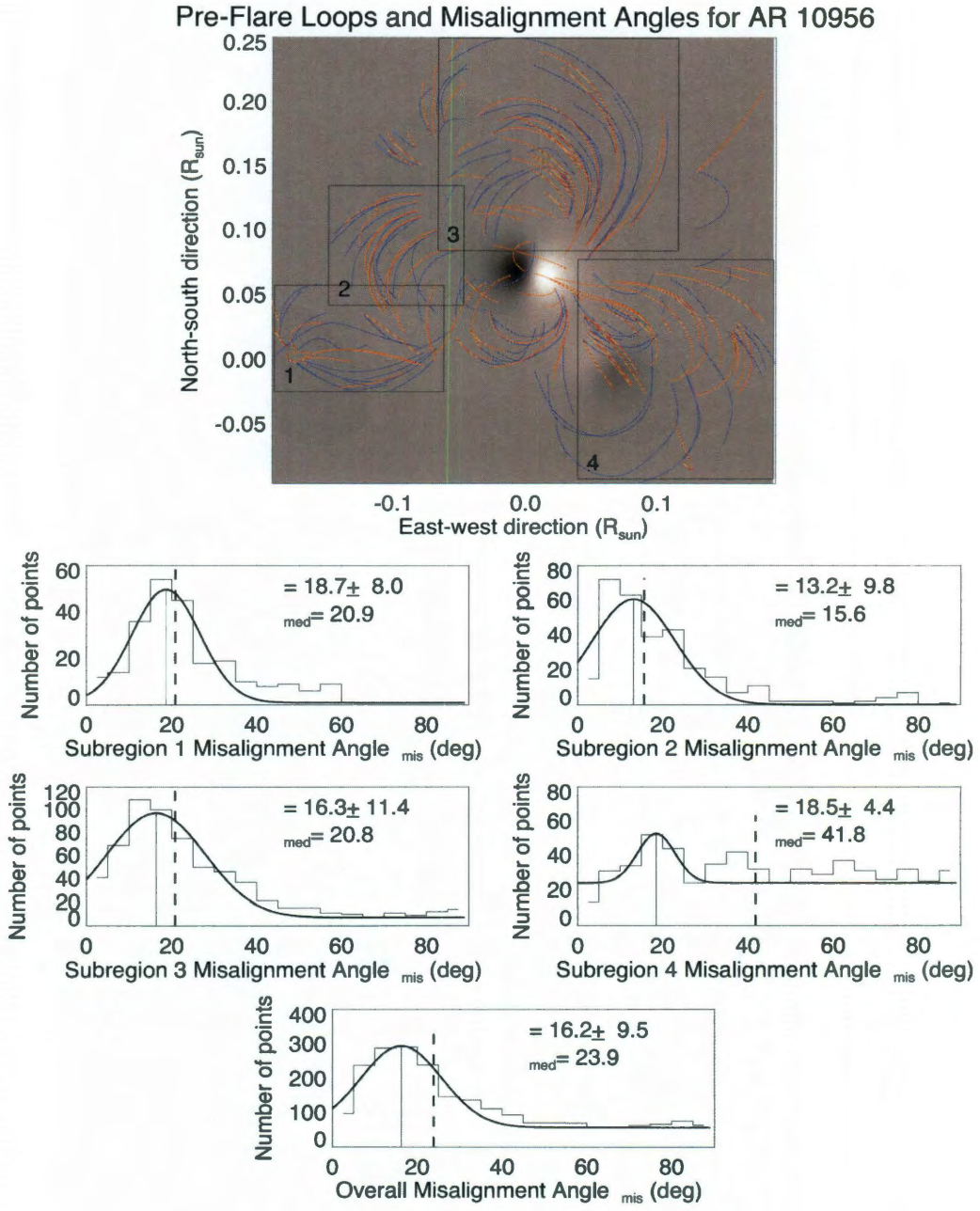

Figure 4.7: Top panel: EUVI loops traced for AR 10956 (19 May 2007) at 12:10 UT, before a B-class flare and partial filament eruption. The boxed regions indicate areas for which the misalignment was calculated independent of the overall misalignment. Lower panels: misalignment angle distributions for the boxed regions, and for the overall active region.

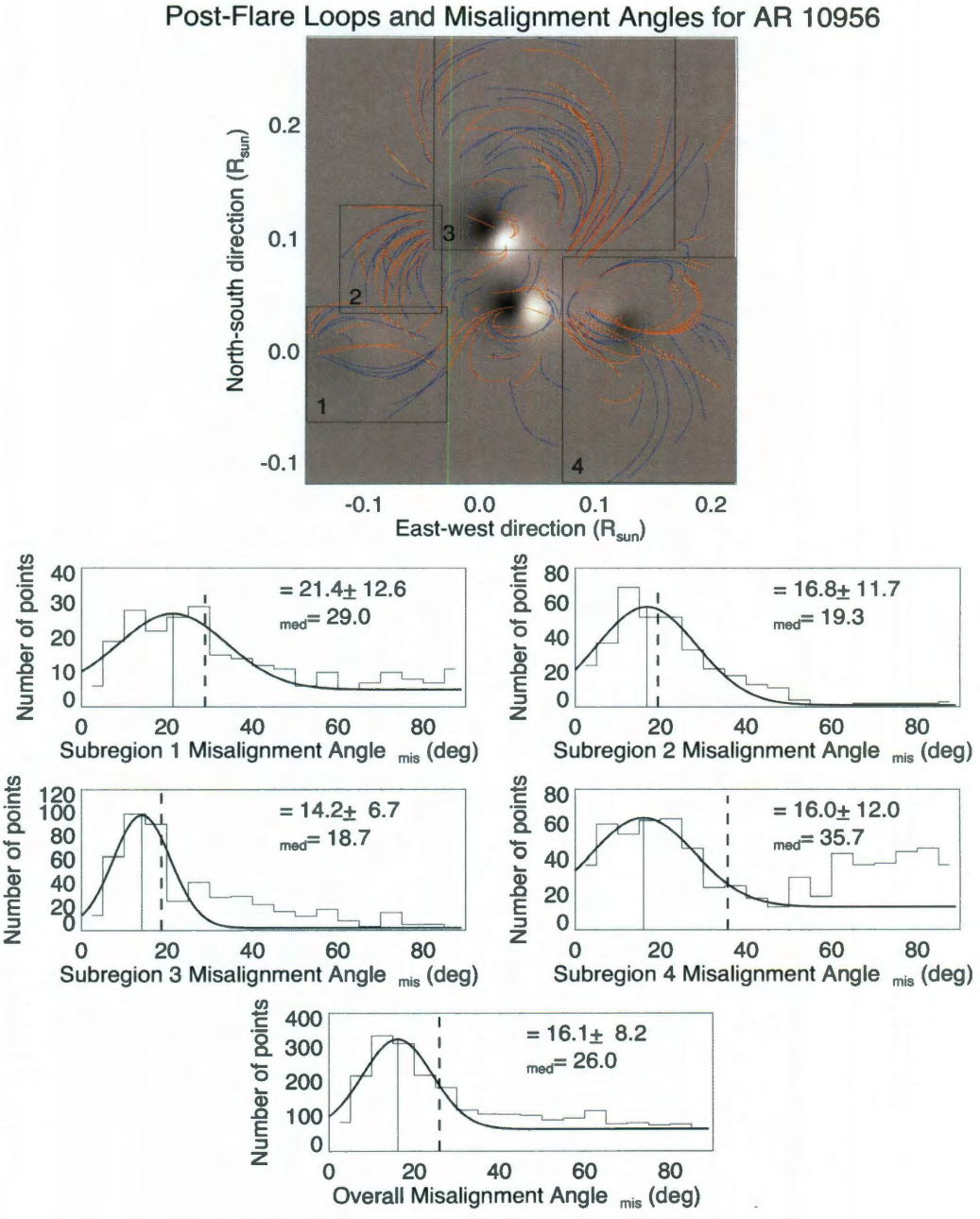

Figure 4.8: Similar representation as Figure 4.7, but for images taken at 15:40 UT, after the GOES soft X-ray curve had returned to pre-flare levels.

Table 4.3. Stereoscopic errors calculated for different magnetic field models.

Field Type	AR 10953	AR 10955	AR 10956	AR 10978
PFSS Model	8.8°	6.1°	9.0°	8.1°
Unipolar Charge Model	9.4°	7.6°	11.5°	8.9°
Dipole Model	9.6°	8.4°	10.4°	8.3°
Mean, α_{SE}	$9.3° \pm 0.4°$	$7.4° \pm 1.7°$	$10.3° \pm 1.3°$	$8.4° \pm 0.4°$
Non-Potentiality, α_{NP}	$13.2° \pm 17.8°$	$7.3° \pm 10.6°$	$11.5° \pm 11.7°$	$7.5° \pm 16.7°$

4.5.3 Stereoscopic Error and Active Region Non-Potentiality

In order to distinguish the different factors that contribute to the overall misalignment angle, it is helpful to quantify the errors associated with the process of tracing the loops in EUVI images. The stereoscopic errors fall into three categories: (1) it is impossible to distinguish unique reference points on loops that lie along or at a small angle to the east-west direction; (2) depending on the angle between the two STEREO spacecraft, the spatial resolution of the instrument may be insufficient to resolve the parallax angle[2]; (3) there are errors due to misidentification of loops in one or both images. These inaccuracies can be due to incorrect connectivity when tracing a loop in one image, or the identification of a completely separate loop in image B, for example, as the counterpart to one already traced in image A.

Aschwanden & Sandman (2010) devised a method of estimating the stereoscopic errors based on the assumption that the three-dimensional structure of the field varies

[2]Because the angle between the STEREO spacecraft increases with time, the resolution of the parallax angle only contributes to the stereoscopic error for images taken during the early months of the STEREO mission.

smoothly, with field vector orientations ranging from near-parallel in close proximity to progressively larger angles with increasing distance. This assumption holds for both the model field, which varies smoothly, and for the real coronal field, which the EUV observations show us is also smoothly varying. By extension, given that coronal loops are assumed to represent the magnetic field, the loop structures traced in STEREO/EUVI images would, if perfectly traced, have the same orientation from one loop to the loop immediately adjacent. The misalignment angles between the model field structure and the observed field structure are expected to display the same consistency over short distances. Conversely, over large distances it is expected that the misalignment angles are not as likely to be consistent.

The stereoscopic error in the traced loop coordinates can be expressed as a function of the difference in misalignment angles from one loop to the next, $\alpha_i - \alpha_j$. The change in misalignment angles is weighted according to the distance ρ_{ij} between two loop positions. An expression for the stereoscopic error, α_{SE}, that takes into account this weighting can be formulated as:

$$\alpha_{SE} = \frac{\sum_{i,j} |\alpha_i - \alpha_j| w_{ij}}{\sum_{i,j} w_{ij}} \tag{4.9}$$

where the index i spans all positions of each loop, and the index j spans all points of other loops. Points distant from each other are expected to have very different misalignment angles, so the weighting factor w_{ij} scales with some power p of the

distance ρ_{ij} between the two points,

$$w_{ij} = \frac{1}{\rho_{ij}^{p}} = \left[(x_i - x_j)^2 + (y_i - y_j)^2 + (z_i - z_j)^2\right]^{-p/2} \tag{4.10}$$

where $p \approx 12$ was found to provide an adequate weighting (Aschwanden & Sandman, 2010). equation 4.9 is evaluated for each active region, and the results collected in Table 4.3. The stereoscopic errors for the PFSS and unipolar charge models are included, and the errors for the three models are used to determine the error mean and standard deviation for each active region.

The true misalignment angle can be defined as the difference between a potential field model and the non-potential real field, α_{NP}. Assuming that the stereoscopic errors (α_{SE}) and the misalignment due to the real field's non-potentiality (α_{NP}) can be added in quadrature to form the observed misalignment angle for the dipole field, $\alpha_{dip}^2 = \alpha_{SE}^2 + \alpha_{NP}^2$, the non-potentiality is written as follows:

$$\alpha_{NP} = \left(\alpha_{dip}^2 - \alpha_{SE}^2\right)^{1/2} \tag{4.11}$$

Evaluating this expression for each active region (for misalignment angle values given in Table 4.2) yields the following values: for AR 10953 (30 April 2007), $\alpha_{NP} = 13° \pm 18°$; for AR 10955 (9 May 2007), $\alpha_{NP} = 7° \pm 11°$; for AR 10956 (19 May, 2007), $\alpha_{NP} = 12° \pm 12°$; and for AR 10978 (11 December, 2007), $\alpha_{NP} = 8° \pm 17°$. We calculate the error propagation using the standard deviation for the distribution of

Table 4.4. Approximation of the force-free parameter λ based on the non-potentiality and observed loop lengths for each active region.

Active Region	Non-Potentiality $\alpha_{NP} \pm \sigma_{NP}$	Loop Lengths L (Mm)	Force-Free Parameter λ (10^{-3} Mm^{-1})
AR 10953	$13.2° \pm 17.8°$	$17.9 - 345.3$	$0.7 - 13.1$
AR 10955	$7.3° \pm 10.6°$	$25.7 - 233.7$	$0.6 - 5.0$
AR 10956	$11.5° \pm 11.7°$	$28.6 - 208.5$	$1.0 - 7.1$
AR 10978	$7.5° \pm 16.7°$	$18.2 - 169.2$	$0.8 - 7.2$

misalignment angles, σ_{dip} (Table 4.2), and the standard deviation for the stereoscopic error, σ_{SE}, which are summarized in Table 4.3.

These estimates of the non-potentiality can be used to investigate the force-free nature of the real coronal field. Relating the misalignment due to non-potentiality α_{NP} to the shear angle θ in a model of a sheared arcade (Priest, 1982), the force-free parameter λ can be written as:

$$\tan \alpha_{NP} \approx \tan \theta = \frac{\lambda}{L} \tag{4.12}$$

where L is the length of the loops. Estimating the non-potentiality from equation 4.11, equation 4.12 gives values of $\lambda \approx (0.6 - 13) \times 10^{-3}$ Mm^{-1} (Table 4.4), which are consistent with other results, e.g., Feng et al. (2007), $\lambda \approx (2 - 8) \times 10^{-3}$ Mm^{-1}.

4.6 Discussion and Conclusions

The surprising results of recent studies (DeRosa et al., 2009, and Chapter 3 of this thesis) have demonstrated a need for a new approach to modeling coronal magnetic fields. The fundamental inconsistency of basing force-free coronal field models on non-force-free boundary conditions yields an inherent constraint on their ability to model the real coronal field. This study utilizes a new magnetic modeling method that circumvents the difficulties of PFSS and NLFFF modeling by relying solely on coronal observations (a dimensionless representation of the coronal field), rather than photospheric magnetograms, to guide the refinement of the model field.

The dipole model uses a system of superimposed submerged dipoles to construct a potential field that is forward-fitted to match the three-dimensional structure of coronal loops stereoscopically triangulated from STEREO/EUVI image pairs. We model four active regions with $3-5$ dipoles (up to ~ 30 free parameters) per active region. The placement and orientation of the dipoles is optimized with the Powell method of minimizing the misalignment angle between the model and the loop structures. The best-fit dipole fields yield active region misalignments of $\alpha_{dip} = 11° - 18°$, which represents a change of $\Delta\alpha_{NLFFF} = 8°$ compared with the most successful NLFFF models of AR 10953, and $\Delta\alpha_{PFSS} = 8° - 21°$ over PFSS models of the four active regions.

These results corroborate those found in Aschwanden & Sandman (2010), in which a unipolar magnetic charge model minimized the mean misalignments to $\alpha_{uni} =$

$13° - 20°$. Although the results from the two models are similar, the dipole model uses fewer free parameters and no observational magnetic input. The unipolar charge model makes use of photospheric magnetograms to guide the placement of its magnetic charges, and this difference may provide further insight into the photospheric and coronal field. The fine structure of the magnetic field map produced by the unipolar charge model is not seen in the map for the dipole model, and yet the two models achieve relatively consistent levels of success in modeling the observed field structure. This result indicates that the field structure on scales of $L \lesssim 10$ Mm does not contribute substantially to the overall structure of the coronal field as observed by STEREO, and thus can be neglected.

In addition to studying the misalignment of the model field and observed field structure over whole active regions, we examine the spatial distribution of misalignment angles within each of the four active regions, as well as temporal changes of the misalignment before and after a flare and partial filament eruption in AR 10956. Although we find heightened misalignments in areas of AR 10956 that are associated with flaring activity, we do not find a significant difference in misalignment angles between the pre- and post-flare states. These results show up to 75% variation in median misalignment angles for different areas within an active region, compared with a change of only $< 40\%$ in a given area over the course of a flare.

Conlon & Gallagher (2010) studied one of the active regions examined here, AR 10956, using a cost function analysis and linear force-free field (LFFF) extrapolations

at several points in time before, during, and after the flare and eruption. They conclude that during the few hours prior to the onset of the flare, there is both flux cancellation in the region and an increase in the twist and free energy in the modeled structures. This build-up phase ends with the initiation of the flare, after which the twist and magnetic energy in the model decrease to levels observed at the beginning of the build-up phase. These findings initially appear to contradict the results presented here; however, the examination performed by Conlon & Gallagher is limited to field lines in an area of the active region that corresponds to region 3 in Figures 4.7 and 4.8. Examination of the dipole model model's misalignment angle distributions in this area shows a decrease in median misalignment: $\alpha_{med} = 21°$ to $\alpha_{med} = 19°$. This change may correspond to a slight decrease in non-potentiality, which would support the reduction in twist and magnetic energy found by Conlon & Gallagher.

Nevertheless, it is not clear that a change in misalignment of $\Delta\alpha_{med} \approx 2°$ in this area is large enough to constitute a definite change in the non-potentiality of the active region as a whole. Schrijver et al. (2005) found that the presence of a filament in or near an active region does not significantly impact the region's non-potentiality, and that it is the currents associated with emerging flux systems that are more indicative of an active region's non-potentiality. It is not clear if this result applies to erupting filaments as well as quiescent filaments, but a similar effect may be at work here. Schrijver et al. also noted that in some cases, the field is non-potential at low altitudes while remaining more potential at larger scales. Because

STEREO/EUVI observes only the large-scale structure of the field, it may be that the use of EUV wavelengths precludes observation of the most non-potential structures, or any significant post-eruption shift toward non-potentiality. Further examination of similar events is needed in order to determine whether or not this result is an anomaly, and if not, to investigate the causes and implications of this behavior.

We have demonstrated that the large-scale morphology of an active region's magnetic field can be represented with a set of submerged dipoles. These dipole magnetic fields yield lower misalignment angles than those achieved by traditional PFSS models, or even with the current state of the art of NLFFF models. We attribute this change in part to the exclusive use of coronal observations in this forward-fitting, in which we ignore the non-force-free lower boundary condition that has been found to hinder other magnetic modeling efforts. With this new modeling technique, it is possible to make more refined estimates of the degree to which non-potentiality contributes to the misalignment angles in an active region, and establish a range of values of the force-free parameter. These estimates appear to be correlated with the localized buildup of currents and magnetic energy in flaring areas of an active region, which may in time help us better understand the conditions that lead to coronal activity.

This analysis of submerged dipole fields motivates further studies of the coronal and photospheric magnetic fields. Because photospheric magnetograms are excluded in this technique, a comparison of STEREO-constrained magnetic field maps with

magnetograms from SOHO/MDI would be of interest for future studies. These findings indicate that the differences between the two maps may shed light on ways in which the magnetic field and electric currents are altered in the transition from from the photosphere to the corona; for example, that a significant portion of the currents close in the photospheric region and do not extend into the corona. These insights could be of use to the NLFFF modeling community as they discuss approaches to dealing with the difficulty of the non-force-free boundary condition.

Chapter 5

Dipole Modeling of Post-Flare Loop Arcades

5.1 Introduction

Analytical models provide an invaluable resource for understanding the coronal magnetic field. In the absence of large-scale measurements of the three-dimensional (3D) field (see discussion in Chapter 2), models supply a means by which we can test our understanding of how the field is distributed throughout the solar atmosphere. Most modeling techniques, however, are hindered by the conflict between assumptions about the nature of the modeled field (i.e. that it is force-free, see below and Appendix B) and the nature of the boundary conditions used. The boundary conditions are necessarily based on photospheric magnetograms, in which the observed field contains currents that run not only parallel, but also perpendicular to the mag-

netic field (Metcalf et al., 1995). The photospheric field contains a non-zero Lorentz force ($F_L = \mathbf{j} \times \mathbf{B}$) and is therefore said to be *non-force-free* (see Appendix B for a summary of magnetic field types). By contrast, the coronal field is believed to contain only field-aligned currents (Schrijver & van Ballegooijen, 2005), i.e. it is *force-free* ($F_L = \mathbf{j} \times \mathbf{B} = 0$). Analytical magnetic modeling techniques do not address the transition between the non-force-free photosphere and the force-free corona (MHD modeling is better suited to dealing with this transition, see Abbett & Fisher, 2003; Abbett, 2007). The resulting discrepancy has contributed to the models' difficulty in accurately representing the real coronal field (DeRosa et al., 2009).

In Chapter 4, we presented a new magnetic modeling approach, developed as part of the research for this thesis, that avoids the inconsistency inherent in a model composed of a non-force-free boundary condition and a force-free simulation domain. The dipole method employs a series of submerged magnetic dipoles placed according to the field structure observed in extreme ultraviolet (EUV) images of the corona, and requires no photospheric magnetic input. For selected active regions, we showed that the dipole model yields a field structure that agrees more closely with the observed field structure than do the commonly used Potential Field Source Surface (PFSS) models or the more sophisticated non-linear force-free field (NLFFF) extrapolations, both of which suffer from the reliance on non-force-free boundaries.

In the course of examining one of the active regions tested, we found that the agreement between the model and observed field structures did not improve appre-

ciably over the course of a minor (GOES B-class[1]) solar flare. Because a flare involves a release of energy, it was expected that analysis of the pre- and post-flare states of the magnetic field would show a relaxation of the field from a stressed (higher energy) configuration to a more potential (lower energy) configuration. We proposed as one possible explanation that the field relaxation for such a small flare is not significant enough to be observable. In this chapter, we investigate two larger flares, one M-class and one X-class. We use the dipole model presented in Chapter 4 to demonstrate that for these events, the coronal loops observed in the aftermath of the flare do experience a relaxation. In both cases, the loops evolve from sheared, high-energy configurations to minimally sheared, more potential configurations, indicating a release of energy from the region over the course of the observing period.

In Section 5.2, we review the criterion used to determine the success of the model field in representing the observed field structure. This section also includes an investigation into the impact of the use of 2D field information, e.g. from projected line-of-sight images from the *Solar Dynamics Observatory* (SDO), compared with the 3D field geometry used in Chapters 3 and 4, where a 3D representation was derived from the two viewpoints afforded by the twin *Solar Terrestrial Relations Observatory* (STEREO) spacecraft. In Section 5.3, we summarize the observational data from which we obtain the constraints for the dipole model. Section 5.4 contains an

[1]Solar flares are classified according to their brightness in soft X-rays (for wavelengths $1 \leq \lambda \leq 8$ Å). The strongest flares are X-class flares, followed in order of descending magnitude by M-class, C-class, B-class, and A-class flares. The classification is based on a logarithmic scale: X-class flares are 10 times brighter than M-class flares, and so on. An X1.0 flare is defined as having X-ray flux of 10^{-4} W m^{-2}, whereas an M1.0 flare is defined as having X-ray flux of 10^{-5} W m^{-2}.

overview of the dipole model, as well as the results of the dipole modeling of the two active regions. In Section 5.5, we present early results of an extension of this effort, in which we use a simple analytical force-free field construction to estimate the change in energy of the different observed field configurations. Finally, Section 5.6 provides a discussion of the results.

5.2 Loop Analysis of Single Images

5.2.1 The Misalignment Angle

In Chapters 3 and 4, we introduced the *misalignment angle* as a means of quantifying the agreement between the observed 3D coronal magnetic field structure and the structure of a model field. Although coronal imaging is unable to constrain the magnitude of the field, the field direction is indicated by bright coronal loops observed in the EUV and in X-rays. For a plasma in which the magnetic field dominates, i.e. the magnetic pressure exceeds the thermal pressure (consequently, the plasma beta is small, $\beta < 1$; see Chapter 1), cross-field diffusion is inhibited, and the plasma is forced to flow along the field. Because the active region corona is considered a low-beta plasma (Gary, 2001b), the structure of coronal loops may be treated as a dimensionless proxy for the real field:

$$\mathbf{b}_{obs}(s) = \frac{\mathbf{B}_{obs}(s)}{|\mathbf{B}_{obs}(s)|} \tag{5.1}$$

where s is the coordinate along an observed loop. At any point in space, $\mathbf{r}$, one can also calculate the dimensionless unit vector associated with the model magnetic field:

$$\mathbf{b}_{model}(\mathbf{r}) = \frac{\mathbf{B}_{model}(\mathbf{r})}{|\mathbf{B}_{model}(\mathbf{r})|} \tag{5.2}$$

Evaluating both vectors at a given point on an observed loop, it is straightforward to use the scalar product to find the angle α between the two vectors:

$$\alpha = \cos^{-1}(\mathbf{b}_{model} \cdot \mathbf{b}_{obs}) \tag{5.3}$$

This quantity provides a measure of the success of the model in reproducing the observed structure of the real magnetic field at that point. By calculating α over all points on all loops in an active region, it is possible to evaluate the success of the model for the active region as a whole. Because the images used to determine the field geometry contain no information regarding the magnitude or sign of the field, α varies within the range $0° < \alpha < 90°$ in order to account for the 180° ambiguity in the sign of the field.

5.2.2 Misalignment Angles in Two Dimensions

In the case of the active regions studied in Chapters 3 and 4, the misalignment angle calculated according to equation 5.3 represented the full 3D misalignment between the model and observed field structures. This calculation was made possible

by the fact that the 3D geometry of the real field (with a degree of accuracy given by the stereoscopic error, see Section 4.5.3) could be derived from pairs of nearly simultaneous images of the corona. These images were taken by the Extreme Ultraviolet Imager instruments (EUVI, Wülser et al., 2004) on board the twin *Solar Terrestrial Relations Observatory* spacecraft (STEREO, Howard et al., 2008), which orbit the Sun in a way that leads to a continuously increasing separation angle between the spacecraft ($d\theta/dt \approx 45°$ per year, see Section 3.3). Because stereoscopy is best performed when the angle between the two observatories is relatively small ($\theta \lesssim 30°$, Aschwanden et al., 2008d), only the first year of the STEREO mission yielded images appropriate for stereoscopy.

Unfortunately, during the first year of STEREO operations, not only was the Sun in the part of its 11-year cycle known as *solar minimum* (a period of decreased solar activity, compared with the period of increased activity known as *solar maximum*), it was experiencing an unusually inactive and prolonged solar minimum (de Toma et al., 2010). As a result, STEREO observed only a handful of active regions that were suitable for stereoscopy, none of which produced a large flare. Thus, in order to study the evolution of an active region's magnetic field after a sizable flare, it is necessary to rely on observations from other satellites, such the *Transition Region and Coronal Explorer* (TRACE) and the *Solar Dynamics Observatory* (SDO), which provide only a single view of the Sun in any particular wavelength at any time.

The restriction of coronal observations to single images, rather than pairs of im-

ages taken from different vantage points, limits the resulting field information to two dimensions. Because the corona is optically thin (which is to say that photons traveling through the corona experience negligible scattering or absorption), each individual image is a projection of all coronal emission along the line of sight. For images taken from a single vantage point, then, it is impossible to extract information about the height of a given structure in the solar atmosphere. One can nevertheless obtain the 2D structure of the field as projected onto the solar surface, and using that projected structure calculate a 2D analogue to the full 3D misalignment angle. In the 2D case, the misalignment angle, α, is calculated as in equation 5.3, but the two vectors $\mathbf{b}_{model}$ and $\mathbf{b}_{obs}$ are composed of only the components that lie in the image plane:

$$\mathbf{b}_{model} = (b_{model,x})\hat{\mathbf{x}} + (b_{model,y})\hat{\mathbf{y}}, \tag{5.4}$$

$$\mathbf{b}_{obs} = (b_{obs,x})\hat{\mathbf{x}} + (b_{obs,y})\hat{\mathbf{y}}, \tag{5.5}$$

for $\hat{\mathbf{x}}$ and $\hat{\mathbf{y}}$ the unit vectors in the $x-$ and $y-$directions, respectively.

In preparation for evaluating the success of a model field in the 2D case, it is prudent to investigate the degree to which the 2D misalignment angle under- or overestimates the true 3D misalignment angle. Using the four active regions presented in Chapters 3 and 4, we recalculate the misalignment angles using only the loop coordinates as traced in the images from the Ahead spacecraft (STEREO-A), which give the projected field structure in the image plane. We calculated the misalignment angles for the dipole model of each active region, using the same dipole configuration

in both the 2D and 3D cases. These values are given in Table 5.1. The table includes the 2D and 3D misalignment angles for five different dipole models of each active region, for a number of dipoles $1 \leq N \leq 5$. The ratio of the 3D misalignment angle to the 2D misalignment angle ($\xi = \alpha_{3D}/\alpha_{2D}$) is also given. This ratio ranges from 0.95 to 2.10, depending on the active region and model configuration, but has an average and standard deviation of $\bar{\xi} = 1.44 \pm 0.24$.

This result is consistent with what is expected via a statistical argument: if we measure α_{2D} in the x-y plane and in the x-z plane, the 3D misalignment angle is simply:

$$\sin \alpha_{3D} = \sqrt{2} \sin \alpha_{2D} \approx 1.41 \sin \alpha_{2D} \tag{5.6}$$

Thus, the misalignment angle as calculated from the 2D projection of coronal loop structures generally *underestimates* the true 3D misalignment angle by 44±24%. This calculation will provide a guide for evaluating the significance of misalignment found in comparisons between 2D observed field structures and magnetic field models.

5.3 Observations

In this study, we examine two large solar flares, each of which was observed by a different spacecraft. The flare of 14 July 2000, also known as the Bastille Day Event after the French national holiday with which it coincided, was observed in the EUV by the TRACE satellite. The flare originated in active region (AR) 9077. Based on observations by the *Geostationary Operational Environmental Satellite* (GOES), the

Table 5.1. Misalignment angles calculated for the dipole models of four active regions. The dipole model is composed of N dipoles, $1 \leq N \leq 5$. The misalignment angles are calculated for the 2D case, α_{2D}, and the 3D case, α_{3D}. Also shown is the ratio of the two values, $\rho = \alpha_{3D}/\alpha_{2D}$. The dipoles' positions are initially determined manually, then refined by minimizing the misalignment angle α using the Powell method.

Number of Dipoles	AR 10953			AR 10955			AR 10956			AR 10978		
	α_{2D}	α_{3D}	ξ	α_{2D}	α_{3D}	ξ	α_{2D}	α_{3D}	ξ	α_{2D}	α_{3D}	ξ
1	28.7°	33.8°	1.18	11.4°	18.0°	1.58	28.5°	35.7°	1.25	13.6°	18.7°	1.38
2	19.9°	28.8°	1.42	16.9°	16.1°	0.95	19.6°	29.5°	1.51	10.9°	16.3°	1.50
3	15.9°	26.7°	1.68	12.3°	15.4°	1.25	19.8°	28.6°	1.44	10.9°	14.8°	1.36
4	12.6°	26.5°	2.10	11.9°	15.1°	1.27	18.8°	24.6°	1.31	9.2°	14.0°	1.52
5	11.9°	20.8°	1.75	10.8°	15.0°	1.39	15.2°	23.5°	1.55	9.1°	13.6°	1.49

maximum soft X-ray flux (1-8 Å) associated with the flare was 5.788×10^{-4} W m^{-2}, observed at 10:23 UT (see Figure 5.3). This peak flux value designates the 14 July flare class as X5.7. The second flare considered occurred on 7 August 2010 in AR 11093 and was observed in the EUV (among other wavelengths) by the *Atmospheric Imaging Assembly* (AIA), one of the suites of instruments on board SDO. This flare was associated with a peak soft X-ray flux of 1.0×10^{-5} W m^{-2} as measured by GOES at 18:25 UT, classifying it as M1.0. The details of the observations and data processing are given below.

5.3.1 TRACE Observations

TRACE observed the 14 July 2000 flare in 3 EUV channels: 171 Å, 195 Å, and 284 Å (see Table 5.2). It recorded images with spatial resolution of 1 arcsec and temporal cadence as low as 1 second (Handy et al., 1999). Because of its magnitude and the fact that it was observed by so many instruments, the 14 July 2001 flare has been studied extensively (see, for example, Aulanier et al., 2000; Somov et al., 2002; Yan & Huang, 2003). Aschwanden & Alexander (2001) analyzed the thermal evolution of the post-flare coronal loops, and as part of their analysis traced coronal loops in images of the active region at five different times: 10:11, 10:28, 10:37, 10:40, and 10:59 UT (see Table 5.4 and Figure 5.3). It is these traced loop structures that we use in our study of the flare here. The five images were subjected to a high-pass filter to enhance visible spatial structure (see Figure 5.1) and facilitate the identification

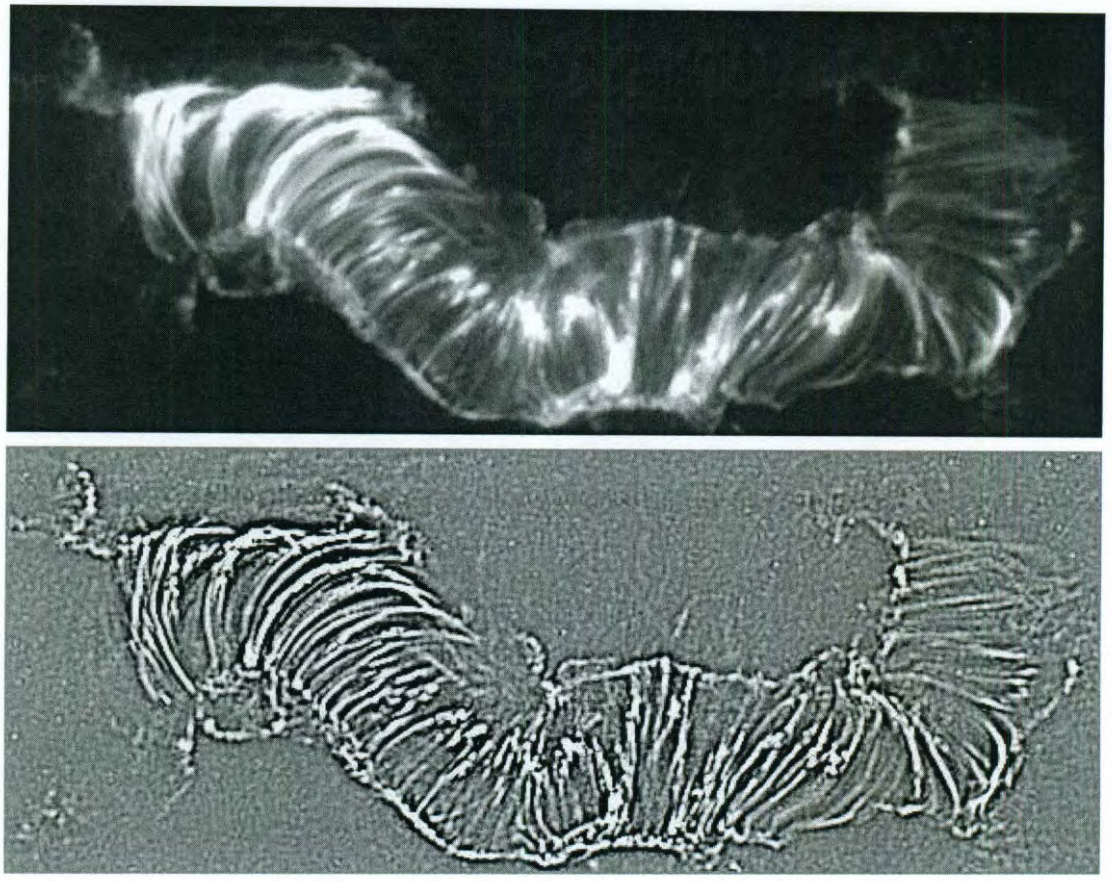

Figure 5.1: Post-flare coronal loops observed by TRACE in 171 Å at 10:59 UT on 14 July 2000. Top: unprocessed image. Bottom: image after a high-pass filter was applied to enhance feature definition.

of as many loops as possible. Aschwanden & Alexander (2001) traced between 3 and 106 loops at each point in time. A TRACE image of the loops in the 171 Å channel is shown in Figure 5.1, unprocessed and after being subjected to a high-pass filter (top and bottom panels, respectively). The traced loop structures can be seen in Figures 5.4 and 5.5.

Table 5.2. EUV wavelengths and corresponding emission lines observed by the *Transition Region and Coronal Explorer* (TRACE) (adapted from Handy et al., 1999).

Wavelength	Emission Line(s)	Temperature of Emitting Plasma
171 Å	Fe IX/X	$1.6 - 20 \times 10^5$ K
195 Å	Fe XII and XXIV	1.2×10^6 K and 2.0×10^7 K
284 Å	Fe XV	$1.25 - 4.0 \times 10^6$ K

5.3.2 AIA Observations

The 7 August 2010 flare was recorded by AIA in all eight of its channels, six of which are suitable for tracing coronal loops: 94 Å, 131 Å, 171 Å, 193 Å, 211 Å, and 335 Å. The spectral lines and plasma temperatures associated with emission at these wavelengths are given in Table 5.3. AIA observes the full solar disk (images span 2.6 solar radii), with 1 arcsec spatial resolution and temporal cadence of 10 seconds. We choose five regularly spaced times at which coronal loops were visible in the AIA images: 18:40, 18:50, 19:00, 19:10, and 19:20 UT (Table 5.4 and Figure 5.3). The AIA image of the post-flare loops in the 171 Å is shown, unprocessed and high-pass-filtered, in Figure 5.2. As in Aschwanden & Alexander (2001), we apply a high-pass filter to the images in order to enhance feature definition for loop tracing (see Figure 5.2). We trace between 79 and 126 loops at each of the times, using images from the six channels listed in Table 5.3. The loop structures traced for this event are shown in Figure 5.9.

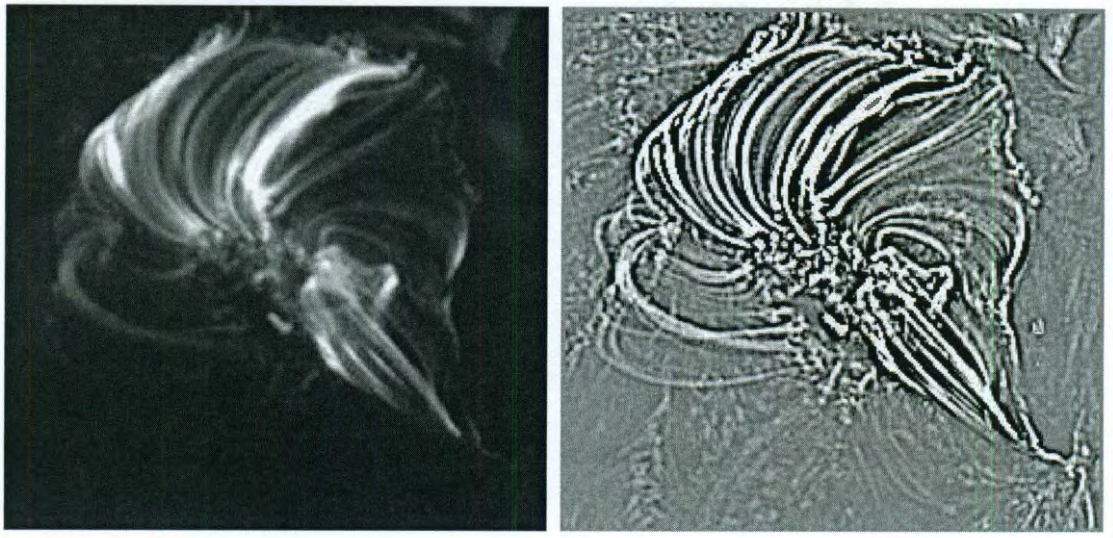

Figure 5.2: Post-flare coronal loops observed by AIA in 171 Å at 19:20 UT on 7 August 2010. Left: unprocessed image. Right: image after a high-pass filter was applied to enhance feature definition.

Table 5.3. EUV wavelengths and corresponding emission lines observed by the Atmospheric Imaging Assembly (AIA) on board the *Solar Dynamics Observatory* (adapted from Soufli et al., 2005).

Wavelength	Emission Line(s)	Temperature of Emitting Plasma
94 Å	Fe XVIII	6.3×10^6 K
131 Å	Fe VIII, XX, and XXIII	4.0×10^5 K, 1.0×10^7 K, and 1.5×10^7 K
171 Å	Fe IX/X	1.0×10^6 K
193 Å	Fe XII and XXIV	1.2×10^6 K and 2.0×10^7 K
211 Å	Fe XIV	2.0×10^6 K
335 Å	Fe XVI	2.5×10^6 K

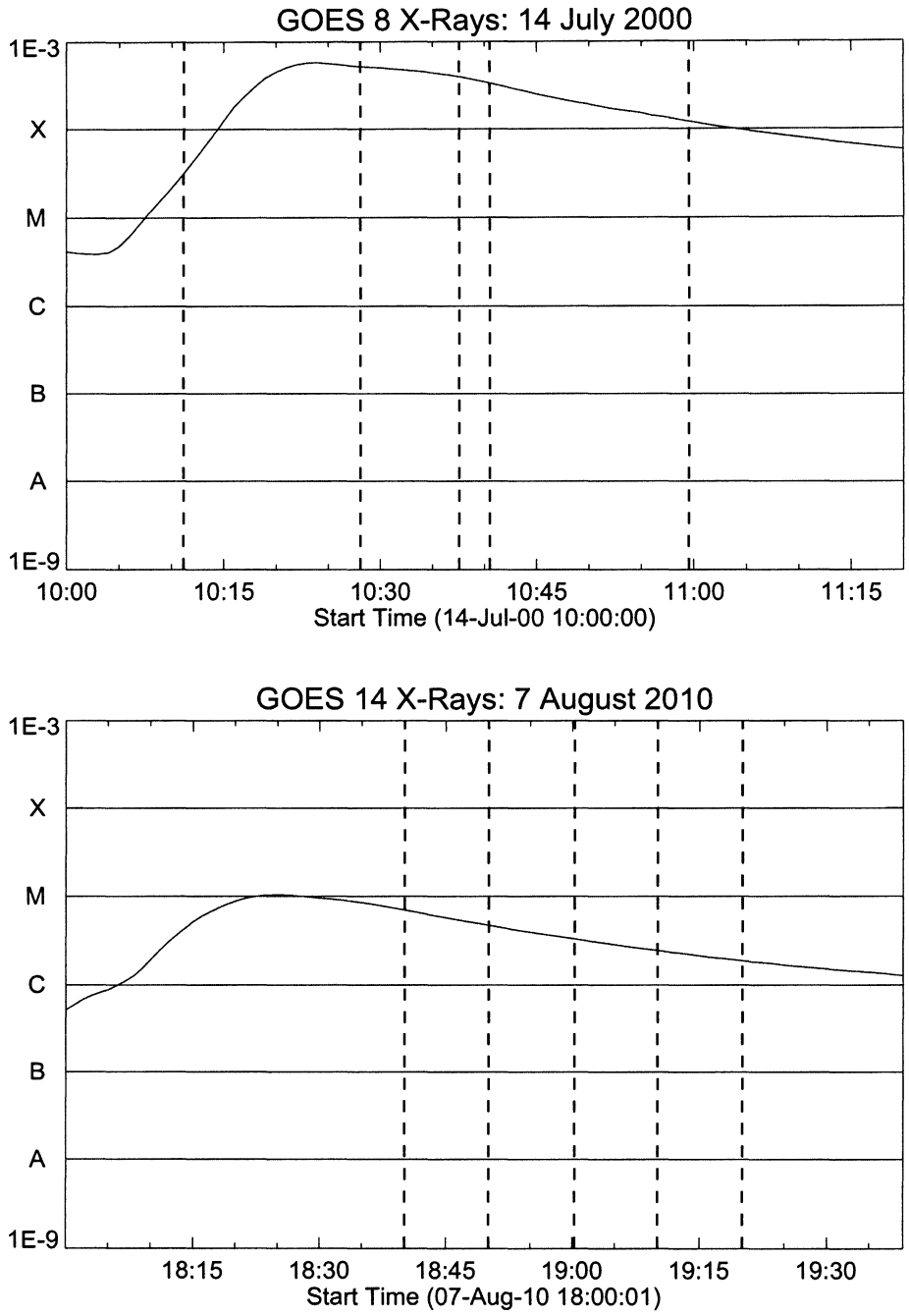

Figure 5.3: X-Ray flux observed by the GOES satellites, GOES 8 and GOES 14, during the flares of 14 July 2000 (top panel) and 7 August 2010 (bottom panel). The y-axis gives the flare magnitude. The dashed vertical lines show the times at which coronal loops were traced.

Table 5.4. Image and loop tracing information for AR 9077 and 11093.

Observing Instrument	Observation Date	Time of Peak X-Ray Flux	Observation Times (UT)	Number of Loops	Points per Loop
TRACE	14 July 2000	10:20 UT	10:11	3	36
			10:28	35	34-36
			10:37	71	34-36
			10:40	90	34-36
			10:59	106	34-36
AIA	7 August 2010	18:25 UT	18:40	79	18-43
			18:50	93	18-36
			19:00	103	18-52
			19:10	126	18-44
			19:20	102	18-61

5.4 Dipole Modeling of Post-Flare Loops

5.4.1 The Dipole Model

The dipole model is discussed in detail in Chapter 4; this section contains only a brief review. The far-field approximation of the field due to a magnetic dipole is described as follows (Jackson, 1999):

$$\mathbf{B}(\mathbf{r}) = \frac{\mu_0}{4\pi}\left[\frac{3\mathbf{n}(\mathbf{n}\cdot\mathbf{m}) - \mathbf{m}}{|\mathbf{r}-\mathbf{r}_0|^3}\right], \tag{5.7}$$

where $\mathbf{m}$ is the magnetic moment of the dipole, $\mathbf{r} = (x, y, z)$ is the position vector indicating the point at which the field is calculated, and $\mathbf{r}_0$ the position vector indicating the location of the dipole, (x_0, y_0, z_0). The normal vector between the field

position and the dipole position is given by $\mathbf{n} = (\mathbf{r} - \mathbf{r}_0)/|\mathbf{r} - \mathbf{r}_0|$. In order to describe a field with complex topology, one can superimpose multiple dipoles, resulting the following general expression for the field:

$$\mathbf{B} = \sum_{i=1}^{n} \mathbf{B}_i(\mathbf{r}_i) = \sum_{i=1}^{n} \frac{\mu_0}{4\pi} \left[\frac{3\hat{\mathbf{r}}_i (\hat{\mathbf{r}}_i \cdot \mathbf{m}_i) - \mathbf{m}_i}{|\mathbf{r}_i|^3} \right]. \tag{5.8}$$

for n the number of dipoles used.

5.4.2 Dipole Placement

In Chapter 4, the configuration of the dipoles was done via the automated optimization of manually determined initial guesses. The dipole placement was performed in an iterative manner: the user provided an initial guess for the dipole's location and orientation, and the parameters were optimized by minimizing the resulting misalignment angle via the Powell method. Subsequent dipoles were added in a similar way.

In the case of the post-flare loops studied here, however, the dipoles' positions are configured solely by hand: the goal of the dipole modeling discussed in Chapter 4 was to model the active regions as closely as possible with submerged dipoles, whereas for these active regions, we wish to determine the observed loops' departure from a certain configuration. Both active regions have a relatively simple arcade structure: mostly semicircular loops in a compact structure that resembles a curved half-cylinder resting on the solar surface. In their simplest state, such arcades are well represented by a series of loops lying orthogonal ($\phi = 90°$) to the neutral line (which runs the

length of the active region and separates areas of opposite magnetic polarity). Loop arcades can also be *sheared*, meaning that the loops make an angle $\phi < 90°$ with the neutral line.

Both AR 9077 and AR 11093 display loop arcades with a degree of shear that appears to decrease with time after the flare. In creating dipole models of these active regions, the objective is not to match the structure of the loops exactly, but to create models of the active regions that retain the same overall shape without the shear observed in the coronal loops. Our interest lies primarily in the trend in misalignment angle with time. The misalignment angles calculated from the resulting model and the observed structures quantify the amount of shear exhibited by the real coronal field. These calculations will provide a basis for further study using a simple sheared arcade model (see Section 5.5).

5.4.3 Dipole Results

Dipole Model of AR 9077

The long, "slinky"-like arcade of loops seen in AR 9077 requires a total of eight dipoles in order to achieve loop structures that run perpendicular to the neutral line along its entire length. The field lines for this model can be seen plotted in blue in the bottom panel of Figure 5.5. The field lines are drawn for footpoint coordinates identical to those of the loops shown in the middle panel of Figure 5.5, and are shown plotted over a map of the $z-$component of the model magnetic field, $\mathbf{B}_{dipole,z}$.

The loops identified in TRACE images of the active region are shown in Figures 5.4 and 5.5. Each loop is colored according to the median misalignment angle (2D misalignment angle) along that loop. Dark red and brown loops have very low misalignment (low shear with respect to the neutral line), and bright orange and yellow loops are highly misaligned (highly sheared). The median misalignment angle over the entire active region at a given time is shown in the title of the panel for that time.

The misalignment angle distributions are also collected in five histograms in Figure 5.6, each of which also shows the median misalignment angle as a dashed vertical line. The median misalignment angles for all five times are shown in the bottom right panel of Figure 5.6, and in Table 5.5. Over the course of the images studied, the overall misalignment angle decreases monotonically from 70.8° to 20.8°. The measurement in a later time interval (52.2° to 20.8°) may be more representative, as the image that yielded a 70.8° misalignment contained only three identifiable loops. Nevertheless, both the median misalignment angles and the misalignment angle distributions for the five times sampled (see misalignment angle distributions in Figure 5.6) show an unambiguous trend toward lower misalignment angles with time.

It is also interesting to examine areas of AR 9077 separately. The loops plotted in Figures 5.4 and 5.5 appear to have different rates of evolution. Loops first appear on the right (western) side of the active region, and the shear displayed by these loops begins to decrease by the bottom panel (t = 10:37 UT) of Figure 5.4. By contrast, the first loops do not appear on the left (eastern) side of the active region

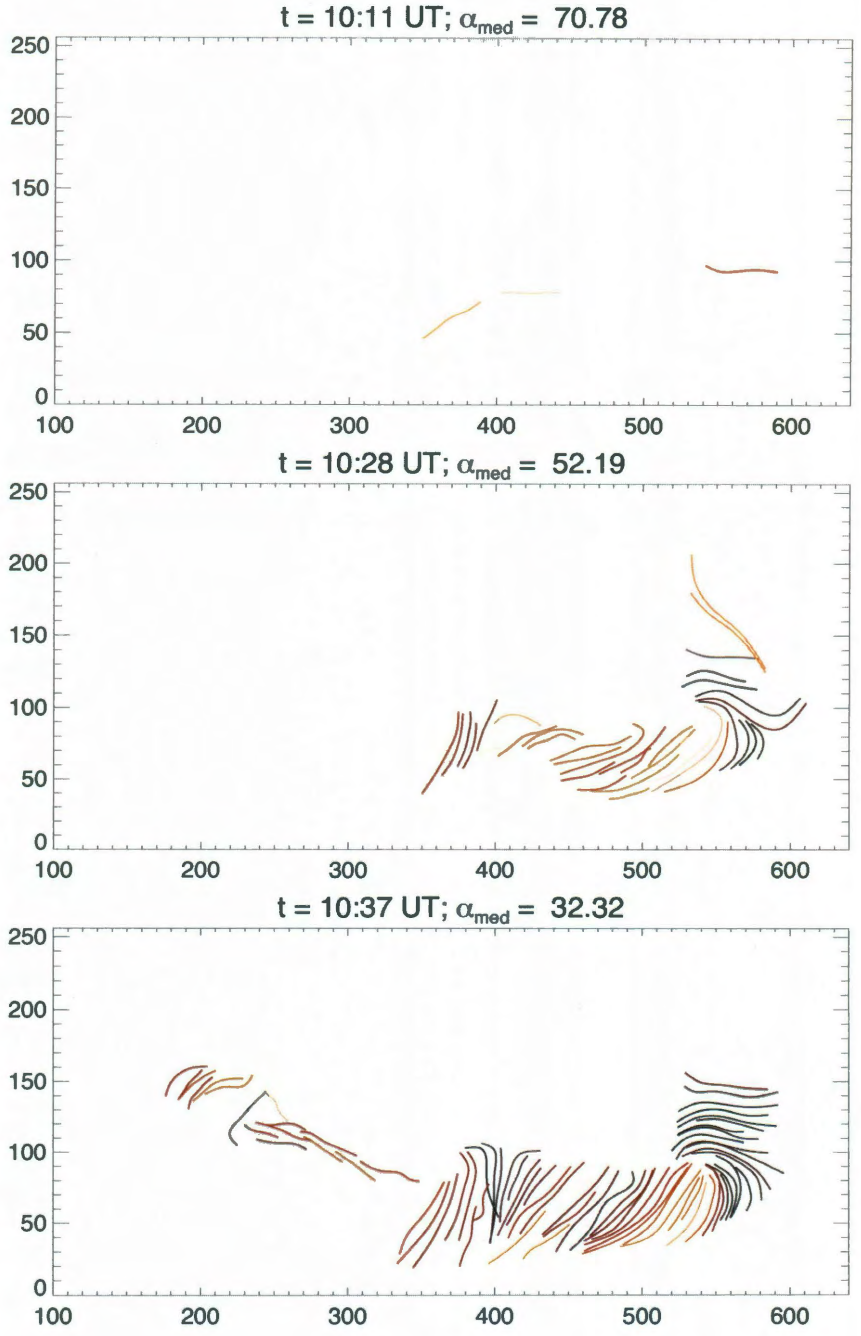

Figure 5.4: Coronal loops observed by TRACE at 10:11, 10:28, and 10:37 UT following an X-class flare in AR 9077 on 14 July 2000 (peak X-ray flux occurred at 10:23 UT). The loops are colored according to their misalignment with the dipole model of the active region.

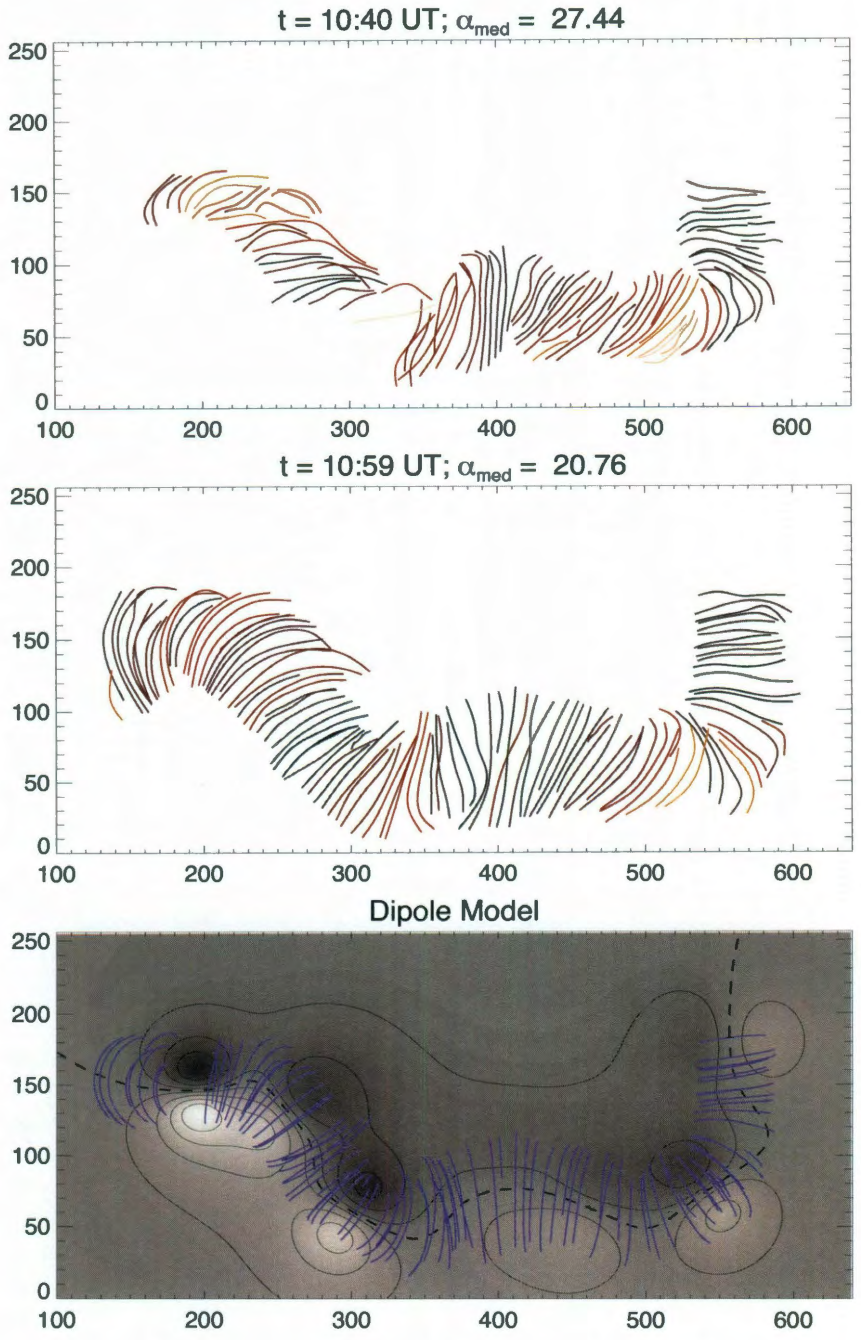

Figure 5.5: Top and middle panels: coronal loops observed by TRACE at 10:40 and 10:59 UT following an X-class flare in AR 9077 on 14 July 2000 (peak X-ray flux occurred at 10:23 UT). The loops are colored according to their misalignment with the dipole model of the active region. Bottom panel: model magnetic field lines (blue) are plotted over a map of the z-component of the dipole (model) magnetic field at the solar surface.

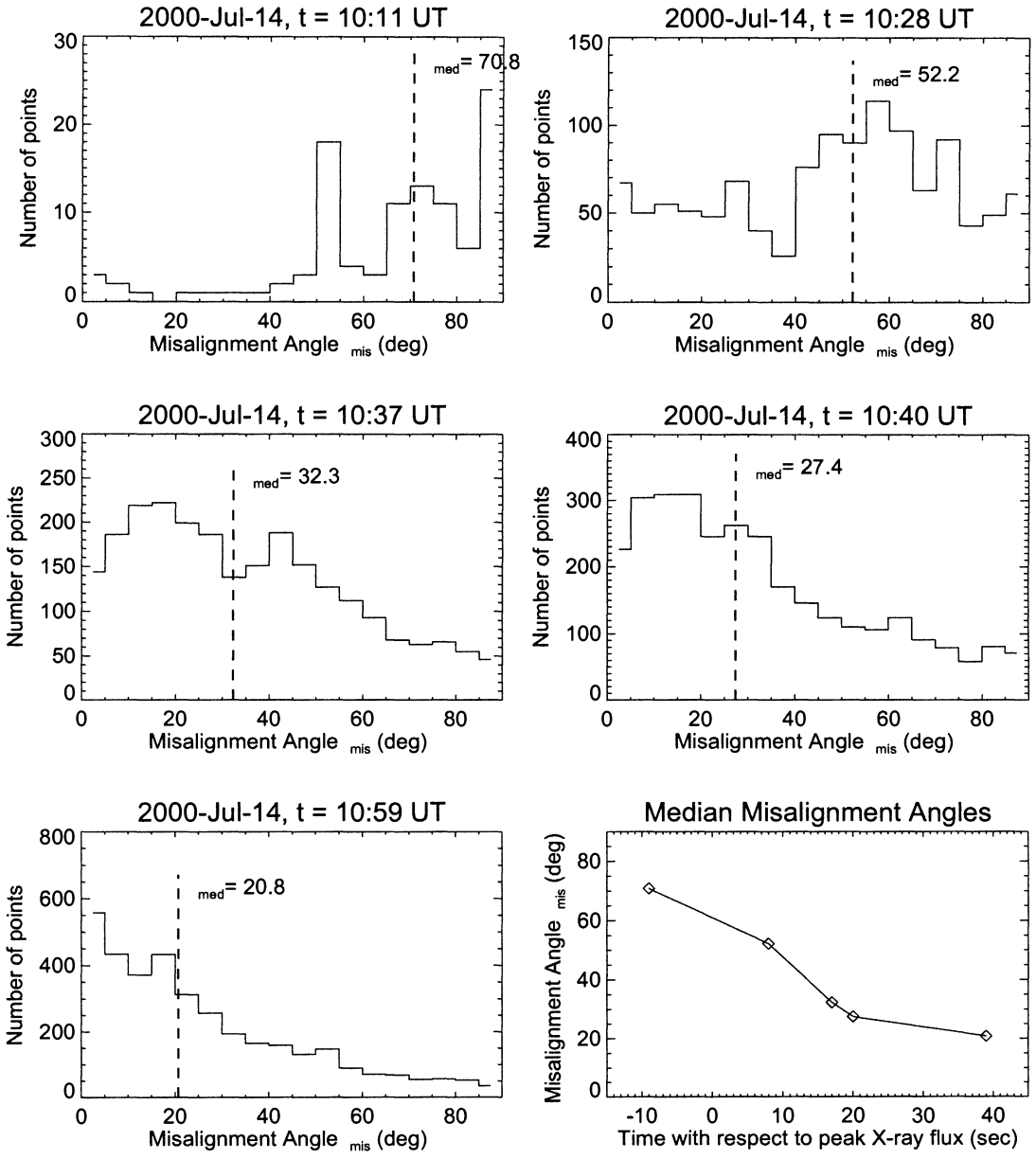

Figure 5.6: Misalignment angle distributions for coronal loops observed at five different times following an X-class flare in AR 9077 at 10:23 UT on 14 July 2000.

until $t = 10{:}37$. Figures 5.7 and 5.8 chart the evolution of the two halves of the active region independently. Each group of loops shows similar behavior with time, with the progress of the left half (Figure 5.8) simply delayed by approximately 25 minutes.

Dipole Model of AR 11093

In the case of AR 11093, six dipoles are sufficient to produce an arcade with the correct morphology. The model field can be seen in the lower right panel of Figure 5.9, with field lines plotted in blue over a map of the $z-$component of the model field at the photosphere. The observed coronal loops are plotted in the first five panels of Figure 5.9, and, as in Figures 5.4 and 5.5, are colored according to their median misalignment angle along each loop. Darker loops (brown and dark red) indicate a low misalignment angle, i.e. closer agreement between the model and the observed field structure. Brighter loops (orange and yellow) indicate high misalignment, i.e. poor agreement between the model and observations.

The median misalignment angles for the active region at each point in time are shown as histograms in Figure 5.10. As in Figure 5.6, the overall median misalignment angles are shown as dashed vertical lines in the corresponding histograms, and collected in the lower right panel of the figure. The median misalignments are also given in Table 5.5. The angles do not display the monotonic behavior seen in AR 9077; rather, the median misalignment angle remains at a plateau for approximately 20 minutes. However, the overall trend is from a state of high misalignment (high shear) to one of lower misalignment (lower shear).

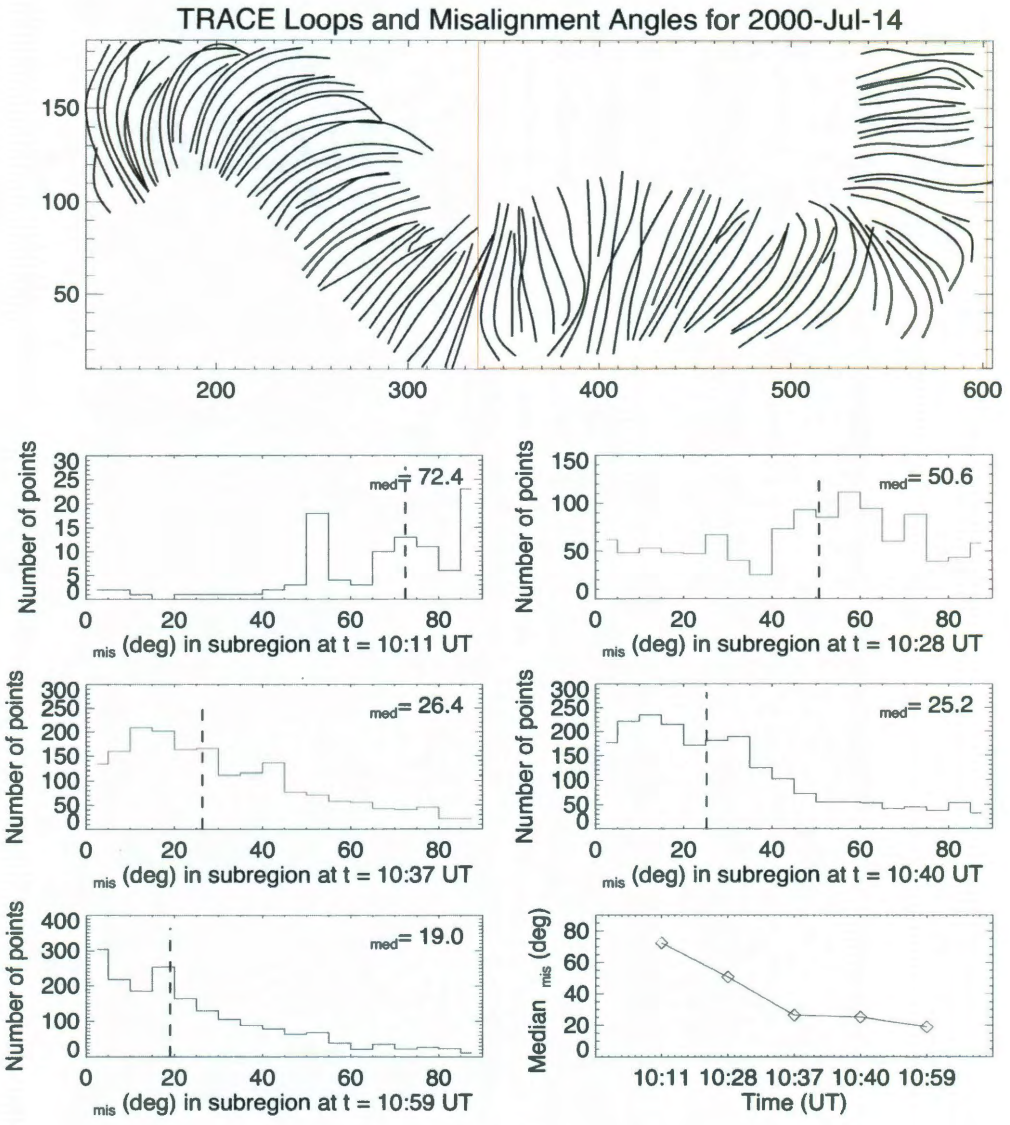

Figure 5.7: Misalignment angles for loops on the right-hand side of the active region (region outlined in red in top panel).

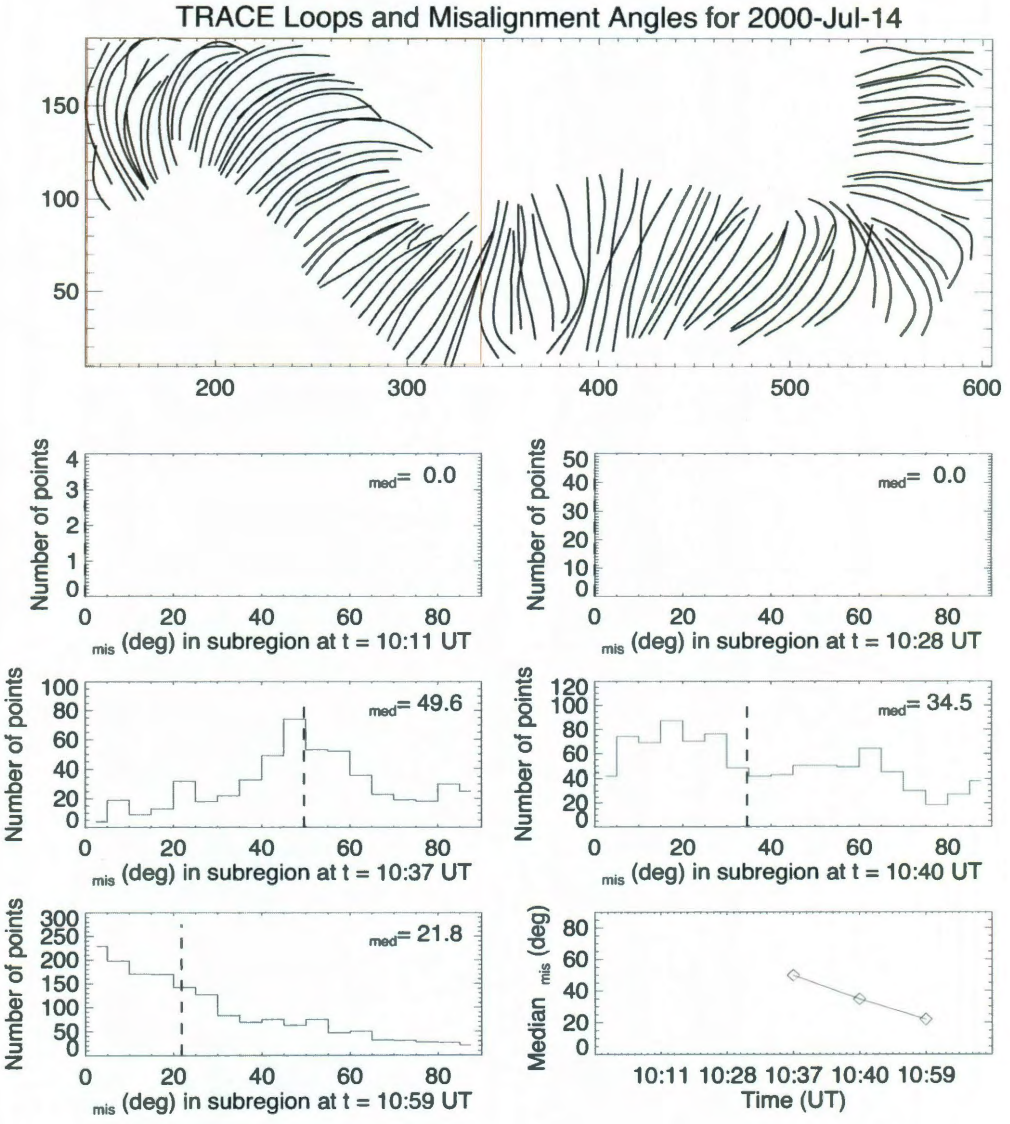

Figure 5.8: Misalignment angles for loops on the left-hand side of the active region (region outlined in red in top panel).

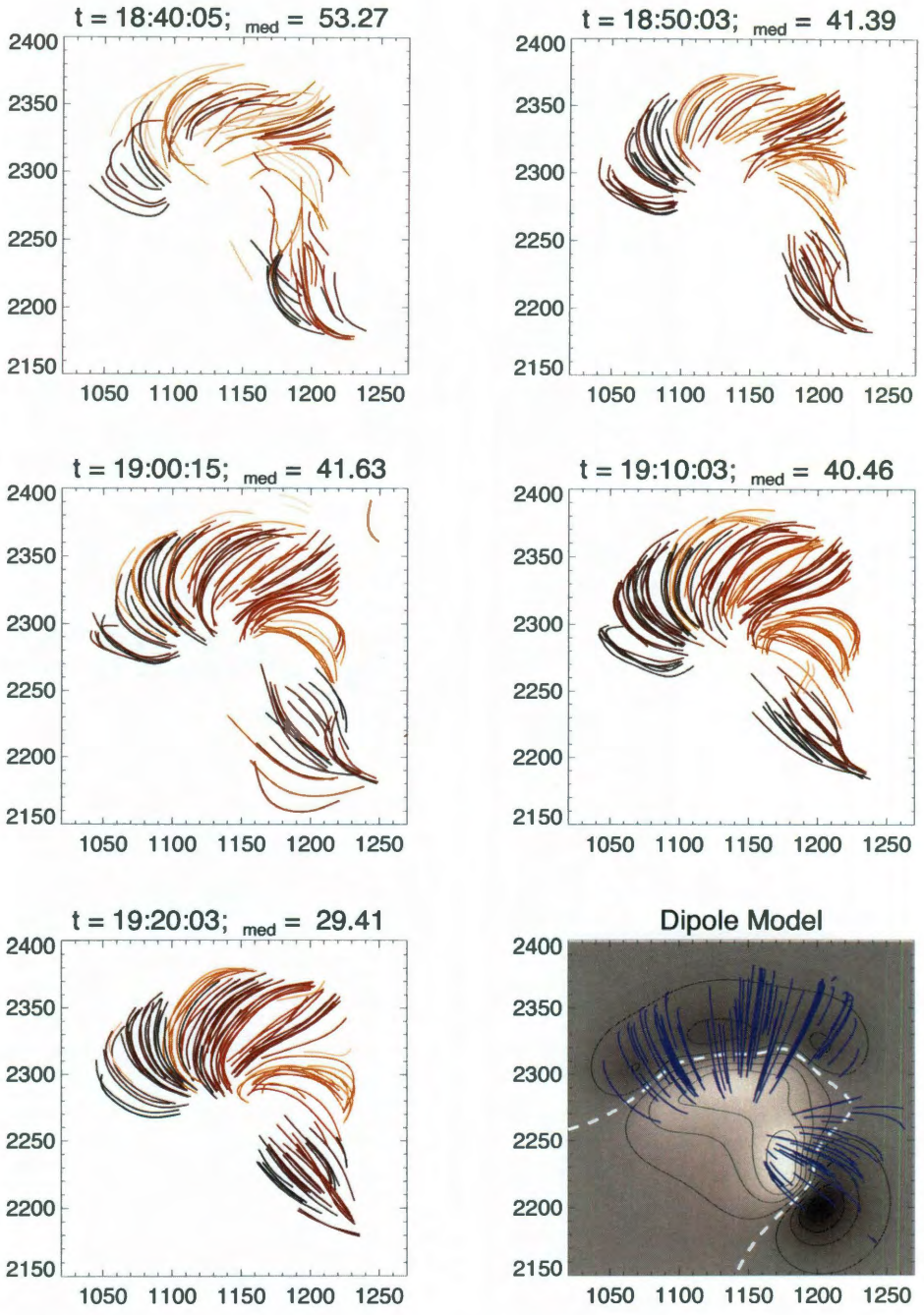

Figure 5.9: Coronal loops observed following an M-class flare in AR 11093 at 18:25 UT on 7 August 2010. The loops are colored according to their misalignment with the dipole model of the active region. The model field is shown in the bottom right panel: magnetic field lines (blue) are plotted over a map of the z-component of the model magnetic field at the solar surface.

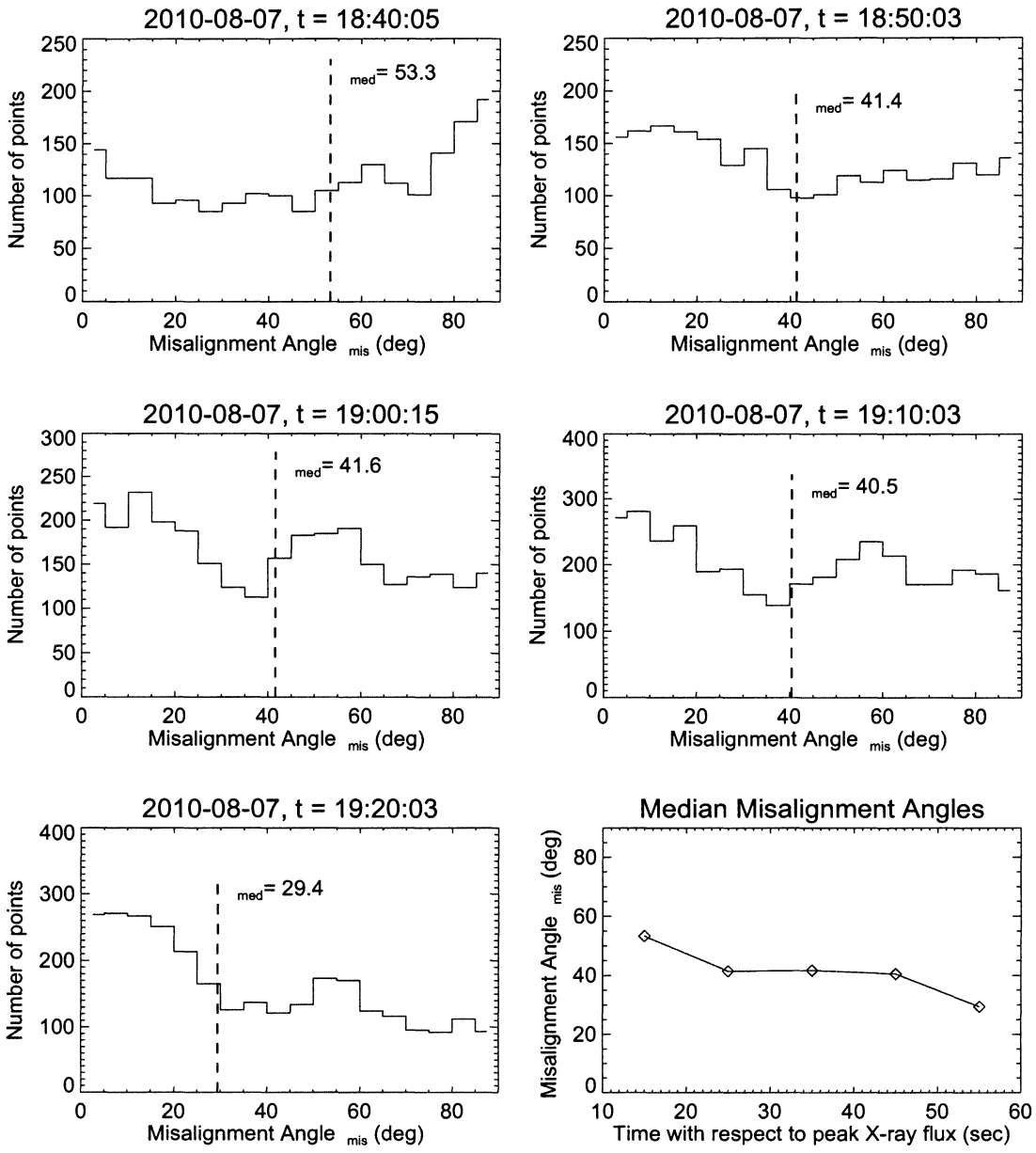

Figure 5.10: Misalignment angle distributions for coronal loops observed at five different times following an M-class flare in AR 11093 at 18:25 UT on 7 August 2010. Representation is similar to Figure 5.6.

Table 5.5. Misalignment angles (2D) at five times for two flaring active regions: AR 9077 (14 July 2000) and AR 11093 (7 August 2010).

Observation Date	Time of Peak X-Ray Flux (UT)	Observation Times (UT)	Median Misalignment Angle
14 July 2000	10:20	10:11	70.8°
		10:28	52.2°
		10:37	32.3°
		10:40	27.4°
		10:59	20.8°
7 August 2010	18:25	18:40	53.3°
		18:50	41.4°
		19:00	41.6°
		19:10	40.5°
		19:20	29.4°

5.5 Energy Estimates

In this section, we present an estimate of the energy contained in magnetic fields displaying degrees of shear comparable to what is observed in ARs 9077 and 11093 above. While the reduction in misalignment angles does in itself demonstrate the relaxation of the field over the course of the flare, estimates of the non-potential energy stored in the magnetic field provide another measure of the relaxation process. Since it is likely that the shearing of the field is due to electrical currents embedded in the field, estimation of the energy contained in the field necessitates a departure from the potential (current-free) dipole model used here. The dipole model provides the initial energy value (for an unsheared, potential field), but calculations of the energy of the sheared fields require a model field that includes currents. The simple model

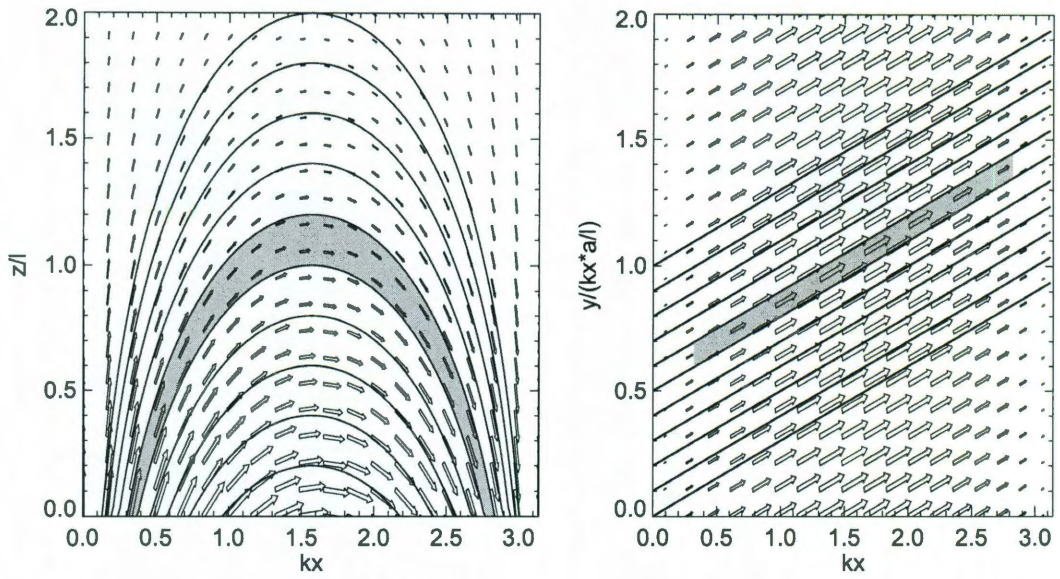

Figure 5.11: Geometry of the force-free sheared arcade magnetic field model. The field is shown in the x-z plane (left) and in the x-y plane (right). Each panel shows the field vectors (arrows) and lines of magnetic force (curved lines). The shear angle θ is simply the slope of the lines in the right panel (Aschwanden, 2004).

used in this study is described below.

5.5.1 Sheared Arcade Model

Because the active regions to be modeled can be treated as simple arcades, a suitable non-potential model is the sheared arcade. One such formulation was originally presented in Priest (1982), and can also be found in Sturrock (1994) and Aschwanden (2004). The field is periodic in x and falls off exponentially with height z:

$$B_x = B_{x0} \sin(kx) \exp(-lz) \tag{5.9}$$

$$B_y = B_{y0} \sin(kx) \exp(-lz) \tag{5.10}$$

$$B_z = B_0 \cos(kx) \exp(-lz) \tag{5.11}$$

Taking the curl ($\nabla \times \mathbf{B}$) of the above equations yields:

$$(\nabla \times \mathbf{B})_x = \frac{\partial B_z}{\partial y} - \frac{\partial B_y}{\partial z} = lB_{y0} \sin(kx) \exp(-lz) \tag{5.12}$$

$$(\nabla \times \mathbf{B})_y = \frac{\partial B_x}{\partial z} - \frac{\partial B_z}{\partial x} = (-lB_{x0} + kB_0) \sin(kx) \exp(-lz) \tag{5.13}$$

$$(\nabla \times \mathbf{B})_z = \frac{\partial B_y}{\partial x} - \frac{\partial B_x}{\partial y} = kB_{y0} \cos(kx) \exp(-lz) \tag{5.14}$$

In order for a magnetic field to be considered *force-free*, the curl of the field must be parallel to the field itself (i.e. the Lorentz force is zero, see Appendix B). This requirement is illustrated in the following equation:

$$(\nabla \times \mathbf{B}) = \lambda \mathbf{B} \tag{5.15}$$

Using this condition with the equations for $\nabla \times \mathbf{B}$ above, one can relate the field constants as follows:

$$lB_{y0} = \lambda B_{x0} \tag{5.16}$$

$$(-lB_{x0} + kB_0) = \lambda B_{y0} \tag{5.17}$$

$$kB_{y0} = \lambda B_0 \tag{5.18}$$

After some reduction, the above equations yield the field coefficients B_{x0} and B_{y0} in terms of the parameters l, k, and λ:

$$B_{x0} = \frac{l}{k} B_0 \tag{5.19}$$

$$B_{x0} = \frac{\lambda}{k} B_0 \tag{5.20}$$

$$k^2 - l^2 - \lambda^2 = 0 \tag{5.21}$$

The field lines associated with the resulting field lie in a plane that is perpendicular to the x-y plane and makes an angle θ with the x-axis (see Figure 5.11):

$$\tan\theta = \frac{B_y}{B_x} = \frac{B_{y0}}{B_{x0}} = \frac{\lambda}{l} \tag{5.22}$$

This angle, θ, is analogous to the misalignment angle, α, measured for the observed coronal loops in ARs 9077 and 11093[2]. Indeed, it is the values of α given in Table 5.5 that determine the shear of the model fields.

For each time t, at which loops have been traced (times given in Tables 5.4 and 5.5), the energy contained in the dipole (current-free) model field is calculated as a baseline. Because the field is known at all points, the total energy in the field is straightforwardly calculated by evaluating the energy at a given location, $E_i = B_i^2/8\pi$,

[2]Recall that in Chapter 4, the shear angle (θ) was considered interchangeable not with the misalignment angle itself (α), but with the *non-potentiality* (α_{NP}), which was added in quadrature with the stereoscopic error (α_{SE}) to form the total misalignment angle: $\alpha^2 = \alpha_{SE}^2 + \alpha_{NP}^2$. When tracing loops in single images, however, the loop coordinates are not subject to the factors that contribute to stereoscopic error, so α_{SE} vanishes and α can be considered interchangeable with α_{NP} (and therefore with θ).

at all points:

$$E_B = \frac{1}{8\pi} \sum_{i=1}^{nx} \sum_{j=1}^{ny} \sum_{k=1}^{nz} B\left(x_i, y_j, z_k\right)^2 \tag{5.23}$$

where nx, ny, and nz are the number of points in the $x-$, $y-$, and $z-$directions, respectively. Because the dipole model is constrained only by loop coordinates traced in coronal images, the magnetic field is dimensionless. As a result, the energy obtained using equation 5.23 is also dimensionless. For consistency, the energy contained in the sheared arcade model is therefore normalized to the value obtained for the dipole field. The normalization is accomplished by adjusting the parameters l and k such that for $\theta = 0$ (zero shear and zero misalignment, i.e. the potential field), the energy calculated for the force-free sheared arcade, E_{FF}, is identical to the energy of the dipole field, E_{dipole}. The energies for the fields with nonzero shear are then calculated by varying θ using the misalignment angles given in Table 5.5.

5.5.2 Sheared Arcade Results

The energy estimates for the dipole field, the unsheared force-free field, and the five different sheared arcades for ARs 9077 and 11093 are given in Table 5.6. The table provides the ratios of the energies of the force-free fields (E_{FF}) to the energies of the dipole fields (E_{dipole}). These ratios can also be seen plotted as a function of the misalignment angle (or shear angle) in Figure 5.12. For AR 9077, the highly sheared loops at t = 10:11 UT result in a field with 260% of the energy of the dipole field for that active region. By the end of the observing period (t = 10:59 UT) the field has lost

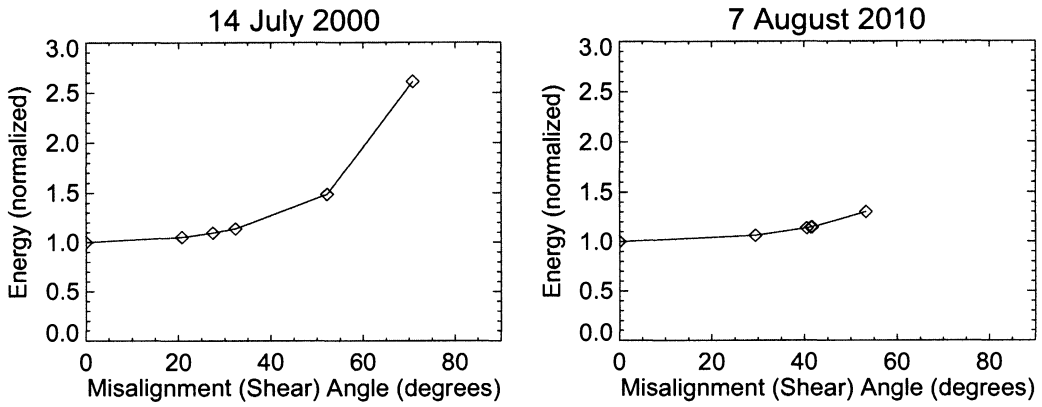

Figure 5.12: Energy estimates for sheared arcade models of ARs 9077 (left panel) and 11093 (right panel) with varying degrees of shear. The shear angle is determined by the median misalignment angle found between the observed loops and the dipole model at each of five times.

59.7% of the energy initially measured. The loops in AR 11093 achieve a maximum energy of 130% of the energy of the dipole field for that active region. At the end of the observing period for this flare (t =18:40 UT), the active region has lost 18.3% of the energy measured for the first loop tracing. These energy estimates provide a measure of the non-potentiality of the field configuration at different points during the post-flare relaxation of the field, and give a more direct indication of the free energy contained in the field than the non-potentiality parameter calculated in Chapter 4. An interesting topic of future study would be the linking of these calculations with magnetic field measurements in order to achieve physical values for the energy in the field (see Section 5.6 and Chapter 6).

Table 5.6. Energy estimates for dipole and sheared arcade models of the two active regions in the aftermath of large flares.

Field Type	14 July 2000 Misalignment Angle	14 July 2000 Estimated Field Energy	14 July 2000 Ratio E_{FF}/E_{dipole}	7 August 2010 Misalignment Angle	7 August 2010 Estimated Field Energy	7 August 2010 Ratio E_{FF}/E_{dipole}
Dipole field	...	150.56	1.00	...	72.47	1.00
Unsheared arcade	...	150.58	1.00	...	72.48	1.00
Sheared arcade ($t = t_1$)	70.78°	392.90	2.61	53.27°	94.25	1.30
Sheared arcade ($t = t_2$)	52.19°	223.61	1.49	41.39°	82.92	1.14
Sheared arcade ($t = t_3$)	32.32°	171.22	1.14	41.63°	83.06	1.15
Sheared arcade ($t = t_4$)	27.44°	164.92	1.10	40.46°	82.35	1.14
Sheared arcade ($t = t_5$)	20.76°	158.40	1.05	29.41°	77.01	1.06

5.6 Discussion

One of the questions raised by the results of Chapter 4 was whether or not one could expect to observe any relaxation of the magnetic field following a solar flare. One of the active regions studied, AR 10956, experienced a minor flare, and it was expected that the field would visibly relax following the flare. Such a relaxation was not observed, and it was not clear from the results whether the absence of any discernible shift toward a more potential state was influenced by the fact that the flare was small (GOES B-class), or if there were other factors at work.

The results presented in this chapter support the theory that the small size of the flare in AR 10956 was the dominant factor affecting the lack of visible field relaxation in the aftermath of the flare. We have analyzed two large flares (an X-class flare on 14 July 2000 and an M-class flare on 7 August 2010) and found that the loop structures for those active regions exhibit significant relaxation following the peak soft X-ray flux associated with the flare. The extent of the relaxation is correlated with the magnitude of the flare in the two cases studied here, but a more extensive survey of similar events is necessary in order to identify a statistically significant correlation.

The change in misalignment angles between the earliest and latest times at which loops were traced appears to be significant even after accounting for the extent to which the 2D misalignment undervalues the true 3D misalignment. Based on analysis of four active regions for which stereoscopic images are available, the 2D misalignment angle underestimates the 3D misalignment angle by 44±24%. For AR 9077, with

an initial misalignment of 70.8° and a final misalignment of 20.8°, the change in misalignment, $\Delta\alpha = 50°$, is well outside of the uncertainty in the misalignment angle measurement. AR 11093 experiences a less dramatic decrease in misalignment angle, but with an initial misalignment of 53.3° and a final misalignment of 29.4°, the change, $\Delta\alpha = 23.9°$, is nevertheless substantial. Thus, this work confirms that for sufficiently large flares, the relaxation of the field is observable and can be measured using the dipole model.

These misalignment angle calculations facilitate the modeling of the active regions via an alternative method using simple sheared arcades. The shear angle of the arcade is determined by the median misalignment angle of the active region, which is measured using traced coronal loops and a dipole field model. Consistent with the change in misalignment angle, AR 9077 experiences a much larger change in energy between the initial and final states than does AR 11093. These early results could be advanced by providing some observational basis for the magnetic field model, such as matching the net flux between the model and observations of the region. The energies calculated for the model fields would then no longer be dimensionless, and the change in energy could be compared with other observational indications of energy loss. This potential future work will be discussed further in Chapter 6.

Chapter 6

Conclusions

The magnetic field governs the behavior of the solar atmosphere. From the movement of the coronal plasma to the way in which the plasma is heated, the magnetic field dominates most aspects of coronal structure and dynamics. Even interplanetary space is subject to the workings of the coronal magnetic field, as it is through the field that energetic phenomena such as flares and coronal mass ejections are initiated. The storms associated with these events travel outward from the corona through the heliosphere, and frequently interact with the Earth's environment.

The role of the coronal magnetic field makes its study an important part of any effort to understand the corona as a whole. These efforts are hindered, however, by difficulties in directly measuring the coronal field. Unlike in the photosphere, where the field is is readily observable via measurement of the Zeeman splitting of spectral lines, the conditions in the corona preclude the use of this technique (see Section 2.1.2). There exist other methods for measuring the magnetic field under coronal

conditions, but they are not yet suitable for the large-scale observations necessary for a comprehensive understanding of the field.

The obstacles to direct measurement of the coronal magnetic field motivate the use of analytical and numerical models as theoretical supplements for observations. Through models it is possible to verify or challenge certain assumptions, leading to a better understanding of the field. However, models are not without their own disadvantages: as discussed in Chapter 2, the analytical methods commonly used to simulate the coronal magnetic field are often undermined by the use of photospheric magnetograms as the basis for the models' lower boundary condition. In the corona, the magnetic field is thought to be *force-free* (Schrijver & van Ballegooijen, 2005), i.e. the electrical currents embedded in the field run parallel to the field, and the Lorentz force is negligible ($\mathbf{j} \times \mathbf{B} = 0$, see Appendix B). The photosphere, however, is a forced system, and the currents may also flow across the field. The photospheric field is therefore said to be *non-force-free* ($\mathbf{j} \times \mathbf{B} \neq 0$). This discrepancy between the nature of the currents in the two domains represents a critical inconsistency between the lower boundary condition and simulation domain.

This problem was thrown into relief following the availability of stereoscopic imaging of the Sun. Historically, coronal imaging has been restricted to single images from only one point of view. Because the corona is optically thin, the loops of bright plasma that illustrate the structure of the magnetic field in the corona are conflated in the line-of-sight projection resulting from the sum of all emission along the line of sight.

It is thus impossible to discern the field's full 3D structure using only single images of the corona.

With the launch of the *Solar Terrestrial Relations Observatory* (STEREO) in 2006, observers had access to images of the Sun from two novel perspectives: twin spacecraft, one traveling ahead of Earth and the other trailing behind Earth. The Extreme Ultraviolet Imager (EUVI) instruments on both STEREO spacecraft take simultaneous images of the corona from different vantage points, allowing observers to investigate the 3D coronal magnetic field for the first time. Using triangulation of loops traced in both sets of images, it is possible to reconstruct the full 3D structure of the magnetic field (see Section 3.4.2 and Appendix D). One can compare the resulting structures with the structure of the field given by magnetic models. In Chapter 3, we used this method to examine the success of one widely used modeling technique, the Potential Field Source Surface (PFSS) model, in simulating the magnetic field structure of active regions. We found that while the PFSS model is more successful at modeling some active regions than others, overall it does not do a good job at representing well the active region magnetic fields.

The conclusion that the PFSS model does not excel at modeling coronal active regions was unsurprising: as noted above, the corona is believed to carry currents, and the PFSS technique uses a current-free field in the lower corona. (At the source surface, however, there are surface currents that force the field to become radial; see Chapter 2.) This study provides a baseline measure of success that allows a

direct comparison between the PFSS models of these active regions with other models of similar active regions. Such a comparison can readily be made with the non-linear force-free field (NLFFF) models tested by DeRosa et al. (2009) for one of the active regions studied here (AR 10953). The NLFFF models demonstrated overall misalignment angles with the STEREO-observed coronal magnetic field structure that was at best comparable to the misalignment calculated for the PFSS model of that active region (25°), and at worst 20° larger. Although there may be additional factors at play in this result (see Section 3.6), the findings of both the PFSS and NLFFF studies point to the necessity of developing new modeling techniques. These techniques must either make use of alternative boundary conditions or address in a more realistic way the transition between the non-force-free photosphere and the force-free corona.

In Chapter 4, we presented a new magnetic modeling method that avoids the difficulty posed by boundary conditions based on photospheric magnetograms. This technique configures submerged magnetic dipoles based on the structure of the coronal magnetic field observed in EUV images. While these images cannot constrain the magnitude of the field, they allow the parameters of the model field to be fitted to the observed field morphology. In the case of images from STEREO/EUVI, this fitting can be performed using the full 3D geometry, which provides a more reliable set of constraints on the model field than the 2D projected geometry that can be obtained from single images. Based on calculations of the misalignment between the model and

observed field structures for four active regions, the dipole models provided a closer agreement with the observed field geometry than the PFSS or NLFFF models. In some cases, the overall misalignment angle was reduced by a factor of two or more (see Section 4.5). The dipole model field is potential, and therefore not as realistic a model of the coronal field as one that carries currents (e.g. a more general, force-free field). Despite this fact, the dipole approach achieves lower misalignment angles than either PFSS or NLFFF models. Although the current-carrying NLFFF models are expected to be better suited to modeling the presumably non-potential corona, the fact that a potential field such as the dipole model outperforms the NLFFF model illustrates the need for modeling techniques that include a more appropriate treatment of the photosphere and corona.

The results of the dipole modeling of four active regions presented in Chapter 4 demonstrate the relative success of a modeling approach that is unimpeded by the incompatibility between a force-free modeling domain and a non-force-free boundary condition, but they also raised questions about the behavior of an active region magnetic field over the course of a solar flare. One of the active regions studied, AR 10956, experienced a minor solar flare (GOES B-class) and partial filament eruption. One would expect that following the release of energy in the flare, the active region magnetic field would evolve from a stressed configuration with significant electrical currents to a less stressed, more potential configuration, and that this change would be reflected in the pre- and post-flare misalignment angles. However, such a change

was not observed, and it was noted that further study of similar events was necessary in order to explain the unexpected result.

Unfortunately, during the first year of the STEREO mission, when the spacecraft were optimally positioned for stereoscopy of observed loop structures, the Sun was in the midst of an unusually quiet solar minimum. Other than AR 10956, there are no flare-producing active regions in the STEREO catalogue that were both present during the first year of the mission and positioned appropriately for stereoscopy (that is, visible to both spacecraft). Studies of additional flaring active regions are therefore restricted to observations from a single viewpoint, which cannot constrain the third dimension of the field geometry. Nevertheless, although the STEREO/EUVI instruments are no longer providing images that are suitable for triangulation of coronal loops, the active regions for which stereoscopy was possible have a lasting utility.

The same misalignment analysis of 2D loops seen in projection and traced in single images taken by instruments such as the *Transition Region and Coronal Explorer* (TRACE) and the Atmospheric Imaging Assembly (AIA) on board the *Solar Dynamics Observatory* (SDO) can also be performed for STEREO/EUVI images. The resulting misalignment angles can then be compared with the misalignment angles calculated for the full 3D structures, yielding an estimate of the degree to which the 2D misalignment underestimates the true 3D misalignment. In this way, although one cannot determine the 3D structure of the coronal magnetic field for active regions observed before or after the prime stereoscopy period, it is possible to estimate

the accuracy of a 2D comparison between a model field and the projected 2D field geometry obtained from single images. We performed this study for the four active regions for which the dipole model was originally tested, and found that the 2D misalignment calculated using only images from the STEREO-A (Ahead) spacecraft underestimated the 3D misalignment by $44 \pm 24\%$.

In the absence of stereoscopic image pairs for the examination of additional flare events to compare with the behavior of AR 10956, the examination of the 2D misalignment angle provided a baseline for dipole model analysis of active regions observed only in 2D. Using this baseline, we used the dipole modeling technique to study two large flares: one an X-class flare observed by TRACE, and the other an M-class flare observed by SDO/AIA. Both active regions exhibited a post-flare reduction in misalignment angle that was significant despite the inherent 2D underestimation of the full 3D misalignment angle. This result indicates that it is likely that the B-class flare observed by STEREO in AR 10956 was not sufficiently powerful to effect an observable change in the magnetic field configuration (and therefore in the misalignment angle). The change in misalignment angle also confirms that it is reasonable to expect the magnetic field to relax visibly following a large flare.

In addition to the ways in which one can use the dipole model directly to explore the nature and behavior of the coronal magnetic field, it can be used as a foundation for broader study of the field using other models. The sheared arcade model discussed in Section 5.5 can be configured for a given active region based on the dipole model

for that active region. The energy contained in the current-free dipole model of the region provides the minimum energy state needed to initialize the field constants (equation 5.21), and the overall misalignment angle calculated for a dipole model gives the shear angle for the arcade. As presented in Section 5.5, the field and energy are dimensionless, but future work on the technique could include an observationally derived basis for physical values of the field, which would, in turn, yield physical energy estimates for comparison with observation. An advantage of linking the field and energy to physical values would be the potential for evaluating the energy in the field at different times following a flare, and comparing the change in energy with other observational indicators of energy loss, such as X-ray light curves.

The establishment of a modeling technique that more accurately reflects the observed configuration of the coronal magnetic field without the use of photospheric magnetograms presents an opportunity to study the interface between the photosphere and corona. The distribution of the model field at low heights above the modeled solar surface invites comparison with the real magnetic field distribution observed at the photosphere. Differences between these two distributions may help illuminate the changes that the field and its embedded currents undergo in the transition from the non-force-free photosphere to the force-free low corona. Study of these discrepancies could potentially improve our understanding of the physics of the transition region, and could provide valuable theoretical support for the upcoming *Interface Region Imaging Spectrograph* mission (IRIS, de Pontieu et al., 2009), which

is scheduled to be launched in 2012. IRIS will facilitate detailed study of the flow of plasma and energy from the photosphere to the corona, and theoretical modeling of the transition region will be a crucial tool in interpreting the observations.

The knowledge gained from study of changes in the magnetic field distribution between the photosphere and the corona will also encourage the development of more advanced magnetic models, particularly with the aid of IRIS data. These models will be better disposed than current models to incorporate observational constraints in the form of photospheric magnetograms. A better understanding of the physics of the transition region, including plasma dynamics as well as the evolution of the magnetic field and electrical currents with height, will help modelers formulate a more appropriate treatment of this complex region. These improved models will then be able to incorporate photospheric magnetic field measurements in a more realistic way.

In this thesis, we have used the novel abilities of stereoscopic coronal imaging to identify a critical shortcoming in a practice that is widely used in magnetic modeling: the reliance on photospheric magnetograms as boundary conditions for coronal models. We then presented an original technique, developed as part of the research for this thesis, that avoids this shortcoming and models the coronal magnetic field in a more consistent way. Instead of using the photospheric boundary conditions that have been shown to be problematic for coronal modeling, our submerged dipole method creates a magnetic field model constrained solely by observations of the structure of the coronal field. We have demonstrated that this model achieves better agreement

with observed field structures in four active regions observed by STEREO. Following the establishment of the method's validity, we used the dipole model to investigate the evolution of coronal loops following large solar flares observed by TRACE and SDO, a study that verifies a hypothesis that we posed in the course of analyzing the dipole models of the four active regions observed by STEREO.

The dipole method uses potential (current-free) fields, and is therefore not strictly applicable for modeling a plasma that is believed to carry currents. Nevertheless, the work presented here, and particularly the success of the dipole model relative to other widely used modeling techniques, contains a valuable demonstration of the need for models that treat the interface between the photosphere and corona in a way that more accurately reflects the physics of the region. In this research, then, modelers may find a foundation for future work in advancing the state of magnetic modeling, and for furthering our understanding of the coronal magnetic field.

Appendix A

Frozen Flux Theorem

In magnetohydrodynamics (MHD), the *induction equation* relates the magnetic field to the plasma velocity and is written as follows:

$$\frac{\partial \mathbf{B}}{\partial t} = \nabla \times (\mathbf{v} \times \mathbf{B}) - \nabla \times (\eta \nabla \times \mathbf{B}) \tag{A.1}$$

where η is the magnetic diffusivity, which is inversely proportional to the electrical conductivity, σ: $\eta = 1/(\mu\sigma)$. In a plasma for which η is uniform, equation A.1 becomes:

$$\frac{\partial \mathbf{B}}{\partial t} = \nabla \times (\mathbf{v} \times \mathbf{B}) + \eta \nabla^2 \mathbf{B} \tag{A.2}$$

For a fully ionized plasma such as the corona, the conductivity is given as:

$$\sigma = \frac{n_e e^2 \tau_{ei}}{m_e} \tag{A.3}$$

for n_e the electron density and τ_{ei} the electron-ion collision time. Spitzer (1962) found for τ_{ei} in a fully ionized plasma:

$$\tau_{ei} = 0.266 \times 10^6 \frac{T^{3/2}}{n_e \ln \Lambda} \text{ s} \tag{A.4}$$

The Coulomb logarithm, $\ln \Lambda$, depends on the temperature and density of the plasma, and for the corona is on the order of ~ 10 (Priest, 1982). The conductivity can then be written as:

$$\sigma = 1.53 \times 10^{-2} \frac{T^{3/2}}{\ln \Lambda} \text{ mho m}^{-1} \tag{A.5}$$

and the magnetic diffusivity becomes:

$$\eta = 5.2 \times 10^7 \ln \Lambda \, T^{-3/2} \text{ m}^2 \text{ s}^{-1} \tag{A.6}$$

For values typical of the corona, then, we can apply the perfectly conducting limit ($\sigma \gg 1$ and $\eta \ll 1$) to the induction equation, and equation A.2 reduces to:

$$\frac{\partial \mathbf{B}}{\partial t} = \nabla \times (\mathbf{v} \times \mathbf{B}) \tag{A.7}$$

Now consider a magnetized plasma embedded with magnetic field B and moving with velocity $\mathbf{v}$. We designate a surface S, bounded by a closed curve C and moving with the plasma (Figure A.1). For a time interval δt, a line segment $\delta \mathbf{s}$ moves through

an area $\delta\mathbf{A} = \mathbf{v}\delta t \times \delta\mathbf{s}$. The magnetic flux through $\delta\mathbf{A}$ can be written as follows:

$$dF = \mathbf{B} \cdot (\delta t\mathbf{v} \times \delta\mathbf{s}) \tag{A.8}$$

We can use the triple scalar product to write the flux as:

$$df = -\delta t\mathbf{v} \times B \cdot \delta\mathbf{s} \tag{A.9}$$

We can also find the magnetic flux through the surface S:

$$F = \int\int \mathbf{B} \cdot d\mathbf{S} \tag{A.10}$$

The derivative of this quantity can be expressed as follows:

$$\frac{DF}{Dt} = \int_S \int \frac{\partial \mathbf{B}}{\partial t} \cdot d\mathbf{S} - \oint_C \mathbf{v} \times \mathbf{B} \cdot d\mathbf{s} \tag{A.11}$$

The first term describes the temporal change of the magnetic field; the second incorporates the motion of the boundary C of the surface S and is the integral of equation A.9. We use Stokes' theorem to rewrite the second term as follows:

$$-\int_S \int \nabla \times (\mathbf{v} \times \mathbf{B}) \cdot d\mathbf{S} \tag{A.12}$$

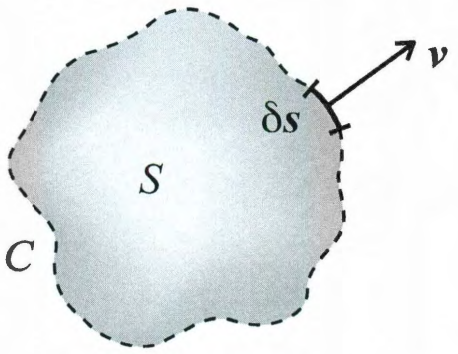

Figure A.1: Representation of a surface, S, in a magnetized plasma. The surface is enclosed by curve C and moves with velocity $\mathbf{v}$.

We can then use this expression to rewrite equation A.11:

$$\frac{DF}{Dt} = \int_S \int \left(\frac{\partial \mathbf{B}}{\partial t} - \nabla \times (\mathbf{v} \times \mathbf{B}) \right) \cdot d\mathbf{S} \tag{A.13}$$

In the case of the corona, a plasma with perfect or nearly perfect conductivity, the integrand of equation A.13 is identically zero according to the induction equation:

$$\frac{\partial \mathbf{B}}{\partial t} = \nabla \times (\mathbf{v} \times \mathbf{B}) \tag{A.14}$$

We therefore conclude that for the surface S moving with the plasma, the magnetic flux through the surface, F, is conserved. Thus, the magnetic field lines are "frozen" in the plasma, and vice versa, the plasma is frozen to the field.

Appendix B

Overview of Magnetic Fields

This appendix contains an overview of three terms commonly used when discussing magnetic fields: *potential*, *linear force-free*, and *non-linear force-free*. These descriptors indicate magnetic fields carrying no current, spatially uniform current that runs parallel to the magnetic field, and spatially distributed parallel current, respectively. The three terms, particularly the last two, are frequently used in the context of magnetic field extrapolation models (see section 2.2.2).

B.1 The Potential Field

In its simplest form, a magnetic field can be expressed as the gradient of a scalar potential, ϕ:

$$\mathbf{B}(\mathbf{r}) = \nabla\phi(\mathbf{r}) \tag{B.1}$$

Because it is derived from a potential function, such a field is known as a *potential field.* Gauss's law for magnetism requires that the field be divergence-free ($\nabla \cdot \mathbf{B} = 0$). The potential field therefore satisfies Laplace's equation:

$$\nabla \cdot \mathbf{B} = \nabla (\nabla \phi) = \nabla^2 \phi = 0 \tag{B.2}$$

Using equation B.1 we can also determine the nature of the electrical currents, if any, that are embedded in a potential field. In cgs units, the current is expressed as follows:

$$\mathbf{j} = \frac{c}{4\pi} (\nabla \times \mathbf{B}) = \frac{c}{4\pi} (\nabla \times \nabla \phi) = 0 \tag{B.3}$$

Thus the current density in a potential field is identically zero, i.e. a potential field is *current-free.*

B.2 Force-Free Fields

Let us consider a magnetic field with nonzero current density $\mathbf{j}$. The current density can be written in terms of the number density, charge, and velocity of the particles that make up the plasma:

$$\mathbf{j} = \frac{q}{c} n \mathbf{v} \tag{B.4}$$

A collection of charged particles moving through a magnetic field $\mathbf{B}$ will feel a force known as the *Lorentz force*:

$$\mathbf{F} = \frac{q}{c} n \left(\mathbf{v} \times \mathbf{B} \right) = \mathbf{j} \times \mathbf{B} \tag{B.5}$$

For a plasma in which movement across the magnetic field is inhibited, the Lorentz force vanishes, and the magnetic field is considered *force-free*:

$$\mathbf{j} \times \mathbf{B} = \frac{c}{4\pi} \left(\nabla \times \mathbf{B} \right) \times \mathbf{B} = 0 \tag{B.6}$$

It is non-trivial to find a solution to this problem, as it is typically non-linear. One can, however, formulate a linear version of the equation. In this case, the currents run parallel to the magnetic field:

$$\left(\nabla \times \mathbf{B} \right) = 4\pi \mathbf{j} = \lambda \left(\mathbf{r} \right) \mathbf{B} \tag{B.7}$$

where $\lambda \left(\mathbf{r} \right)$ is a scalar function that varies with position. Choosing $\lambda \left(\mathbf{r} \right) = 0$ results in the current-free (potential) solution: $\nabla \times \mathbf{B} = 0$. More generally, the choice of $\lambda \left(\mathbf{r} \right)$ must be made such that the field remains divergence-free ($\nabla \cdot \mathbf{B} = 0$). Combining this requirement with equation B.7, the divergence-free condition is now described by two equations:

$$\nabla \cdot \mathbf{B} = 0 \tag{B.8}$$

$$\nabla \cdot (\nabla \times \mathbf{B}) = 0 \tag{B.9}$$

If we combine equations B.7 and B.9, we find the following condition for the function $\lambda(\mathbf{r})$:

$$\nabla \cdot (\nabla \times \mathbf{B}) = \nabla \cdot (\lambda \mathbf{B}) = \lambda (\nabla \cdot \mathbf{B}) + \mathbf{B} \cdot \nabla \lambda = \mathbf{B} \cdot \nabla \lambda = 0 \tag{B.10}$$

Thus, we have the requirement that $\lambda(\mathbf{r})$ be constant along any single magnetic field line. For the case in which λ is constant everywhere, the magnetic field is known as a *linear force-free field* and carries uniform current. For the more general case in which λ varies spatially, $\lambda = \lambda(\mathbf{r})$ (λ remains constant along individual field lines but varies from field line to field line), the magnetic field is known as a *non-linear force-free field* and carries non-uniform current.

Appendix C

High-Pass Filter for Image Processing

Generally speaking, a high-pass filter is a filter that attenuates low-frequency components of a signal and retains the high frequency components. In image processing, it is also known as an *unsharp mask* because it masks the blurred components of the image and enhances the sharper elements. In EUV images of coronal loops such as those used in this work, the loops can appear indistinct and blurry (bottom panel of Figure C.1), which hinders accurate loop tracing. The application of a high-pass filter sharpens the image and enhances features that appear smoothed in the original image (top panel of Figure C.1).

In order to perform a high-pass filtering of an image, one first computes a smoothed version of the image. A boxcar smoothing is used here, in which each pixel is replaced

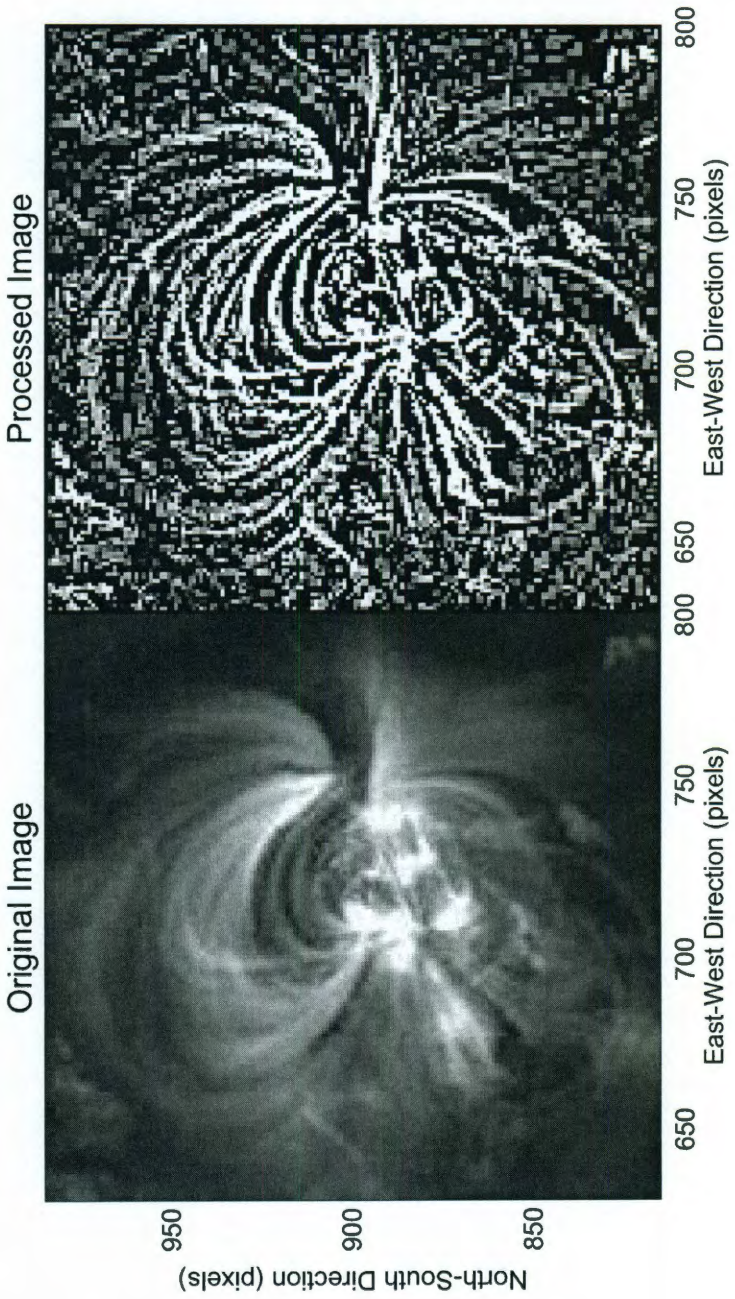

Figure C.1: EUVI images of AR 10955 in the 171 Å channel. Left: unprocessed image. Right: image after the application of a high-pass filter to enhance feature definition for loop tracing.

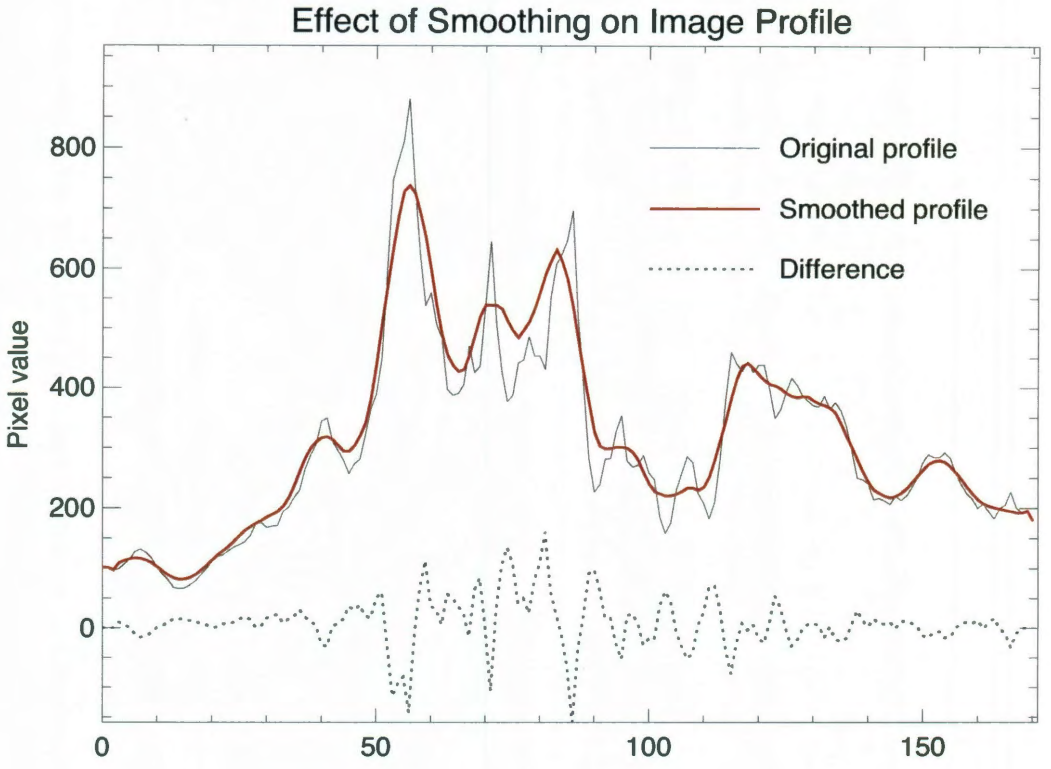

Figure C.2: Profile of a slice through the image in Figure C.1. Solid black line: the original image profile. Solid red line: the "mask," which represents the low-frequency components of the image. Dotted black line: the difference between the two profiles, containing the high-frequency (sharpened) components of the image.

by the average of its neighboring pixels. The size of the neighborhood is chosen by the user; we typically chose a width of 7 pixels. The smoothed image is then subtracted from the original image to complete the high-pass filter (see representative image profiles in Figure C.2). The resulting image contains features that have better definition, facilitating more accurate loop tracing.

Appendix D

Stereoscopic Triangulation of Curvilinear Structures

This appendix presents the mathematical basis of the triangulation used in the stereoscopy of loop structures observed in STEREO/EUVI images, as presented in Aschwanden et al. (2008c). The geometry of the system can be seen in Figure D.1. Let us define a Cartesian coordinate system in (x, y, z) that has its origin, O, at the center of the Sun. The z-axis lies along the line of sight from the origin to the Ahead spacecraft, A, and the x-z plane is defined as the plane of the two spacecraft, A and B, and Sun center. The distances from the spacecraft to Sun center are given as d_A and d_B. The spacecraft are separated by an angle α_{sep}.

The two spacecraft observe a point P, which has coordinates (x, y, z) with respect to Sun center. Point P also has heliographic longitude λ and latitude b, where the

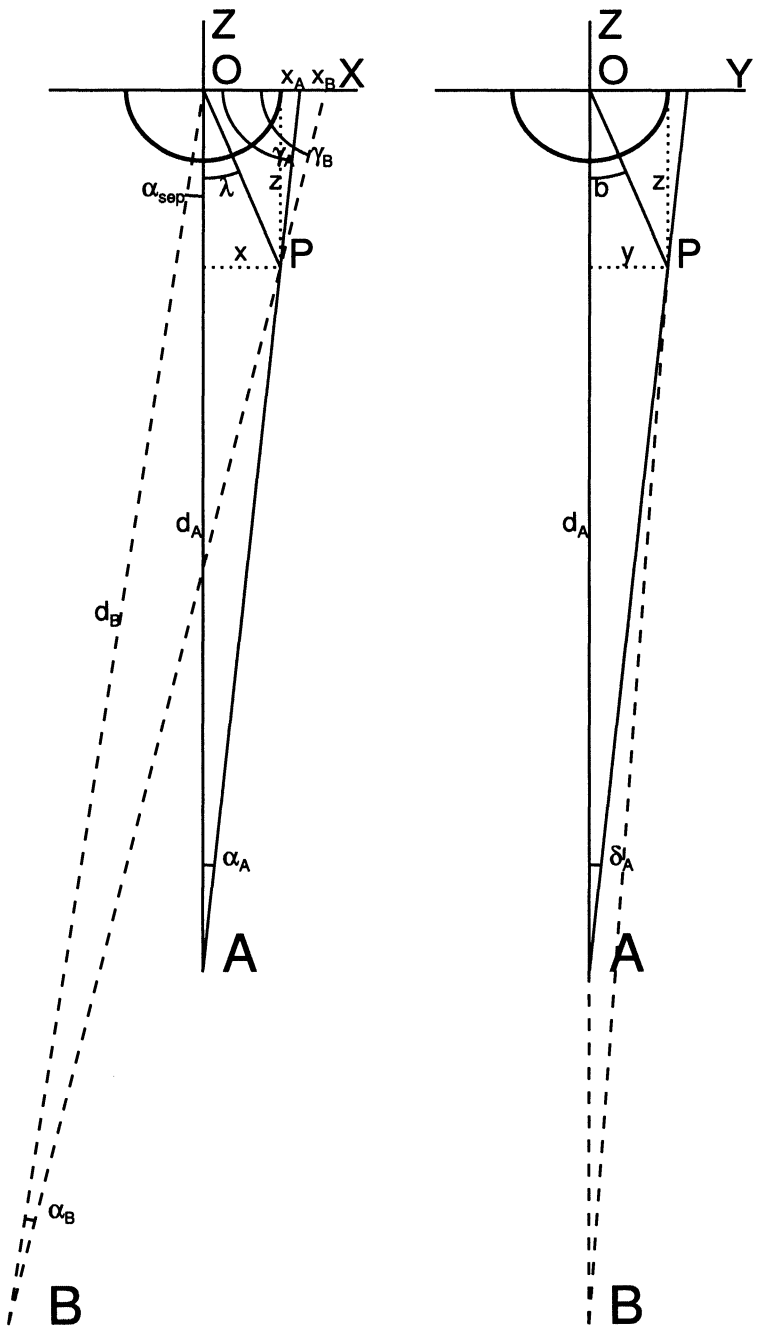

Figure D.1: Geometry of the triangulation of a point, P, using observations from spacecraft A and B. The x-z plane is shown at left, and the y-z plane is shown at right (Aschwanden et al., 2008c).

longitude is defined relative to the central meridian as observed by spacecraft A. The different positions of the spacecraft lead them to observe P from different angles with respect to Sun center: α_A and α_B along the x-axis, and δ_A and δ_B along the y-axis. A and B also observe point P to have coordinates x_A and x_B, respectively, along the x-axis. Using the known and observable quantities $d_A, d_B, \alpha_A, \alpha_B, \delta_A, \delta_B$, and α_{sep}, we can solve for the true position of point P (x, y, z).

We begin by solving for the angles γ_A and γ_B in the triangle given by $O - A - x_A$ and $O - B - x_B$:

$$\gamma_A = \frac{\pi}{2} - \alpha_A \tag{D.1}$$

$$\gamma_B = \frac{\pi}{2} - \alpha_B - \alpha_{sep} \tag{D.2}$$

Using the law of sines for planar triangles, we find expressions for x_A and x_B:

$$x_A = d_A \tan(\alpha_A) \tag{D.3}$$

$$x_B = d_b \frac{\sin \alpha_B}{\sin \gamma_B} \tag{D.4}$$

We also have the following relations using γ_A, γ_B, x_A, and x_B:

$$\tan \gamma_A = \frac{z}{x_A - x} \tag{D.5}$$

$$\tan \gamma_B = \frac{z}{x_B - x} \tag{D.6}$$

Using equations D.5-, we can solve for x and z:

$$x = \frac{x_B \tan\gamma_B - x_A \tan\gamma_A}{\tan\gamma_B - \tan\gamma_A} \tag{D.7}$$

$$z = (x_A - x)\tan\gamma_A \tag{D.8}$$

In the y-z plane (right panel of Figure D.1), the y-coordinate can be determined using the angle δ_A:

$$y = (d_A - z)\tan\delta_A \tag{D.9}$$

Having solved for the coordinates (x, y, z) of the point P, the distance between Sun center (O) and P is simply $r = \sqrt{x^2 + y^2 + z^2}$. We can then solve for the height h above the solar surface:

$$h = r - R_\odot \tag{D.10}$$

where $R_\odot$ is the solar radius. We can also calculate the heliographic longitude and latitude of point P:

$$\lambda = \arctan\left(\frac{x}{y}\right) \tag{D.11}$$

$$b = \arctan\left(\frac{y}{z}\right) \tag{D.12}$$

Thus we have not only the Cartesian coordinates of point P, (x, y, z), but also its spherical coordinates, (r, λ, b).

We can also calculate the coordinates of point P as observed by the two spacecraft:

in the plane of the image, (α_A, δ_A) and (α_B, δ_B). These coordinates become useful when we wish to project onto the B image, for example, the anticipated paths that a loop already traced in A might take for a range of heights h (see Figures D.3(b)-D.3(c)). We use the following relations, which are straightforwardly deduced from Figure D.1:

$$\tan\lambda = \frac{x}{z} \tag{D.13}$$

$$\tan b = \frac{y}{z} \tag{D.14}$$

$$\tan\alpha_A = \frac{x}{(d_A - z)} \tag{D.15}$$

$$\tan\delta_A = \frac{y}{(d_A - z)} \tag{D.16}$$

$$r^2 = x^2 + y^2 + z^2 \tag{D.17}$$

We can solve the last equation for z to find two solutions:

$$z = \frac{d_a t^2 \pm \sqrt{r^2\left(1+t^2\right) - d_A^2 t^2}}{\left(1+t^2\right)} \tag{D.18}$$

where we have made the substitution

$$t^2 = (\tan\alpha_A)^2 + (\tan\delta_A)^2 \tag{D.19}$$

The remaining variables can now be found:

$$x = (d_A - z)\tan\alpha_A \tag{D.20}$$

$$y = (d_A - z)\tan\delta_A \tag{D.21}$$

$$x_{B0} = d_b \sin\alpha_{sep} \tag{D.22}$$

$$z_B = \sqrt{d_B^2 - x_{B0}^2} \tag{D.23}$$

$$\gamma_B = \arctan\left(\frac{z_B - z}{x_{B0} - x}\right) \tag{D.24}$$

$$\alpha_B = \frac{\pi}{2} - \gamma_B - \alpha_{sep} \tag{D.25}$$

$$\delta_B = \arctan\left(\frac{y}{d_B - z}\right) \tag{D.26}$$

With these variables we can predict the coordinates (α_B, δ_B) of point P projected in the B image. The utility of these predictions can be seen in Figures D.3(b) and D.3(c), which show loop tracing in the EUVI-B image, and D.5, which shows all traced loops for AR 10955, as well as height projections, for the B image.

Figures D.2 - D.3 show the process of tracing a single loop, starting with the definition of a region of interest in the A image in Figure D.2. The three panels of Figure D.3 show the steps in the tracing: the user first selects several points on the loop in the A image, and the code interpolates a smooth curve via a spline fit (Figure D.3(a)). The user then traces conjugate points in the B image, which are guided by projections of the curve traced in A (Figures D.3(b) and D.3(c)). This process is repeated for all identifiable loop structures in both images. The collection

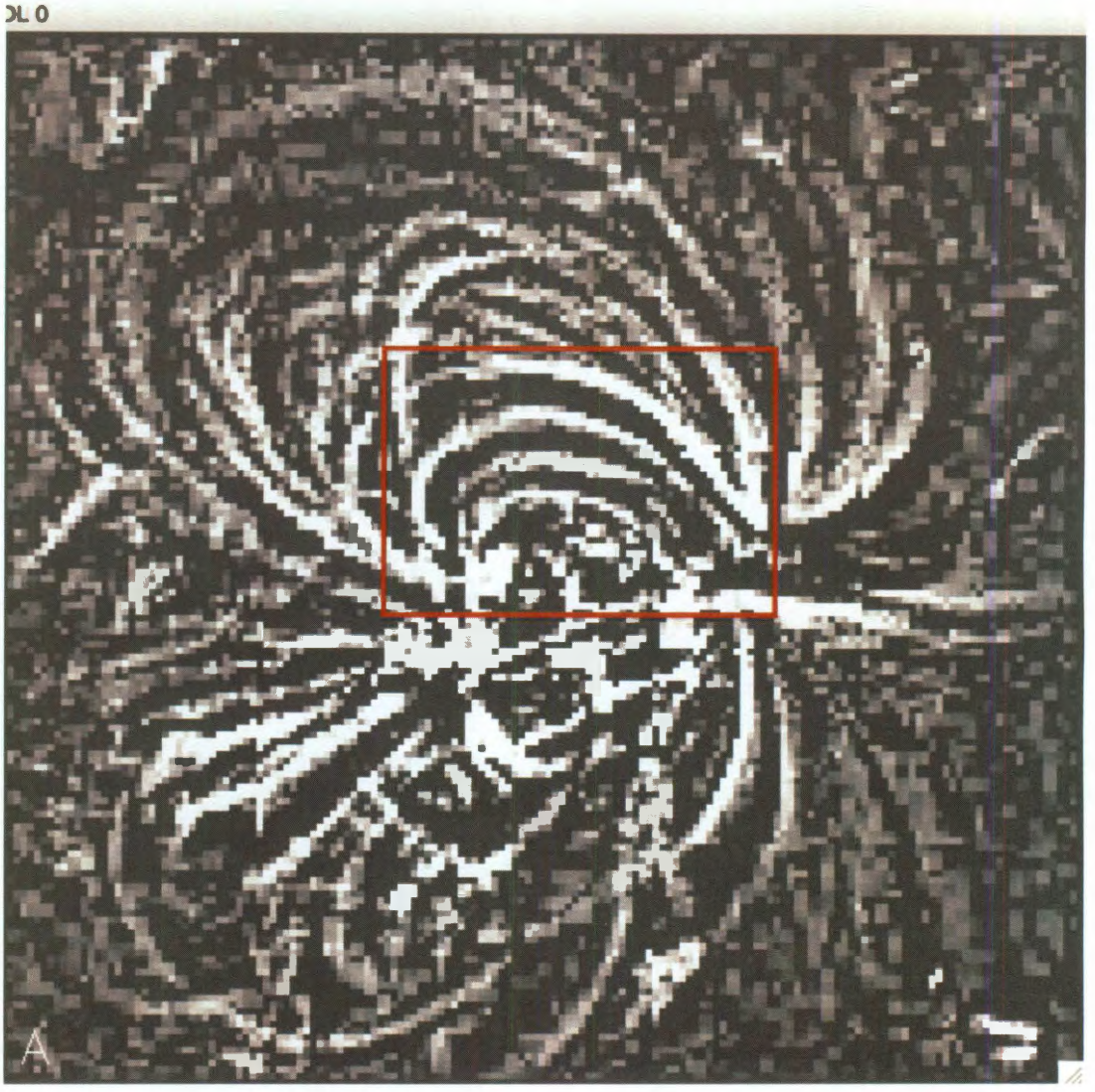

Figure D.2: Preparing for loop tracing in a high-pass-filtered image of AR 10955 in the 171 Å channel. The user must first select the area in which a loop is to be traced (red box)

of loops for AR 10955 can be seen displayed over a logarithmic contour representation of the EUVI-A image in Figure D.4). The loops can also be seen in Figure D.5 over a logarithmic contour representation of the EUVI-B image. In this figure, the thick red lines represent the triangulated loops, and the thin red lines represent projections of curves traced in EUVI-A at two heights: $h = 0$ (solid lines) and $h = 0.1R_{\odot}$ (dashed lines). Finally, the 3D structure of all loops can be seen in three different perspectives in Figure D.6.

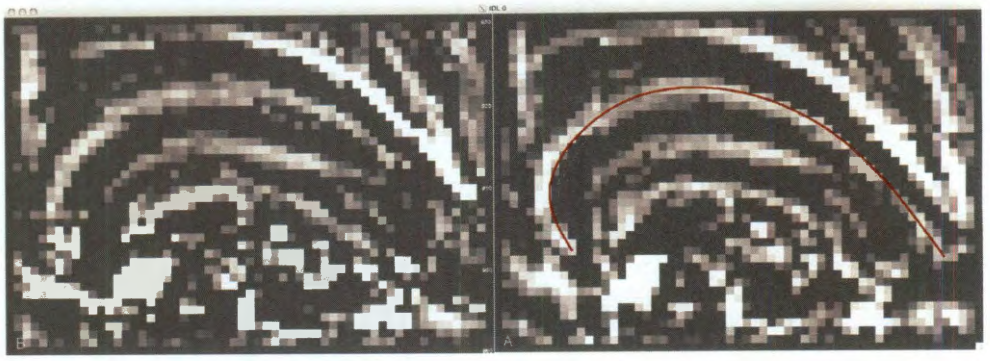

(a) Loop tracing in the EUVI-A image (right). The user clicks on 3-5 points along a loop. The code performs a spline fit to the points, and displays the resulting curve. The B image is shown at left.

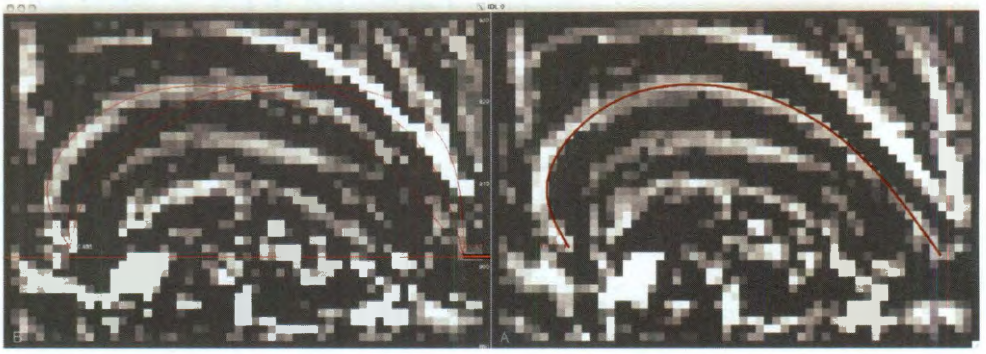

(b) Loop tracing in the EUVI-B image (left). The code plots indicators (thin red lines) of the loop path for different heights. The user must first click on the loop at the initial point (thick red bar). The A image is shown at right, with the curve traced in that image.

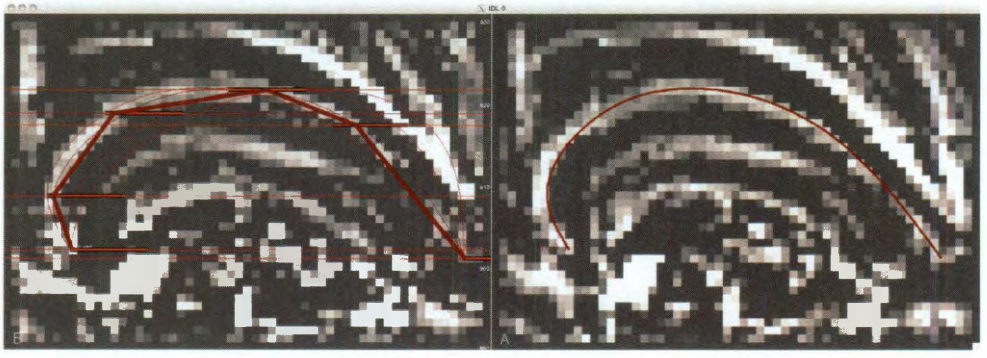

(c) Loop tracing in the EUVI-B image (left), continued. The code provides guides (thick red bars) indicating the range of positions that correspond, at a given point clicked in the A image, to different heights. The user clicks on the points at which the guides intersect the observed loop, and the coordinates are stored. The A image is shown at right.

Figure D.3: Screenshots of the loop tracing process.

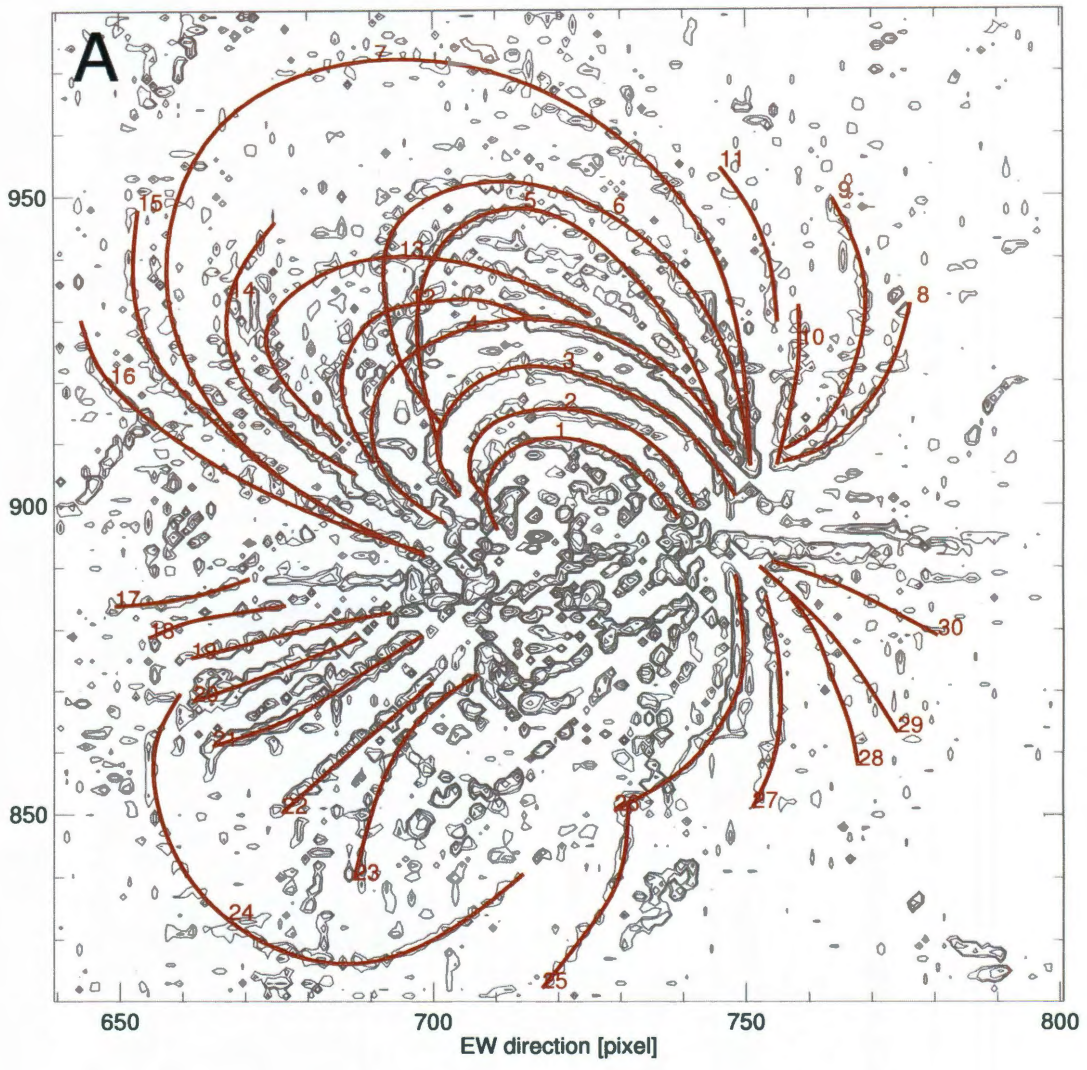

Figure D.4: Loops traced in the EUVI-A image for AR 10955 (9 May 2007). Background is a logarithmic contour plot of the EUVI-A image, subjected to a high-pass filter as discussed in Appendix C (Aschwanden et al., 2008c).

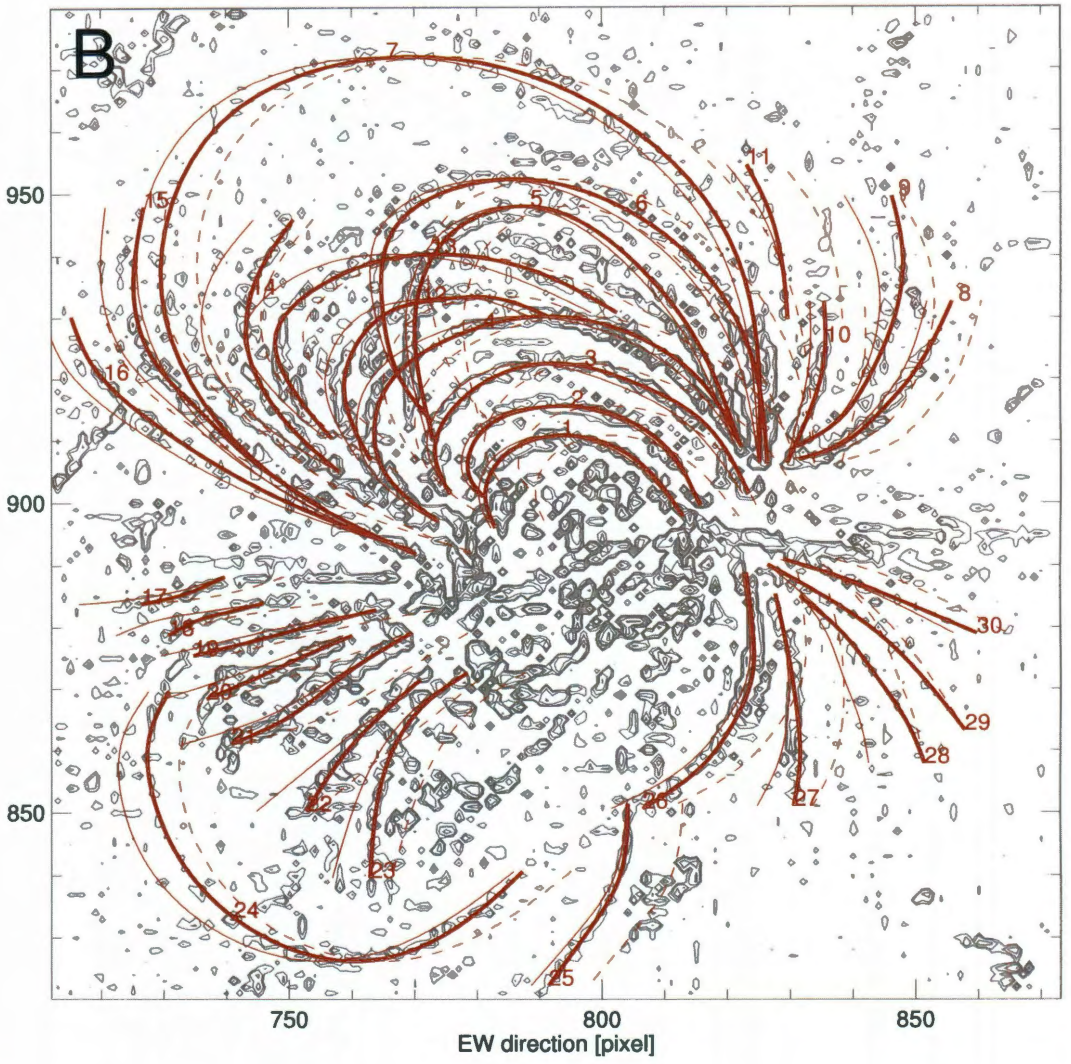

Figure D.5: Representation is similar to Figure D.4, but for the EUVI-B image. Thick red lines represent the traced loops. Thin solid red lines indicate loop projections, based on curves traced in the A image, calculated for photospheric heights ($h = 0$). Thin dashed red lines indicated loop projections for constant height $h = 0.1R_{\odot}$ (Aschwanden et al., 2008c).

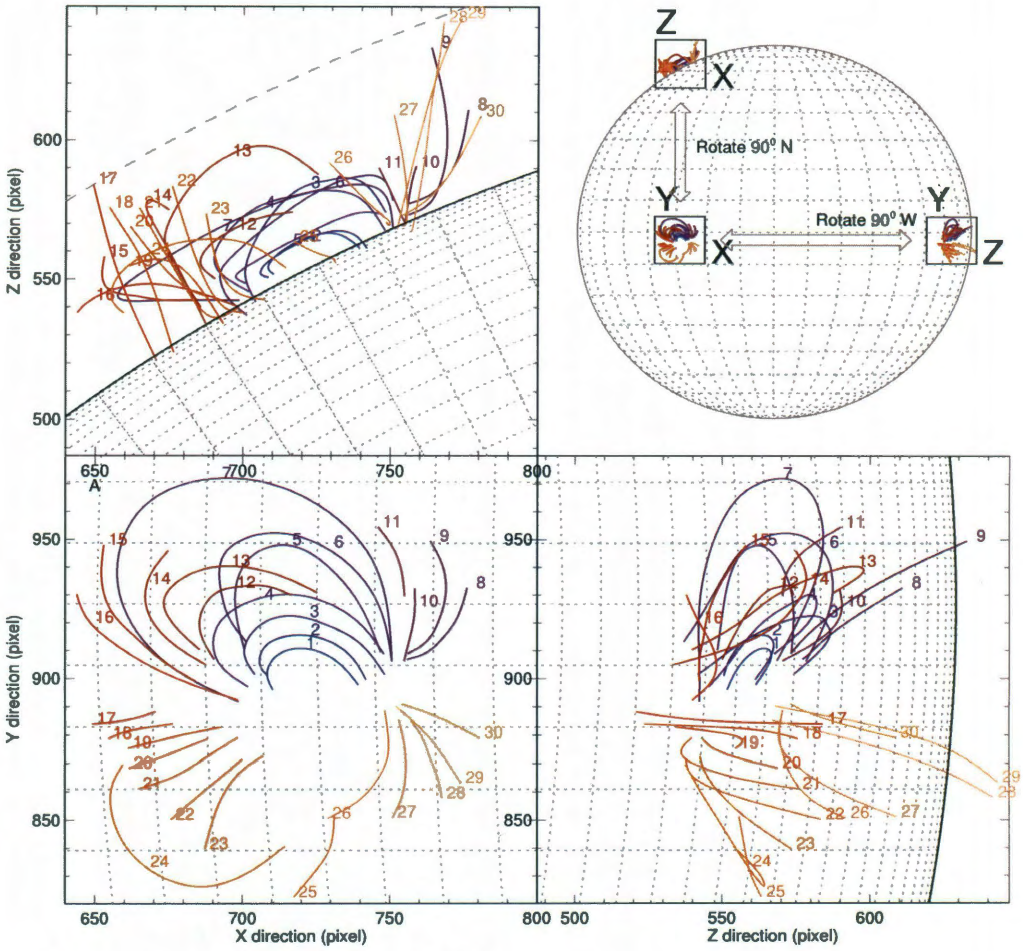

Figure D.6: Triangulated loops for AR 10955 (9 May 2007) shown from three different perspectives, which are illustrated in the diagram at top right Bottom left: the loops as seen from the EUVI-A spacecraft. Top left: the loops as seen rotated up 90°. Bottom right: the loops as seen rotated 90° to the west (Aschwanden et al., 2008c).

Appendix E

Dipole Magnetic Fields: the Far-Field Approximation

The dipole modeling method initially presented in Chapter 4 makes use of the *far field approximation* for the field due to a magnetic dipole. The approximation applies in situations where the size of the magnetic dipole, or the size of the current distribution that gives rise to the magnetic field, is small compared with the distance at which the field is evaluated. This appendix presents a derivation of the approximation.

We start with the law of Biot and Savart, which describes the magnetic field $\mathbf{B}$ at a given point P due to a length of wire $d\mathbf{l}$ carrying electrical current I:

$$d\mathbf{B} = kI\frac{(d\mathbf{l} \times \mathbf{x})}{|x|^3}, \tag{E.1}$$

where $\mathbf{x}$ is the vector from the element of wire to the point at which the field is

evaluated. If we generalize the equation from the field due to an infinitesimal length of wire to a finite distribution of current density $\mathbf{J}(\mathbf{x})$ (see Figure E.1), we obtain the following:

$$\mathbf{B}(\mathbf{x}) = \frac{\mu_0}{4\pi} \int \mathbf{J}(\mathbf{x}') \times \frac{\mathbf{x} - \mathbf{x}'}{|\mathbf{x} - \mathbf{x}'|^3} d^3x', \tag{E.2}$$

where $\mathbf{x}'$ is the coordinate of an element within the current distribution, and $\mathbf{x}$ remains the vector to the point at which the field is evaluated. We can obtain a more useful form of equation E.2 using the following relation:

$$\frac{\mathbf{x} - \mathbf{x}'}{|\mathbf{x} - \mathbf{x}'|^3} = -\nabla \left(\frac{1}{|\mathbf{x} - \mathbf{x}'|} \right), \tag{E.3}$$

which yields as an alternative to equation E.2:

$$\mathbf{B}(\mathbf{x}) = \frac{\mu_0}{4\pi} \nabla \times \int \frac{\mathbf{J}(\mathbf{x}')}{|\mathbf{x} - \mathbf{x}'|} d^3x' \tag{E.4}$$

We can then express the field as the curl of a *vector potential* function, $\mathbf{A}(\mathbf{x})$:

$$\mathbf{A}(\mathbf{x}) = \frac{\mu_0}{4\pi} \int \frac{\mathbf{J}(\mathbf{x}')}{|\mathbf{x} - \mathbf{x}'|} d^3x'. \tag{E.5}$$

Because we consider only the far-field case here, we assume that $|\mathbf{x}| \gg |\mathbf{x}'|$, which allows us to expand the denominator of equation E.5 in powers of $\mathbf{x}'$:

$$\frac{1}{|\mathbf{x} - \mathbf{x}'|} = \frac{1}{|\mathbf{x}|} + \frac{\mathbf{x} \cdot \mathbf{x}'}{|\mathbf{x}|^3} + \cdots \tag{E.6}$$

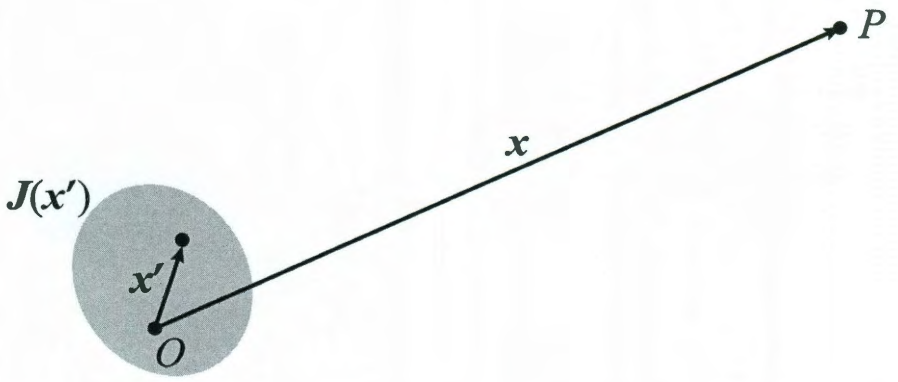

Figure E.1: The localized current distribution $\mathbf{J}(\mathbf{x}')$ (shaded area), which gives rise to a magnetic field that is calculated at point P.

Substituting this expansion into equation E.5, we have the following for each component of the vector potential:

$$A_i(\mathbf{x}) = \frac{\mu_0}{4\pi}\left[\frac{1}{|\mathbf{x}|}\int j_i(\mathbf{x}')\,d^3x' + \frac{\mathbf{x}}{|\mathbf{x}|^3}\cdot\int J_i(\mathbf{x}')\,\mathbf{x}'d^3x' + \cdots\right] \tag{E.7}$$

We now wish to simplify the above expression. We define two well-behaved functions of $\mathbf{x}'$, $f(\mathbf{x}')$ and $g(\mathbf{x}')$. Because the current density $\mathbf{J}(\mathbf{x}')$ is localized, we have the following identity:

$$\int (f\mathbf{J}\cdot\nabla' g + g\mathbf{J}\cdot\nabla' f + fg\nabla'\cdot\mathbf{J})\,d^3x' = 0, \tag{E.8}$$

which is based on an integration by parts of the second term. If we require that $\nabla'\cdot\mathbf{J} = 0$ and declare that $f = 1$ and $g = x'$, we find:

$$\int J_i(\mathbf{x}')\,d^3x' = 0 \tag{E.9}$$

Thus, the first term in equation E.7 vanishes. For $f = x'_i$ and $g = x'_j$, we have the following condition from equation E.8:

$$\int \left(x'_i J_j + x'_j J_i\right) d^3x' = 0, \tag{E.10}$$

which allows us to write the second term of equation E.7 as follows:

$$\begin{aligned}
\mathbf{x} \cdot \int \mathbf{x}' J_i d^3x' &\equiv \sum_j x_j \int x_j J_i d^3x' && \text{(E.11)} \\
&= -\frac{1}{2} \sum_j x_j \int \left(x'_i J_j - x'_j J_i\right) d^3x' && \text{(E.12)} \\
&= -\frac{1}{2} \sum_{j,k} \epsilon_{ijk} x_j \int (\mathbf{x}' \times \mathbf{j})_k \, d^3x' && \text{(E.13)} \\
&= -\frac{1}{2} \left[\mathbf{x} \times \int (\mathbf{x}' \times \mathbf{J}) \, d^3x'\right]_i && \text{(E.14)}
\end{aligned}$$

The magnetic moment is customarily defined as the integral of the magnetic moment density:

$$\mathbf{m} = \frac{1}{2} \int \mathbf{x}' \times \mathbf{J}(\mathbf{x}') \, d^3x' \tag{E.15}$$

Using this expression with equation E.7, we have the vector potential as a function of the magnetic moment:

$$\mathbf{A}(\mathbf{x}) = \frac{\mu_0}{4\pi} \frac{\mathbf{m} \times \mathbf{x}}{|\mathbf{x}|^3} \tag{E.16}$$

This equation represents the lowest order physical (non-vanishing) term in equation E.7 for a current distribution that is both localized and steady-state. Evaluating the

curl of equation E.16 yields:

$$\mathbf{B}(\mathbf{x}) = \frac{\mu_0}{4\pi}\left[\frac{3\mathbf{n}(\mathbf{n}\cdot\mathbf{m}) - \mathbf{m}}{|\mathbf{x}|^3}\right] \tag{E.17}$$

which is the magnetic field due to a localized current distribution.

Bibliography

Abbett, W. P. 2007, *Astrophysical Journal*, 665, 1469

Abbett, W. P., & Fisher, G. H. 2003, *Astrophysical Journal*, 582, 475

Alexander, D. 2009, The Sun (Santa Barbara, California: Greenwood Guides to the Universe)

Altschuler, M. D., & Newkirk, G. 1969, Solar Physics, 9, 131

Arnaud, J., & Newkirk, Jr., G. 1987, *Astronomy & Astrophysics*, 178, 263

Aschwanden, M. J. 2004, Physics of the Solar Corona: An Introduction (Berlin: Springer)

—. 2010, *Solar Physics*, 262, 399

Aschwanden, M. J., & Alexander, D. 2001, *Solar Physics*, 204, 91

Aschwanden, M. J., Alexander, D., Hurlburt, N., Newmark, J. S., Neupert, W. M., Klimchuk, J. A., & Gary, G. A. 2000, *Astrophysical Journal*, 531, 1129

Aschwanden, M. J., Lee, J. K., Gary, G. A., Smith, M., & Inhester, B. 2008a, *Solar Physics*, 248, 359

Aschwanden, M. J., Newmark, J. S., Delaboudinière, J., Neupert, W. M., Klimchuk, J. A., Gary, G. A., Portier-Fozzani, F., & Zucker, A. 1999, *Astrophysical Journal*, 515, 842

Aschwanden, M. J., Nitta, N. V., Wülser, J., & Lemen, J. R. 2008b, *Astrophysical Journal*, 680, 1477

Aschwanden, M. J., & Sandman, A. W. 2010, *Astronomical Journal*, in press

Aschwanden, M. J., & Wülser, J. 2010, *Journal of Atmospheric and Solar-Terrestrial Physics*, subm.

Aschwanden, M. J., Wülser, J., Nitta, N. V., & Lemen, J. R. 2008c, *Astrophysical Journal*, 679, 827

Aschwanden, M. J., Wülser, J., Nitta, N. V., Lemen, J. R., & Sandman, A. 2009, *Astrophysical Journal*, 695, 12

Aschwanden, M. J., et al. 2008d, Space Science Reviews, 136, 565

Aulanier, G., DeLuca, E. E., Antiochos, S. K., McMullen, R. A., & Golub, L. 2000, *Astrophysical Journal*, 540, 1126

Aulanier, G., Schmieder, B., Démoulin, P., van Driel-Gesztelyi, L., & DeForest, C. 1998, in ASP Conference Series, Vol. 155, 2nd Advances in Solar Physics Eurocon-

ference: Three-Dimensional Structure of Solar Active Regions, ed. C. E. Alissandrakis & B. Schmieder, 105–109

Babcock, H. W. 1953, *Astrophysical Journal*, 118, 387

Baum, W. A., Johnson, F. S., Oberly, J. J., Rockwood, C. C., & Strain, C. V. 1946, Physical Review, 70, 781

Bellot Rubio, L. R., Ruiz Cobo, B., & Collados, M. 2000, *Astrophysical Journal*, 535, 475

Berger, M., & Colella, P. 1989, Journal of Computational Physics, 82, 64

Berger, M., & Oliger, J. 1984, Journal of Computational Physics, 53, 484

Berger, T. E., de Pontieu, B., Fletcher, L., Schrijver, C. J., Tarbell, T. D., & Title, A. M. 1999, *Solar Physics*, 190, 409

Berton, R., & Sakurai, T. 1985, *Solar Physics*, 96, 93

Bobra, M. G., van Ballegooijen, A. A., & DeLuca, E. E. 2008, *Astrophysical Journal*, 672, 1209

Bogod, V. M., & Gelfreikh, G. B. 1980, *Solar Physics*, 67, 29

Bommier, V., & Sahal-Bréchot, S. 1982, *Solar Physics*, 78, 157

Bone, L. A., van Driel-Gesztelyi, L., Culhane, J. L., Aulanier, G., & Liewer, P. 2009, *Solar Physics*, 259, 31

Brosius, J. W., & White, S. M. 2006, *Astrophysical Journal Letters*, 641, L69

Casini, R., & Judge, P. G. 1999, *Astrophysical Journal*, 522, 524

Conlon, P. A., & Gallagher, P. T. 2010, *Astrophysical Journal*, 715, 59

de Pontieu, B., Title, A. M., Schryver, C. J., Lemen, J. R., Golub, L., Kankelborg, C. C., & Carlsson, M. 2009, AGU Fall Meeting Abstracts, B1499+

de Toma, G., Gibson, S., Emery, B., & Kozyra, J. 2010, Twelfth International Solar Wind Conference, 1216, 667

Delaboudinière, J.-P., et al. 1995, *Solar Physics*, 162, 291

Démoulin, P., Henoux, J. C., Mandrini, C. H., & Priest, E. R. 1997, *Solar Physics*, 174, 73

DeRosa, M. L., et al. 2009, *Astrophysical Journal*, 696, 1780

Derouich, M., Auchère, F., Vial, J. C., & Zhang, M. 2010, *Astronomy & Astrophysics*, 511, A7+

Domingo, V., Fleck, B., & Poland, A. I. 1995, *Solar Physics*, 162, 1

Fan, Y. 2004, Living Reviews in Solar Physics, 1, 1

—. 2009, *Astrophysical Journal*, 697, 1529

Fan, Y., Abbett, W. P., & Fisher, G. H. 2003, *Astrophysical Journal*, 582, 1206

Fang, F., Manchester, W., Abbett, W. P., & van der Holst, B. 2010, *Astrophysical Journal*, 714, 1649

Faurobert-Scholl, M. 1994, *Astronomy & Astrophysics*, 285, 655

Feng, L., Inhester, B., Solanki, S. K., Wiegelmann, T., Podlipnik, B., Howard, R. A., & Wuelser, J. 2007, *Astrophysical Journal Letters*, 671, L205

Fletcher, L., & De Pontieu, B. 1999, *Astrophysical Journal Letters*, 520, L135

Fletcher, L., Metcalf, T. R., Alexander, D., Brown, D. S., & Ryder, L. A. 2001, *Astrophysical Journal*, 554, 451

Gary, D. E., & Hurford, G. J. 1994, *Astrophysical Journal*, 420, 903

Gary, G. A. 2001a, AGU Spring Meeting Abstracts, 51

—. 2001b, *Solar Physics*, 203, 71

Gary, G. A. 2003, in Bulletin of the American Astronomical Society, Vol. 35, Bulletin of the American Astronomical Society, 834–+

Gary, G. A., & Alexander, D. 1999, *Solar Physics*, 186, 123

Hale, G. E., Ellerman, F., Nicholson, S. B., & Joy, A. H. 1919, *Astrophysical Journal*, 49, 153

Handy, B. N., et al. 1999, *Solar Physics*, 187, 229

Howard, R., Tanenbaum, A. S., & Wilcox, J. M. 1968, *Solar Physics*, 4, 286

Howard, R. A., et al. 2008, Space Science Reviews, 136, 67

Inhester, B. 2006, ArXiv Astrophysics e-prints

Jackson, J. D. 1999, Classical Electrodynamics, 3rd edn. (New York, NY: Wiley)

Jing, J., Yurchyshyn, V. B., Yang, G., Xu, Y., & Wang, H. 2004, *Astrophysical Journal*, 614, 1054

Judge, P. G. 1998, *Astrophysical Journal*, 500, 1009

Judge, P. G., Low, B. C., & Casini, R. 2006, *Astrophysical Journal*, 651, 1229

Kazachenko, M. D., Canfield, R. C., Longcope, D. W., Qiu, J., Des Jardins, A., & Nightingale, R. W. 2009, *Astrophysical Journal*, 704, 1146

Kittinaradorn, R., Ruffolo, D., & Matthaeus, W. H. 2009, *Astrophysical Journal Letters*, 702, L138

Kosovichev, A. G., & HMI Science Team. 2007, Astronomische Nachrichten, 328, 339

Kosugi, T., et al. 2007, *Solar Physics*, 243, 3

Koutchmy, S., & Molodenskii, M. M. 1992, *Nature*, 360, 717

Li, Y., & Luhmann, J. 2006, *Astrophysical Journal*, 648, 732

Li, Y., Lynch, B. J., Stenborg, G., Luhmann, J. G., Huttunen, K. E. J., Welsch, B. T., Liewer, P. C., & Vourlidas, A. 2008, *Astrophysical Journal Letters*, 681, L37

Liewer, P. C., de Jong, E. M., Hall, J. R., Howard, R. A., Thompson, W. T., Culhane, J. L., Bone, L., & van Driel-Gesztelyi, L. 2009, *Solar Physics*, 256, 57

Lin, C., Gallagher, P. T., & Raftery, C. L. 2010, *Astronomy & Astrophysics*, 516, A44+

Lin, H., Kuhn, J. R., & Coulter, R. 2004, *Astrophysical Journal Letters*, 613, L177

Lin, H., Penn, M. J., & Tomczyk, S. 2000, *Astrophysical Journal Letters*, 541, L83

Lin, J., Soon, W., & Baliunas, S. L. 2003, *New Astronomy Reviews*, 47, 53

Liu, Y., & Lin, H. 2008, *Astrophysical Journal*, 680, 1496

Longcope, D. W. 2005, Living Reviews in Solar Physics, 2

López Ariste, A., et al. 2005, *Astrophysical Journal Letters*, 621, L145

Lyot, B. 1932, *Zeitschrift für Astrophysik*, 5, 73

Metcalf, T. R., Jiao, L., McClymont, A. N., Canfield, R. C., & Uitenbroek, H. 1995, *Astrophysical Journal*, 439, 474

Mickey, D. L. 1973, *Astrophysical Journal Letters*, 181, L19+

Mickey, D. L., Canfield, R. C., Labonte, B. J., Leka, K. D., Waterson, M. F., & Weber, H. M. 1996, *Solar Physics*, 168, 229

Miesch, M. S. 2005, Living Reviews in Solar Physics, 2

Mittal, N., & Narain, U. 2010, Journal of Atmospheric and Solar-Terrestrial Physics, 72, 643

Morgan, H., & Habbal, S. R. 2010, *Astrophysical Journal*, 710, 1

Penn, M. J., Arnaud, J., Mickey, D. L., & Labonte, B. J. 1994, *Astrophysical Journal*, 436, 368

Phillips, K. J. H., Chifor, C., & Landi, E. 2005, *Astrophysical Journal*, 626, 1110

Plewa, T., Linde, T., & Gregory, V. 2005, Adaptive Mesh Refinement - Theory and Applications: Proceedings of the Chicago Workshop on Adaptive Mesh Refinement Methods, Sept. 3-5, 2003 (Berlin: Springer)

Press, W. H., Flannery, B. P., Teukolsky, S. A., & Vettering, W. T. 1986, Numerical Recipes in C++: The Art of Scientific Computing (Cambridge University Press)

Priest, E. R. 1982, Solar Magneto-hydrodynamics (Dordrecht, Holland: D. Reidel)

Pulkkinen, T. 2007, Living Reviews in Solar Physics, 4

Querfeld, C. W., & Smartt, R. N. 1984, *Solar Physics*, 91, 299

Régnier, S., Amari, T., & Kersalé, E. 2002, *Astronomy & Astrophysics*, 392, 1119

Rhodes, Jr., E. J., Cacciani, A., Garneau, G., Misch, T., Progovac, D., Shieber, T., Tomczyk, S., & Ulrich, R. K. 1988, in Flare Research at the Next Solar Maximum, ed. R. C. Canfield & B. R. Dennis, 33–49

Ryabov, B. I., Pilyeva, N. A., Alissandrakis, C. E., Shibasaki, K., Bogod, V. M., Garaimov, V. I., & Gelfreikh, G. B. 1999, *Solar Physics*, 185, 157

Sahal-Bréchot, S., Malinovsky, M., & Bommier, V. 1986, *Astronomy & Astrophysics*, 168, 284

Sakurai, T. 1982, *Solar Physics*, 76, 301

Sakurai, T., Shibata, K., Ichimoto, K., Tsuneta, S., & Acton, L. W. 1992, *Publications of the Astronomical Society of Japan*, 44, L123

Schatten, K. H., Wilcox, J. M., & Ness, N. F. 1969, *Solar Physics*, 6, 442

Scherrer, P. H., et al. 1995, *Solar Physics*, 162, 129

Schmieder, B., Démoulin, P., Aulanier, G., & Golub, L. 1996, *Astrophysical Journal*, 467, 881

Schrijver, C. J. 2001, in Astronomical Society of the Pacific Conference Series, Vol. 223, 11th Cambridge Workshop on Cool Stars, Stellar Systems and the Sun, ed. R. J. Garcia Lopez, R. Rebolo, & M. R. Zapaterio Osorio, 131

Schrijver, C. J., & De Rosa, M. L. 2003, *Solar Physics*, 212, 165

Schrijver, C. J., DeRosa, M. L., & Title, A. M. 2010, *Astrophysical Journal*, 719, 1083

Schrijver, C. J., DeRosa, M. L., Title, A. M., & Metcalf, T. R. 2005, *Astrophysical Journal*, 628, 501

Schrijver, C. J., & van Ballegooijen, A. A. 2005, *Astrophysical Journal*, 630, 552

Seehafer, N. 1982, *Solar Physics*, 81, 69

Somov, B. V., Kosugi, T., Hudson, H. S., Sakao, T., & Masuda, S. 2002, *Astrophysical Journal*, 579, 863

Soufli, R., et al. 2005, in Presented at the Society of Photo-Optical Instrumentation Engineers (SPIE) Conference, Vol. 5901, Society of Photo-Optical Instrumentation Engineers (SPIE) Conference Series, ed. S. Fineschi & R. A. Viereck, 173–183

Spiegel, E. A., & Zahn, J. 1992, *Astronomy & Astrophysics*, 265, 106

Spitzer, L. 1962, Physics of Fully Ionized Gases (Wiley)

Sterling, A. C., & Moore, R. L. 2004, *Astrophysical Journal*, 602, 1024

Strain, C. V. 1947, Sky & Telescope, 6, 3

Sturrock, P. A. 1994, Plasma Physics (Cambridge University Press)

Tomczyk, S., et al. 2008, *Solar Physics*, 247, 411

Vaiana, G. S., Zombeck, M., Krieger, A. S., & Timothy, A. F. 1976, Astrophysics and Space Science, 39, 75

Wang, Y., & Sheeley, Jr., N. R. 2003, *Astrophysical Journal*, 599, 1404

Westendorp Plaza, C., del Toro Iniesta, J. C., Ruiz Cobo, B., Martinez Pillet, V., Lites, B. W., & Skumanich, A. 1998, *Astrophysical Journal*, 494, 453

White, S. M., & Kundu, M. R. 1997, *Solar Physics*, 174, 31

Winebarger, A. R., Warren, H. P., & Seaton, D. B. 2003, *Astrophysical Journal*, 593, 1164

Wülser, J., et al. 2004, in Presented at the Society of Photo-Optical Instrumentation Engineers (SPIE) Conference, Vol. 5171, Society of Photo-Optical Instrumentation Engineers (SPIE) Conference Series, ed. S. Fineschi & M. A. Gummin, 111–122

Yan, X., Qu, Z., Xu, C., Xue, Z., & Kong, D. 2009, Research in Astronomy and Astrophysics, 9, 596

Yan, Y., & Huang, G. 2003, *Space Science Reviews*, 107, 111

Zhou, G., Wang, Y., & Wang, J. 2006, Advances in Space Research, 38, 466